Magnetism in Two-Dimensional van der Waals Materials

by

Dahlia Klein

B.A., M.S., University of Pennsylvania (2015)

Submitted to the Department of Physics
in partial fulfillment of the requirements for the degree of

Doctor of Philosophy

at the

MASSACHUSETTS INSTITUTE OF TECHNOLOGY

June 2021

Author . . . .
Department of Physics
May 3, 2021

Certified by . . . .
Pablo Jarillo-Herrero
Professor of Physics
Thesis Supervisor

Accepted by . . . .
Deepto Chakrabarty
Associate Department Head

Magnetism in Two-Dimensional van der Waals Materials

by

Dahlia Klein

Submitted to the Department of Physics
on May 3, 2021, in partial fulfillment of the
requirements for the degree of
Doctor of Philosophy

Abstract

Layered van der Waals crystals are a rich proving ground for exploring electronic behavior confined to two dimensions. Since the discovery of graphene in 2004, a large family of crystals has been isolated in the ultrathin limit, hosting a range of different properties, including semiconductors, superconductors, and topological insulators. These few-atom-thick sheets can be restacked into endless combinations of artificial heterostructures with atomically sharp interfaces that can be thought of as fundamentally new quantum materials. For over a decade, however, magnetism was noticeably absent from van der Waals materials.

In this thesis, I present experiments on one of the first families of 2D magnets, the insulating chromium trihalides (CrX_3), including CrI_3 and $CrCl_3$. These results were enabled by techniques developed to manipulate these air-sensitive few-layer crystals in an inert glovebox environment. I discuss magneto-optical experiments to measure and electrically control the magnetic ordering of ultrathin CrI_3. I also present a new approach to probe the layer-dependent magnetic ordering by electron tunneling through van der Waals spin-filter magnetic tunnel junctions, where a few-layer crystal of CrX_3 serves as the insulating tunnel barrier. Surprisingly, these magneto-optical and tunneling experiments reveal magnetic properties in ultrathin CrX_3 differing from those of the bulk crystals. Using Raman spectroscopy, I connect these differences to changes in the lateral stacking arrangements between individual crystalline layers.

The techniques established to handle air-sensitive 2D magnets lay the groundwork for the discovery of novel magnetic phenomena in the many yet unexplored layered magnetic insulators. Moreover, the development of 2D magnetic tunnel junctions with large magnetoresistances and highly spin-polarized currents paves the way for integration in the spintronics community. Finally, the more complete understanding of the layer-dependent magnetism in ultrathin CrX_3 unlocks the potential to carefully incorporate 2D magnets in a variety of van der Waals heterostructures for proximity magnetism effects and beyond.

Thesis Supervisor: Pablo Jarillo-Herrero
Title: Professor of Physics

Acknowledgments

I have a number of people to recognize without whom I couldn't have completed this journey.

First and foremost, I am greatly indebted to my advisor, Prof. Pablo Jarillo-Herrero, for his guidance and support during the last six years. I appreciate the abundance of opportunities you have provided me to develop my skills as a well-rounded physicist beyond the lab and to foster meaningful collaborations around the world. Your encouragement to experiment with growth of new air-sensitive materials in our lab was vital in starting the field of 2D magnets.

Next, I owe so much to Dr. David MacNeill, who has worked alongside me the past four years. You have always been my cheerleader whenever I've felt discouraged (especially after many failed transfers in the glovebox) and never hesitated trying something new. I'm still amazed at your seemingly endless deep knowledge of every area of condensed matter physics and hope that at least some fraction has transferred to me.

Dr. Efrén Navarro-Moratalla, thank you for mentoring me as a fellow chemist-turned-physicist in the critical beginning stages of my PhD. You patiently devoted so much time to teach me both nanofabrication and the uncharted territory of crystal growth in the group. Without you, 13-2056 wouldn't have been transformed into the glovebox room we know and love today.

Daniel Rodan-Legrain, we've grown as physicists alongside one another and I can't imagine a lab without you. I have always valued your enthusiasm to bring the group together, whether it was to celebrate someone's recent success or to construct an elaborate game on a group trip. I'm looking forward to your own defense in the not-too-distant future and will miss hearing your daily greetings.

Dr. Valla Fatemi, you were one of the first people I met at MIT and in my mind shaped our group's culture. I enjoyed our many discussions in the office together, including those at odd hours of the night. Even though we never directly collaborated, I still learned so much from you.

Märta Tschudin, it was such a delight to have you as a member of our subteam. Our shared passion for van der Waals magnets, especially the bright purple crystals, made working with you so much fun. I owe you a visit one day before it's your turn to graduate.

Liqiao Xia, I wish we could have worked together for longer. Your inquisitive spirit has made me deepen my own understanding of our projects and I can tell that you have a bright career lying ahead.

To the present and former members of the Jarillo-Herrero group: Mallika Randeria, Joel Wang, Qiong Ma, Clément Collignon, Kenji Yasuda, Yafang Yang, Yaqing Bie, Xirui Wang, Jane Park, Isaac Zheng, Isabelle Phinney, Yuan Cao, Sanfeng Wu, Denis Bandurin, Javier Sanchez-Yamagishi, Landry Bretheau, Sergio de la Barrera, Yonglong Xie, and Xueqiao Wang. I've been so privileged to work amongst such talented scientists over the course of my PhD. You've shared insights with me about truly everything, ranging from fabrication details to life advice. I'll always remember our many adventures together in Cambridge and our group trips to the mountains and the sea.

Prof. Xiaodong Xu, I would like to express my gratitude for welcoming me into your lab on numerous visits. Our collaborations played a pivotal role in my PhD and I have learned so much from discussions with your group.

To Bevin Huang and the rest of Xu Group, thank you for showing me around your lab and the city. You made me feel like a true part of the team and always kept me heavily caffeinated with superb Seattle coffee during the long hours of MOKE measurements.

To Luiz Pimenta Martins, Linda Ye, Alfred Zong, Su-Yang Xu, Spencer Tomarken, Carina Belvin, Qi Song, and the rest of the CMX community, you have all enriched my experience on the floor over the past six years. I'll miss our hallway chats, meals together in the lounge, and frequent greetings throughout the day.

To my friends roaming around MIT outside of CMX: Cyprian Lewandowski, Emily Crabb, Sameer Abraham, Constantin Weisser, Rey Cruz Torres, Oscar Moll, Ryuji Takagi, Libby Tolman, Tom Boettcher, Graeme Sutcliffe, John Hardin, Neel Kabadi, Alex Siegenfeld, and many more. We've enjoyed so many fun memories together and I'm going to miss not being able to share my baked goods with such wonderful friends.

To the past and present members of Graduate Womxn in Physics, you have provided a special place during my time here at MIT. I won't take for granted having such a strong GWIP community during my PhD.

Monica Wolf, you've kept all of CMX afloat for so many years. I cherished having you next door and already miss our frequent conversations and knowing there isn't a problem you can't solve.

To Prof. Nuh Gedik and Prof. Anna Frebel, thank you for serving on my thesis committee and taking the time to review this thesis.

To Grace Truong, Laura Doherty, Julia Steinberg, Chris Wang, Jordan Driskill, Noah Rubin, Nathan Koocher, Nathan Weinbren, and other friends outside of MIT, thank you for reminding me that there is a world beyond research and helping me laugh during stressful times.

Ethan, it's been a privilege to have you as my brother and incredibly special to share MIT with you the past three years (even though you beat me to MIT first). I would always look forward to our breakfast meetups and valued running into each other surprisingly often in the Infinite.

Finally, to Ema and Abba, words cannot express how grateful I am for everything you have done for me. You have been the most unquestionably supportive parents I could ask for, even though you're not entirely sure what I do all day. Thank you for encouraging me to pursue my goals. I dedicate this thesis to you.

Contents

List of Figures

List of Tables

Chapter 1

Introduction

Since the use of iron-containing lodestones as the world's first compasses more than two millennia ago, magnetism has played a key role in human life. Technological developments have now incorporated magnets into almost every facet of our world. Today, they are widely used to store data in hard disk drives. Every swipe of a credit or ID card transmits information encoded in its magnetic strip. Medical tools, such as MRI machines, rely on large magnetic fields to image internal organs. Within our smartphones, magnetic sensors serve as modern-day lodestones to help us orient ourselves.

Underlying all of these systems is the spontaneous alignment of electrons' spins within a magnetic material, a phenomenon deeply rooted in quantum mechanics. From a condensed matter physics perspective, magnets offer us ample opportunity to explore various complex magnetic phases, both in intrinsically magnetic crystals and through engineered heterostructures with other materials. This thesis centers around the discovery of magnetism in a new platform: layered two-dimensional (2D) van der Waals crystals which are only a few atoms thick. The following chapter introduces the broad family of van der Waals materials, including its recently discovered magnetic members. Chapter 2 focuses on the chromium trihalides, a key family of magnetic insulators, which are the topic of the experiments presented in this thesis. Chapter 3 outlines different techniques used to study magnetism in the thin limit. Chapters 4 through 7 then detail several experiments probing magnetic order in the ultrathin chromium trihalides. Finally, Chapter 8 concludes with an outlook for the burgeoning field of van der Waals magnetism.

1.1 van der Waals Materials

In a typical three-dimensional (3D) crystal, strong covalent or ionic bonds between atoms hold the material together in all directions. In contrast, van der Waals materials are a wide class of crystals composed of 2D sheets of tightly bound atoms that are only held together by weak van der Waals forces. This unique feature allows for individual layers to be peeled apart from one another while preserving crystallinity within each layer. The most famous of these materials is graphene, a single layer of graphite comprised of sp^2-hybridized carbon atoms arranged in a honeycomb lattice. It gained widespread attention in 2004 when researchers first isolated graphene using Scotch tape to separate the layers [1,2], ultimately leading to the 2010 Nobel Prize in Physics. These early results opened up a new field of 2D materials research, not only to study graphene, but also to explore other cleavable crystals that can be isolated to the monolayer limit.

Beyond graphene, there are thousands of predicted van der Waals materials [10], many of which have now been experimentally studied. These materials cover a vast range of desirable physical properties, including metals, semiconductors, insulators, semimetals, superconductors, topological insulators, and magnets. More recent in-

Table 1.1: Diverse properties of van der Waals materials

Material	**Property**
Graphene [1]	Semimetal
BN [3]	Insulator
MoS_2 [4]	Semiconductor
Bi_2Se_3 [5]	Topological insulator
$NbSe_2$ [6]	Metal/superconductor
CrI_3 [7]	Magnetic insulator
$Cr_2Ge_2Te_6$ [8]	Magnetic semiconductor
Fe_3GeTe_2 [9]	Magnetic conductor

vestigations have revealed exotic materials with tunable quantum phases that can be accessed in a single device [11, 12]. Importantly, they often reveal different physical properties than their parent bulk 3D crystals due to changes in band structure [4], crystal structure [13], and phase transitions [6]. They can also have layer-dependent properties in the few-layer limit. For example, monolayer graphene is a semimetal with a linear dispersion at the Fermi level [1, 2]. Bilayer graphene, on the other hand, is a semimetal with a quadratic dispersion at the Fermi level and can have a tunable band gap controlled by a vertical electric displacement field [14]. Some key examples of the diverse properties within the family of van der Waals materials are listed in Table 1.1.

1.1.1 Advantages of 2D Materials

There are several attractive features of 2D materials that give them advantages over both their parent 3D crystals and thin films grown from bottom-up synthesis techniques.

First, the ability to transfer few-layer crystals on top of one another opens up the possibility to construct countless new artificial materials, called van der Waals heterostructures. Since these crystals are only a few atoms thick, they are extremely sensitive to their local environment. As a result, proximity effects can transform a few-layer crystal when placed in direct atomic contact with another material. For example, reports have demonstrated proximity-induced spin-orbit coupling (SOC) in graphene on WS_2 [15, 16], the anomalous Hall effect (AHE) and the Zeeman spin Hall effect (ZSHE) in graphene on thin films of the magnetic insulators yttrium iron garnet (YIG) and EuS [17, 18], and valley splitting of WSe_2 on CrI_3 by the induced magnetic exchange field [19].

Second, unlike a bulk crystal, 2D materials are highly susceptible to gate voltages to tune their properties. We can build up a parallel-plate capacitor using the 2D insulator hexagonal boron nitride (BN) as a gate dielectric and treating our few-layer crystal of interest as one plate of the capacitor. The other electrode can either be another van der Waals crystal, such as graphene, or a metallic thin film. By adding a second gate dielectric and electrode, we can use the top and bottom gate voltages to independently tune the flake's carrier density n and apply a displacement electric field $\vec{D}_\perp$. We can thus achieve *in situ* fine-tuned control over the Fermi level, band structure, and resulting properties of the material. In contrast, doping a bulk crystal requires elemental substitution within the entire crystal lattice (*e.g.* changing the doping amount in the cuprate family of high-T_c superconductors). For bulk crystals, the growth of an entirely new single crystal sample is necessary each time one wishes to slightly alter the carrier density, rather than simply tweaking an applied gate voltage *in situ* during a measurement.

Third, van der Waals materials have the advantage of substrate independence. Epitaxially grown thin films, while quite flat and possessing many of the same desirable properties as van der Waals materials, must adhere to the lattice of the underlying substrate. They also often contain dangling bonds, significant surface reconstruction, free radicals, or even form covalent bonds with the substrate. This is contrasted with van der Waals heterostructures, which are only weakly coupled to the substrate through van der Waals interactions. We therefore have the choice of the final substrate to suit the requirements of a particular experiment. Van der Waals stacks can be placed onto substrates like sapphire for optical measurements to minimize background signal, aligned to pre-patterned metallic electrodes for electrical measurements, and even be suspended as a membrane across a trench.

Fourth, the twist degree of freedom in van der Waals crystals gives rise to a large parameter space for exciting and surprising physics discoveries. Heterostructures can depend quite sensitively on the relative angles of the individual layers. The moiré superlattice from the stacking arrangements of atoms in adjacent layers introduces a new electrostatic potential with the periodicity of a large moiré unit cell up to tens of nanometers in size. In comparison, the lattice spacing of graphene is just 0.142 nm. Scattering from this superlattice potential consequently leads to a much smaller Brillouin zone in reciprocal space, which can renormalize the band structure of the original material. The resulting phenomena were observed in the early days of graphene research when graphene placed on boron nitride revealed beautifully rich physics including the fractal Hofstadter's butterfly [20, 21]. More recently, the discovery of superconductivity [22] and correlated insulator states [23] in twisted bilayer graphene aligned near the so-called magic angle of 1.1° has resulted in a renewal of interest in tunable moiré physics, both in few-layer graphene and in other 2D materials [24–29]. Advances in experimental techniques and theoretical understanding of these systems will likely continue to reveal new surprises for condensed matter physicists in the coming years.

1.1.2 Mechanical Exfoliation and van der Waals Assembly

The extremely weak interlayer van der Waals forces holding together individual sheets of a van der Waals crystal enables one to easily peel apart and isolate layers in a process called mechanical exfoliation. To achieve this, one starts by placing a bulk 3D crystal onto a piece of adhesive tape. By taking a second piece of tape, gently pressing it on top of the first, and separating the tapes, one can cleave the crystal in half. As one repeats this process several times, the crystal cleaves into increasingly thinner layers. One can then press one of these tapes onto a substrate, typically Si coated with a thin layer of SiO_2, and slowly peel off the tape. The resulting crystals on the substrate are of varying shapes and thicknesses, typically tens of microns across and below 100 nm thick. Using an optical microscope, one can identify these nanoflakes based on their optical contrast in order to determine the thickness of monolayer and few-layer crystals [30]. The thickness of the SiO_2 layer modifies the optical contrast values and can be selected for optimizing the contrast relative to the substrate background for few-layer crystals of different materials.

Once the crystals have been identified, they can be stacked into a heterostructure using a dry-transfer van der Waals assembly process [31]. A poly(bisphenol A carbonate) (PC) film is first stretched over a polydimethylsiloxane (PDMS) block mounted on a glass slide. Using mild heat, one can pick up the first flake in the heterostructure from its substrate onto the PC film. Then, since the PC and PDMS are transparent, one can use an optical microscope and micropositioners to align the first flake with the next flake on a second substrate. The van der Waals forces between two atomically flat 2D crystals are stronger than the second crystal's weak interactions with the underlying rough substrate. Therefore, one can easily pick up the second flake with mild heat by relying on this van der Waals adhesion. Once all flakes have been picked up onto the slide, one can release the stack onto a final substrate by melting the PC at 160-170°C and remove the PC residue with a chloroform soak.

This van der Waals assembly process is integral to creating new artificial heterostructures combining different layered materials. Moreover, one can take advantage of 2D hexagonal boron nitride (BN), an inert insulator with a large band gap. SiO_2 suffers from a bumpy surface on the atomic scale, as well as dangling bonds and free radicals that introduce charge inhomogeneities [32]. BN has been established as a workhorse insulator to screen charges from the underlying SiO_2/Si substrate in van der Waals devices [33]. It is also now widely used as an inert capping layer to protect air-sensitive 2D crystals from degradation in the presence of water and oxygen.

1.2 van der Waals Magnets

During the initial boom of exploring cleavable 2D materials, a noticeable absence in this growing list was a few-layer crystal possessing long-range magnetic order. There was clearly a desire to introduce these materials to achieve long-standing goals for both fundamental physics, such as the quantum anomalous Hall effect (QAHE) [34] and the Kitaev quantum spin liquid (QSL) state [35], and applications, including low-power spintronics devices and topological quantum computing [36].

van der Waals magnets offer several benefits compared to other magnetic systems. First, their intrinsic magnetism is more robust than other thin magnets, like the class of dilute magnetic semiconductors. Those materials rely on defect engineering to introduce magnetic moments but consequently also introduce disorder [37]. Second, van der Waals magnets' ultrathin nature results in small magnetic volumes, which are well-suited for applications in high-efficiency, low-power spintronics devices [38]. Third, and perhaps most importantly, their ability to form van der Waals heterostructures with other layered materials unlocks endless possibilities for magnetic exchange interactions and other phenomena at the interface. In light of this, the twist degree of freedom also offers the unique opportunity to explore rich magnetic textures arising from modulated interlayer exchange interactions in the moiré superlattice of two twisted magnetic layers [39].

The Mermin-Wagner theorem [40] states that in the absence of magnetic anisotropy (*e.g.* for the isotropic Heisenberg model), spin-wave fluctuations at vanishingly low energies prohibit long-range magnetic order in two dimensions at finite temperature. For some time, it was believed that therefore two-dimensional magnetism could not exist. However, introducing magnetic anisotropy through magnetocrystalline anisotropy, spin-orbit coupling, or other means opens up a gap in the magnon spectrum, thereby stabilizing a long-range magnetic ground state with a finite Curie temperature.

In the mid-2010s, several candidate 2D magnetic materials were revisited decades after their discoveries as bulk crystals. One such material, CrI_3, was suggested as a cleavable ferromagnet [41]. It had been studied for over 50 years as a bulk ferromagnetic insulator with strong magnetic anisotropy perpendicular to the layers [42]. In 2017, we published a study using the magneto-optical Kerr effect (MOKE) to observe robust ferromagnetism persisting in monolayer CrI_3 [7] (see Chapter 4). At the same time, another study was published on MOKE experiments of ferromagnetic bilayer $Cr_2Ge_2Te_6$ (CGT) [8]. These initial works, together with an earlier Raman study exploring antiferromagnetism in monolayer $FePS_3$ [43], were met with great enthusiasm in the 2D materials community and established van der Waals magnets as a new field of research.

Since then, a number of van der Waals magnets have been theoretically proposed and experimentally verified in the few-layer limit. In the rest of this section, I will highlight some of the magnets studied so far. Several reviews on 2D magnets have assembled more comprehensive lists [38, 44–47], though the full family of materials is still ever-growing.

My PhD work has focused primarily on the insulating chromium trihalides (CrX_3, X = I, Br, Cl; see Chapter 2), especially CrI_3 and $CrCl_3$. Bulk CrI_3 [41] and $CrBr_3$ [48] are both out-of-plane ferromagnets, although CrI_3 was found to exhibit layered antiferromagnetism in the thin limit [7]. $CrCl_3$ is a layered in-plane antiferromagnet, both in the bulk [49] and few-layer [13] limits.

The transition metal trihalides (MX_3) are not limited to just CrX_3. One notable member is α-$RuCl_3$, a zigzag antiferromagnet that has gained attention as a candidate Kitaev QSL predicted to host fractionalized Majorana fermion excitations [50–56]. Other members include VX_3, including VI_3 with out-of-plane ferromagnetism [57], $FeCl_3$, and $FeBr_3$. $FeCl_3$ is a bulk antiferromagnet with helimagnetic order below 15 K [58], which has yet to be explored in the thin limit. In addition to the trihalides, there are also numerous magnetic van der Waals transition metal dihalides (MX_2) with a variety of bulk phases including helimagnetism and multiferroicity. A detailed overview of bulk MX_3 and MX_2 materials can be found in Ref. [44].

Another broad class of 2D magnets are transition metal chalcogenides. $Cr_2Ge_2Te_6$ (CGT) [8] and its sister compound $Cr_2Si_2Te_6$ (CST) [59] are both out-of-plane ferromagnetic semiconductors. The family of MPX_3 (M = transition metal, X = S or Se) magnets have also emerged as another class of insulating antiferromagnets with a range of ordering types. $FePS_3$ [43] and $FePSe_3$ [60] are Ising-type, $MnPS_3$ [61] and $MnPSe_3$ [60] are Heisenberg-type, and $NiPS_3$ is XY-type [62]. More recently, Fe_3GeTe_2 (FGT) was discovered to be the first conducting ferromagnetic monolayer magnet with itinerant ferromagnetism persisting up to 130 K (compared to 205 K in the bulk) [63]. Upon electrostatic doping with an applied gate voltage, however, its Curie temperature was pushed above 300 K in a trilayer device [9], making it a promising candidate for room temperature devices incorporating 2D magnetism. In addition, a study on $GdTe_3$, an antiferromagnetic metal, demonstrated very high bulk electron mobility of 60,000 cm^2/Vs and the ability to cleave into few-layer flakes [64].

An important subgroup of the transition metal chalcogenides are the magnetic topological insulators $MnBi_2Te_4 \cdot nBi_2Te_3$ [65]. $MnBi_2Te_4$ (MBT) is a van der Waals crystal comprising of alternating stacks of Bi_2Te_3, a well-known layered topological insulator, and MnTe, whose moments within each layer order ferromagnetically in the out-of-plane direction. In MBT, the MnTe planes couple antiferromagnetically, resulting in a layered out-of-plane antiferromagnet similar to thin CrI_3. Researchers observed the QAHE in a five-layer MBT crystal with zero applied field at 1.4 K [66] due to its net magnetic moment. When the spins were fully aligned with an external magnetic field of 7.6 T, the onset of QAHE was increased to 6.5 K. In a six-layer flake, MBT displayed a zero Hall plateau and large R_{xx}. These two signatures are indicative of the first experimentally demonstrated axion insulator state [67], which requires opposite magnetization in the top and bottom layers. These exciting studies on MBT have motivated tuning the interlayer magnetic coupling between the MnTe planes by adding additional layers of Bi_2Te_3 ($n \geq 1$). Researchers have achieved the transition to ferromagnetic interlayer coupling in bulk crystals of $MnBi_8Te_{13}$ with a T_C of 10.5 K [68], providing the opportunity to realize the QAHE at higher temperatures in less disordered systems than the magnetically-doped topological insulators.

Finally, a surprising class of van der Waals magnets has been uncovered in studies of moiré superlattices of 2D crystals containing non-magnetic elements [26–29]. Here, the underlying mechanism arises from orbital magnetic moments in the *K* and *K'* valleys of graphene, rather than from spin magnetic moments in conventional magnetic materials. Zero-field QAHE was observed in a device of magic-angle ($\theta = 1.15°$) twisted bilayer graphene aligned to hexagonal boron nitride. This discovery implies that this van der Waals heterostructure is an intrinsic out-of-plane QAH ferromagnet with an estimated Curie temperature of 7.5 K [28]. Moreover, current pulses of 20 nA were shown to reversibly switch the magnetization. The QAHE has also been observed in another electrically-switchable moiré system of twisted monolayer-bilayer graphene with a Chern number of 2 [29]. Finally, ABC-stacked trilayer graphene aligned to boron nitride also displays anomalous Hall behavior suggestive of orbital ferromagnetism [27]. These systems offer the exciting potential to study the interplay of magnetism, strong electron correlations, and topology in a new field of moiré magnetism.

Chapter 2

The Chromium Trihalides

In this chapter, I will focus on the chromium trihalides (CrX_3), the family of van der Waals materials I have primarily studied over the course of my PhD. The chromium trihalides have emerged as a leading class of layered magnetic insulators. While their crystal structures are similar, their magnetic ordering strongly depends on the halide ion. In the following sections, I will detail the various properties of the bulk CrX_3. Chapters 4 through 7 will explore what happens to the magnetic order in these systems when taken to the few-layer limit.

2.1 Bulk crystal structure

CrX_3 crystals are built up of layers with a three-atom-thick unit cell. Each unit cell is comprised of Cr^{3+} ions approximately arranged in a honeycomb lattice with edge-sharing octahedra of X^- ions, shown in Figure 2-1a. These layers are separated from one another by the van der Waals gap (Fig. 2-1b). At high temperatures, CrX_3 adopts a monoclinic crystal structure with space group $C2/m$ [41]. Upon cooling, CrX_3 undergoes a first-order crystallographic phase transition to a rhombohedral structure with space group $R\bar{3}$ [41]. The transition temperatures are 210 K, 420 K, and 240 K for CrI_3, $CrBr_3$, and $CrCl_3$, respectively [41, 69]. Thus, at room temperature, CrI_3 and $CrCl_3$ are in the monoclinic phase whereas $CrBr_3$ has already transitioned to the low-temperature rhombohedral phase.

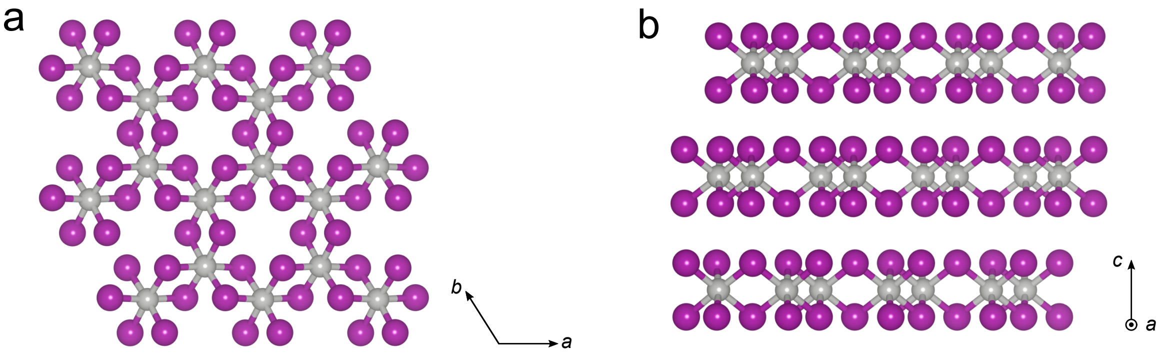

Figure 2-1: **a.** Bird's eye view of monolayer CrI_3 in the bulk low-temperature rhombohedral $R\bar{3}$ phase. **b.** Stacking of three CrI_3 layers in the $R\bar{3}$ phase. Each layer is separated from adjacent layers by the van der Waals gap. Crystal structures were rendered from crystallographic data in Ref. [41].

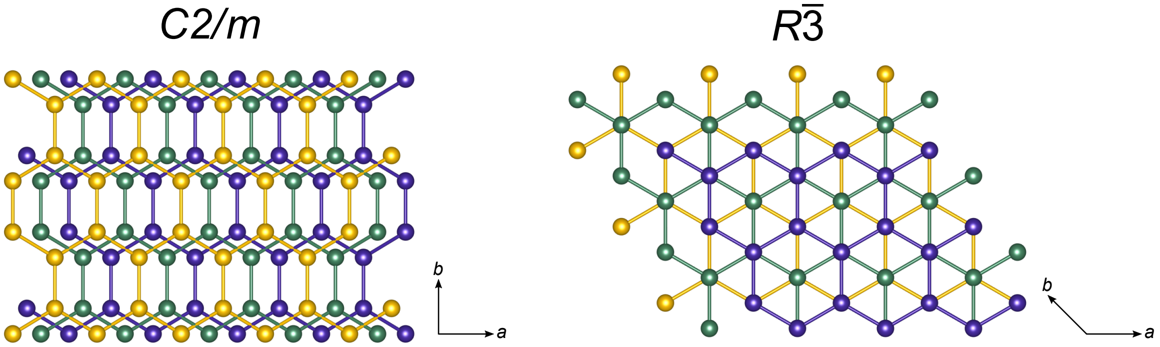

Figure 2-2: Stacking order of Cr^{3+} honeycomb lattices in three adjacent layers in the high-temperature monoclinic $C2/m$ phase (left) and the low-temperature rhombohedral $R\bar{3}$ phase (right).

While these two crystal structures obey different symmetries, the dominant effect of the phase transition is altering the stacking order between adjacent sheets in the crystal, shown in Figure 2-2. Without accounting for magnetic ordering, both structures are centrosymmetric.

2.2 Bulk magnetic order

2.2.1 Intralayer coupling

The local magnetic moments in CrX_3 can be understood in the framework of crystal field theory. Cr^{3+} has three valence electrons in its outermost $3d$ subshell, giving it a

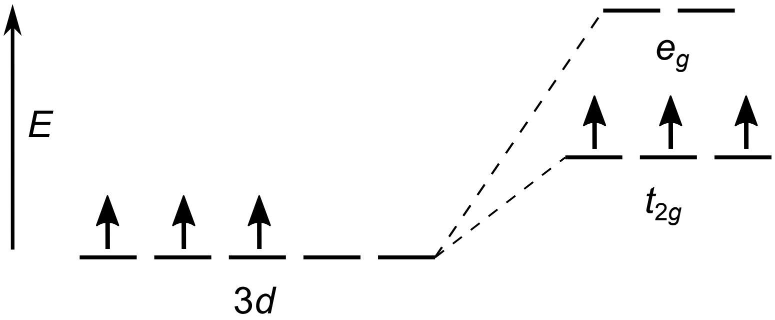

Figure 2-3: Crystal field splitting diagram for Cr^{3+} ions in an octahedral environment. The three free electrons half-fill the t_{2g} subshell.

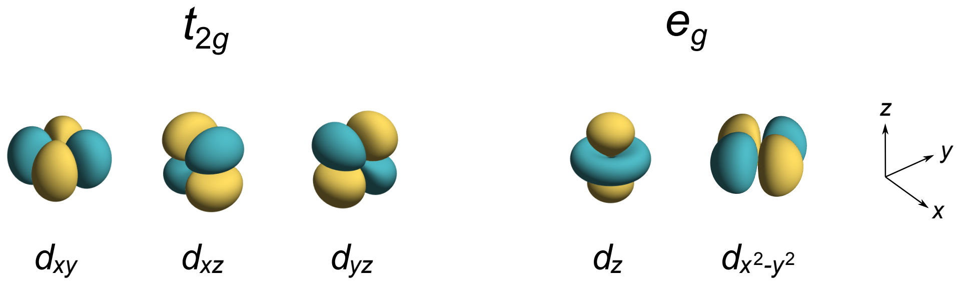

Figure 2-4: $3d$ orbitals are divided into off-axis lower energy t_{2g} (left) and on-axis higher energy e_g (right) subshells by an octahedral crystal field.

$3d^3$ electron configuration. By approximating an octahedral environment of X^- ions surrounding each Cr^{3+}, we can think of each Cr^{3+} ion as experiencing an octahedral crystal electric field. The six negatively charged X^- ions along the $\pm x$, $\pm y$, and $\pm z$ axes lead to an anisotropy in the Coulomb repulsion experienced by electrons in the on-axis and off-axis $3d$ orbitals. This anisotropy, termed crystal field splitting, breaks the degeneracy between the five $3d$ orbitals, resulting in three off-axis lower energy orbitals (d_{xy}, d_{yz}, d_{xz}) in the t_{2g} subshell and two on-axis higher energy orbitals (d_{z^2}, $d_{x^2-y^2}$) in the e_g subshell. In order to minimize energy, the three available electrons will half-fill the t_{2g} subshell and align with the same spin configuration following Hund's rule (Figure 2-3).

The magnetic moments in the chromium trihalides are localized on these Cr^{3+} ions, which each contain a total spin $S = 3/2$ from the three unpaired t_{2g} electrons. The orbitals in the t_{2g} and e_g subshells are depicted in Figure 2-4.

In all of the chromium trihalides, the moments on Cr^{3+} ions within the same layer align ferromagnetically. This ferromagnetic intralayer exchange can be understood by superexchange (SE) interactions between the half-filled t_{2g} and nearest-neighbor (NN) empty e_g orbitals, mediated by filled X^- p orbitals [70–74]. Direct exchange between the NN Cr^{3+} ions is unlikely to strongly contribute to the magnetic order due to the larger Cr-Cr bond distances (3.96 Å in CrI_3 [41]) compared to the shorter Cr-I bond distances (2.72 Å in CrI_3 [41]). The Goodenough-Kanamori rules [72,73] predict that the nearly 90° Cr-X-Cr bond angles should result in ferromagnetic coupling between moments on NN Cr^{3+} ions. The Pauli exclusion principle prevents pairing of the exchanged electron with an electron in a half-filled t_{2g} orbital on the NN site, while Hund's rule aligns the electron's spin in the e_g orbital with the existing unpaired electron spins in the t_{2g} subshell.

In the very simplest approximation, a single layer of the chromium trihalides can be cast in terms of the Heisenberg model on a honeycomb lattice with the addition of anisotropy terms. In the absence of anisotropy, the isotropic Heisenberg spin Hamiltonian is given by:

$$\mathcal{H} = -J \sum_{<ij>} \vec{S}_i \cdot \vec{S}_j \tag{2.1}$$

where J is the exchange between NN on the Cr^{3+} honeycomb lattice and $< >$ denotes the sum over NN. Taking $J > 0$, the system's energy is minimized when the spins align ferromagnetically. In the cases of CrI_3 and $CrBr_3$, magnetic anisotropy gives rise to a perpendicular easy axis, which can be approximated by the Hamiltonian:

$$\mathcal{H} = -J \sum_{<ij>} \vec{S}_i \cdot \vec{S}_j - \lambda \sum_{<ij>} S_i^z S_j^z \tag{2.2}$$

where λ is the anisotropic symmetric exchange arising from spin-orbit coupling of I or Br [75]. A Dzyaloshinskii–Moriya (antisymmetric) exchange term between NN is forbidden due to the inversion center of the NN Cr-Cr bond. In $CrCl_3$, on the other hand, shape anisotropy effects result in an easy-plane anisotropy within the plane of the crystal. It is best described by Eq. 2.1 with the addition of in-plane anisotropy terms.

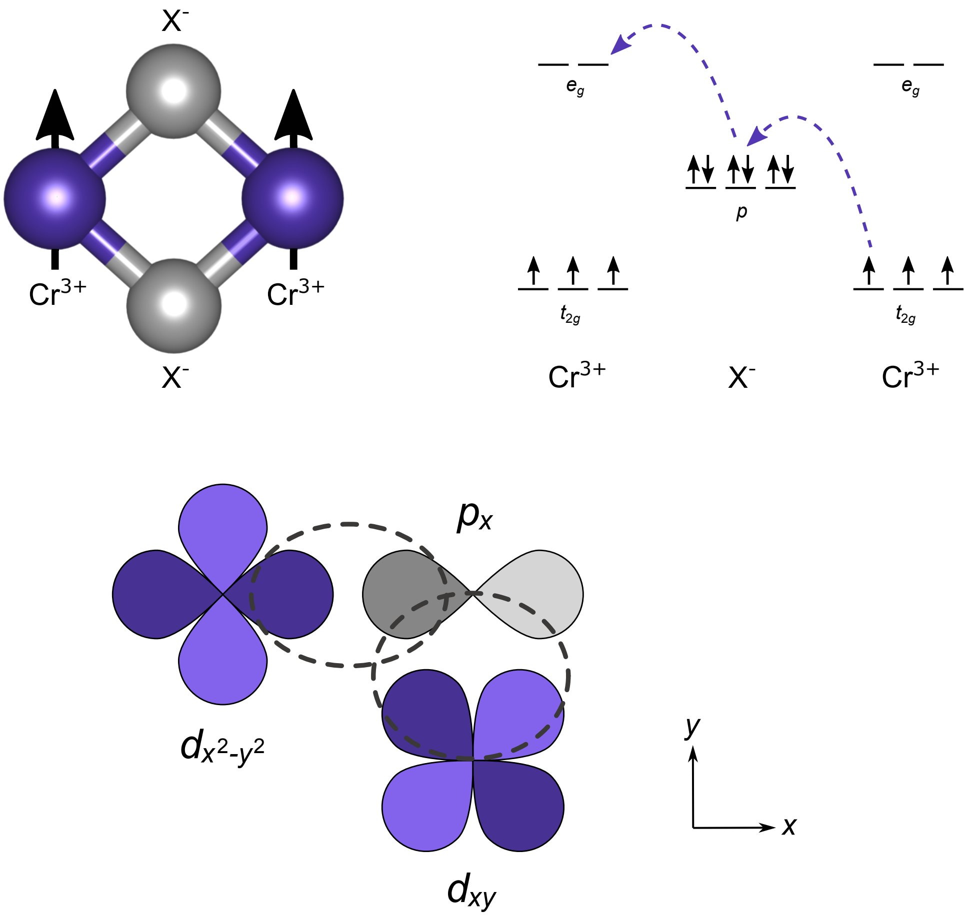

Figure 2-5: Top left: Superexchange mechanism for nearest-neighbor Cr^{3+} ions mediated by the shared X^- ions at near-90° bond angles. Top right: Orbital energy diagram showing the electrons involved in the superexchange mechanism between the three ions. Bottom: Example of orbital overlap for two nearest-neighbor Cr^{3+} sites. The electron from the half-filled d_{xy} orbital on one Cr^{3+} site can hop from the X^- p_x orbital to the empty $d_{x^2-y^2}$ orbital on the neighboring Cr^{3+} site.

These spin Hamiltonians serve to provide a basic understanding but do not capture the full scope of the intralayer magnetic behavior in the chromium trihalides. Additional anisotropy terms and magnetic exchange terms between further Cr neighbors are required. Different frameworks including those incorporating next-nearest neighbor Dzyaloshinskii–Moriya exchange or dominant NN Kitaev interactions (instead of Heisenberg) have also been used to model the magnetic behavior in $\mathrm{CrI_3}$ [76, 77]. Ongoing studies of bulk $\mathrm{CrI_3}$ crystals are actively seeking to resolve which of these terms are most appropriate and estimate the values of their parameters [78–80]. Future work will likely further refine these terms and converge on a full spin Hamiltonian to describe the magnetism in these anisotropic systems.

2.2.2 Interlayer coupling

The interlayer magnetic coupling across the van der Waals gap depends on a more complicated exchange pathway between the nearest $\mathrm{Cr^{3+}}$ ions in different layers, now mediated by the p orbitals of two $\mathrm{X^-}$ ions, one on either side of the van der Waals gap. This mechanism, termed super-superexchange (SSE), is directly impacted by the stacking order of adjacent layers shown in Figure 2-2 [81–84]. Changing the stacking configuration will alter the wave function overlaps and exchange integrals for electrons across the four ions, thereby modifying the strength and even sign of the interlayer exchange arising from this SSE interaction.

The bulk magnetic order varies across the three chromium trihalides, as shown in Figure 2-6. $\mathrm{CrI_3}$ and $\mathrm{CrBr_3}$ are both ferromagnets with an out-of-plane easy axis, while $\mathrm{CrCl_3}$ is an antiferromagnet with an *ab*-plane easy plane. Individual ferromagnetic layers of $\mathrm{CrCl_3}$ have moments that lie in-plane but couple antiferromagnetically. Each layer's magnetization is oriented 180° relative to adjacent layers across the van der Waals gaps. The chromium trihalides magnetically order below the ferromagnetic Curie temperature ($T_\mathrm{C} = 61$ K for $\mathrm{CrI_3}$ [41], 37 K for $\mathrm{CrBr_3}$ [48]) or antiferromagnetic Néel temperature ($T_\mathrm{N} = 14$ K for $\mathrm{CrCl_3}$ [49]).

Based on the localized moment picture of $\mathrm{Cr^{3+}}$ ions with $3d^3$ electron configurations, we should expect a magnetic moment of approximately $3\mu_\mathrm{B}$ per Cr site.

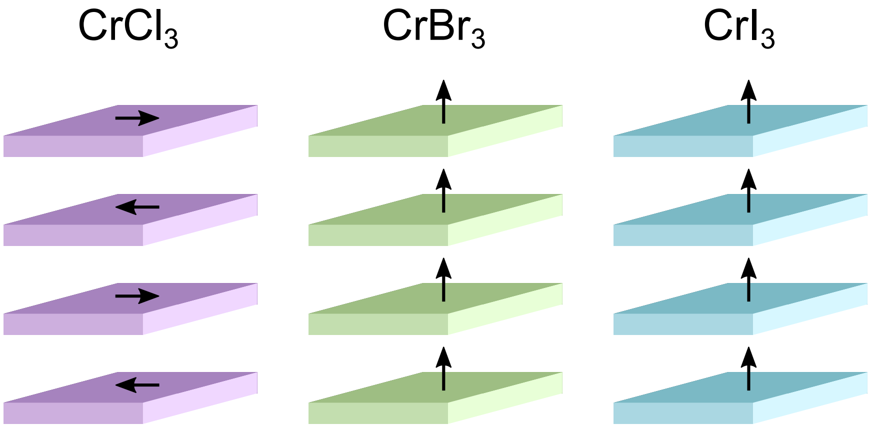

Figure 2-6: Bulk magnetic order of the three chromium trihalides.

Indeed, neutron diffraction and magnetic saturation studies have demonstrated that $\mathrm{CrX_3}$ have ordered moments of $2.7-3.2\mu_\mathrm{B}$ for $\mathrm{CrCl_3}$ [58], $3\mu_\mathrm{B}$ for $\mathrm{CrBr_3}$ [48], and $3.1\mu_\mathrm{B}$ for $\mathrm{CrI_3}$ [41,42]. The magnetic anisotropy depends heavily on the halide ions. It is strongest in $\mathrm{CrI_3}$, whose I $5p$ orbitals have the largest degree of SOC. $\mathrm{CrI_3}$ requires an in-plane applied magnetic field close to 3 T to orient the moments in-plane at 2 K [41, 42], compared to only 0.5 T for $\mathrm{CrBr_3}$ [48] with weaker SOC in its Br $4p$ orbitals. $\mathrm{CrCl_3}$ has the weakest magnetic anisotropy, arising predominately from shape effects to minimize dipolar interactions. It requires only a small field of $0.2-0.25$ T to overcome the antiferromagnetic coupling and align ferromagnetically within the *ab* plane [49, 85].

2.3 Bulk electronic properties

If one were to ignore all exchange interactions (*e.g.* in performing a DFT calculation), one would obtain a series of bands stemming from the Cr $3d$ t_{2g} orbitals. These bands would be half-filled and result in metallic or semimetallic behavior [82]. An intuitive understanding would be to think of the crystal field picture in Fig. 2-3, where each Cr^{3+} site has three unpaired t_{2g} electrons (half-filled orbitals).

However, exchange interactions are exceedingly important in $\mathrm{CrX_3}$ and lead to their insulating behavior. On-site ferromagnetic exchange interactions, arising from the half-filled t_{2g} and empty e_g states in each Cr atom, split the energy bands into spin-majority (up, $\uparrow$) and spin-minority (down, $\downarrow$) bands. These on-site interactions are present even in the absence of long-range order, and thus even above the Curie or Néel temperature. Other exchange mechanisms (*e.g.* intralayer superexchange and interlayer super-superexchange) are much smaller compared to the on-site exchange.

The conduction and valence bands in $\mathrm{CrX_3}$ have mostly Cr $3d$ character with only small contributions from the X p orbitals [82, 86]. The valence and conduction bands are two clusters of flat bands below and above the Fermi level coming from Cr $t_{2g\uparrow}$ and $e_{g\uparrow}$ contributions, respectively. The resulting band gaps are large, exceeding 1 eV for $\mathrm{CrI_3}$ and increasing with smaller halide atomic mass. The spin-minority $t_{2g\downarrow}$ bands sit above the conduction band of $e_{g\uparrow}$, reflecting the very strong on-site exchange interaction splitting the t_{2g} majority and minority spins.

This insulating behavior is analogous to the Mott transition. In a traditional Mott insulator, strong on-site Coulomb interactions (without spin sensitivity) lead to a large energy penalty to put an electron on the same site. Similarly, in $\mathrm{CrX_3}$, the on-site exchange interaction, essentially a type of spin-dependent Coulomb interaction between electrons, introduces an energy cost to put a spin-down electron in a t_{2g} orbital on the same site. These strong electron interactions driving highly insulating behavior limit transport measurements of $\mathrm{CrX_3}$, but enable electron tunneling processes when $\mathrm{CrX_3}$ are used as tunnel barriers (see Chapters 6 and 7).

Chapter 3

Probing magnetism in van der Waals materials

The introduction of ultrathin van der Waals magnets has necessitated new methods to study magnetism in these crystals just a few atoms thick. Fortunately, many techniques employed for thin magnetic films have been adapted for van der Waals magnets over the past several years. This chapter highlights some of these techniques, both those discussed in detail in this thesis and elsewhere. Several methods for studying bulk crystals are also outlined in this chapter.

3.1 Magnetometry of 3D systems

There are numerous established techniques to probe magnetic order in 3D crystals. These include vibrating-sample magnetometry (VSM) [87], SQUID magnetometry [88], and neutron diffraction [89].

VSM is among the easiest characterization tools for bulk samples. It operates by vibrating the sample perpendicular to an applied DC magnetic field [87]. The magnetic field from the magnetized sample will also oscillate, which induces a voltage in a set of detection coils that are fixed in position. The signal is compared to those produced by a permanent magnet reference with known magnetization and its own set of coils, allowing for a quantitative comparison. By changing temperature, applied

DC magnetic field strength, and sample orientation, one can thus fully map out the magnetization of a bulk sample. In our experiments, we used a commercial system (MPMS3 SQUID-VSM from Quantum Design) to perform magnetization studies on our bulk CrI_3 crystals. The results are shown in Fig. 3-1 and reproduce previously reported data for CrI_3 [41].

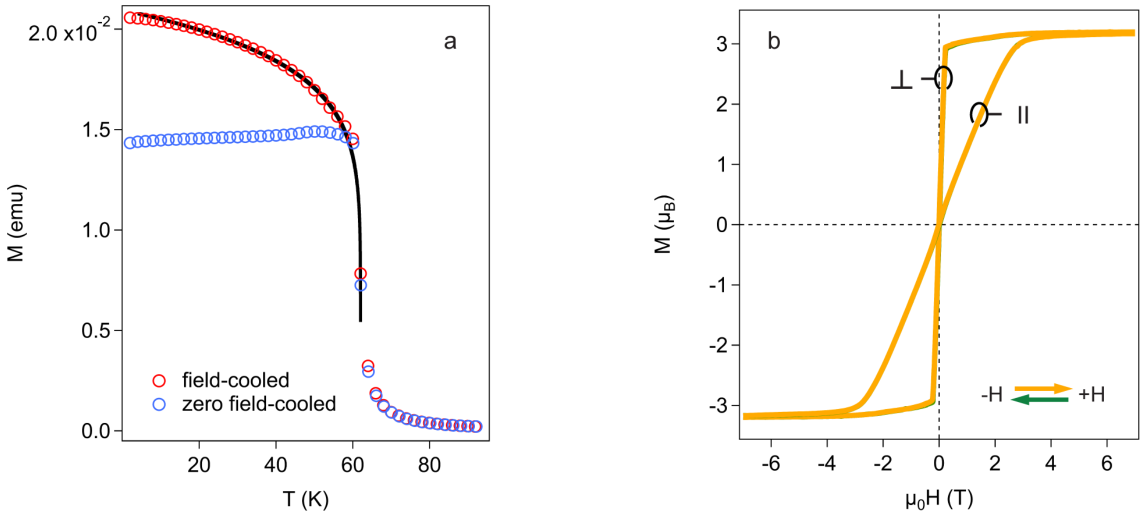

Figure 3-1: SQUID-VSM magnetometry in bulk CrI_3 (reproduced from Ref. [7]). **a.** Zero-field-cooled/field-cooled temperature dependence of the magnetization of a CrI_3 bulk crystal with an applied magnetic field of 1 mT perpendicular to the basal plane of the sample. The black line is a criticality fit ($M = \alpha(1 - T/T_\mathrm{C})^\beta$) of the data with $T_\mathrm{C} = 61$ K and $\beta = 0.125$ (Ising universality class). The units along the y-axis are electromagnetic units (emu). **b.** Hysteresis loops of the same sample with the external magnetic field in perpendicular and parallel orientations with respect to the CrI_3 layers. The magnetization along the y-axis is normalized per Cr atom.

Fig. 3-1b shows typical magnetic hysteresis curves for the bulk ferromagnet CrI_3. The magnetization fully saturates with a small applied perpendicular field $\mu_0 H_\perp$, whereas it takes several Tesla to saturate with $\mu_0 H_\parallel$. Together, these curves point to a strong out-of-plane magnetic anisotropy in bulk CrI_3.

3.2 Optical probes of 2D magnetism

3.2.1 MOKE and RMCD spectroscopy

One of the best-suited methods to probe thin film magnetism is the polar magneto-optical Kerr effect (MOKE), which uses linearly-polarized (LP) light incident on a flat sample to detect its magnetization. In a magnetic material, the complex dielectric tensor $\boldsymbol{\varepsilon}$ contains nonzero off-diagonal terms $\tilde{\varepsilon}_{xy} = -\tilde{\varepsilon}_{yx} \propto M_z$ [7, 90]. When right- or left-circularly polarized light (RCP and LCP, respectively) is reflected off of the surface, it adopts a Fresnel coefficient $\hat{r}_\pm = r_\pm e^{i\theta_\pm}$ [91]. Here, $\hat{r}_+$ and $\hat{r}_-$ denote RCP and LCP reflection coefficients, respectively. If $M_z = 0$, then $r_+ = r_-$ and $\theta_+ = \theta_-$. However, in the case of finite out-of-plane magnetization in the sample, these reflected amplitudes and phases are no longer equivalent for RCP and LCP due to the off-diagonal components of $\boldsymbol{\varepsilon}$.

LP light is an equal combination of RCP and LCP light. When LP light incident along the z-axis is reflected off of a magnetized thin film, the phase shifts θ_+ and θ_- become unequal, resulting in reflected light having elliptical polarization with a semimajor axis rotated by the Kerr rotation $\theta_K \equiv -\frac{1}{2}(\theta_+ - \theta_-)$ relative to the original polarization axis [91]. One can then use a quarter-wave plate to convert this light back into LP light with its polarization axis rotated by θ_K relative to the incident light (see Section 4.7 for a detailed discussion of the experimental MOKE setup).

A very similar measurement technique to MOKE is reflectance magneto-circular dichroism (RMCD) spectroscopy. Using the same Fresnel coefficients described above, one instead focuses on the change in the amplitudes r_+ and r_-. The RMCD signal is defined as $\Delta R/R \equiv \frac{1}{2}(r_+^2 - r_-^2)/(r_+^2 + r_-^2)$ [91]. In effect, RMCD is measuring the reflected elliptically polarized light with the semimajor axis along the same polarization axis as the incident light to extract the same magnetic information as MOKE. The work described in Chapter 5 utilizes both MOKE and RMCD signals in the same experimental setup.

These techniques are powerful tools to detect out-of-plane magnetization in a magnetic material such as $\mathrm{CrI_3}$. By tracking the evolution of θ_K or $\Delta R/R$ in the presence of an applied out-of-plane magnetic field, we can construct hysteresis loops to learn about the layer-dependent magnetic behavior in few-layer 2D van der Waals materials [7]. However, these methods are only sensitive to out-of-plane magnetization, making them impractical for sensing in-plane magnetic order found in $CrCl_3$ and other magnets.

3.2.2 Magneto-photoluminescence

Another light-matter interaction influenced by magnetism is photoluminescence (PL). Different helicities of light (RCP and LCP) selectively excite spin-up and spin-down electrons in a material. This coupling to electron spin manifests in polarization-dependent PL emission in a magnetic material, termed magneto-PL or helical PL.

In a work not shown in this thesis [92], we used magneto-PL spectroscopy to study CrI_3 down to the monolayer limit. We excited CrI_3 with LP light (an equal superposition of RCP and LCP which does not break time-reversal symmetry) and then separately detected the RCP and LCP components of the emitted PL. Below T_C, we observed a large spontaneous polarization of the PL, defined as $\rho \equiv (I_+ - I_-)/(I_+ + I_-)$, where I_+ and I_- are the peak intensities of RCP and LCP PL, respectively. Spin relaxation mechanisms can flip spins prior to relaxation through the emission of a photon, resulting in ρ less than unity but nonetheless indicative of a net magnetization. More recently, a similar study on magneto-PL of $CrBr_3$ [93] demonstrated large helical polarization of a monolayer flake of $CrBr_3$ [93]. Furthermore, these two works have also revealed new information about the $d-d$ transitions in CrX_3, which can be thought of in terms of molecular orbitals constructed from Cr $3d$ t_{2g} and e_g orbitals and X p orbitals [92]. Thus, optical studies can deepen our understanding of the electronic structure of these materials in addition to their magnetic order.

3.2.3 Raman spectroscopy

Raman spectroscopy is another heavily utilized optical method to probe ultrathin magnetic samples. It measures the inelastic light scattering off of thin films that occurs when incident light couples to collective mode oscillations in a solid. The resulting frequency shift, typically expressed in units of cm^{-1}, gives the energy of those excitations. Raman is most commonly used as a spectroscopic tool to detect phonons, which are quantized lattice vibrations. However, it can also be used to detect signatures of short-range and long-range magnetic order in a sample.

The first evidence for long-range order in a monolayer 2D crystal came from a Raman study of monolayer $\mathrm{FePS_3}$, a zigzag antiferromagnet [43]. Upon cooling below T_{N}, a phonon mode abruptly split, which can be explained by in-plane 2D Brillouin zone folding from the onset of magnetic order, thereby doubling the unit cell size. Other Raman studies on van der Waals magnets have identified magnons [94], which are quantized spin-wave excitations, and evidence of spinons [53], which are fractional magnons in frustrated magnetic systems like quantum spin liquids. Magnetic order can also modify the selection rules governing which phonon modes are Raman active. For example, magneto-electrical switching of magnetic order in bilayer $\mathrm{CrI_3}$ was recently demonstrated as a novel control mechanism of its Raman spectrum [95].

3.3 Spin-filter magnetic tunnel junctions

When an electron encounters an energy barrier, quantum mechanics tells us that there is a small probability of the electron tunneling across the barrier, unlike what one would expect from classical mechanics. One can make use of this fact to construct a tunnel junction comprised of two conducting electrodes sandwiched by a thin insulating tunnel barrier. Applying a finite bias voltage between the two electrodes enables transmission of electrons across the barrier, illustrated schematically in Fig. 3-2a. The DC bias voltage establishes an electric field across the insulating layer, resulting in a trapezoidal potential barrier.

There are three main types of transmission across the barrier. First, at low applied bias voltage, electrons can tunnel across the full width d of the barrier in what is called direct tunneling (DT in Fig. 3-2a). Second, as the bias energy eV is increased,

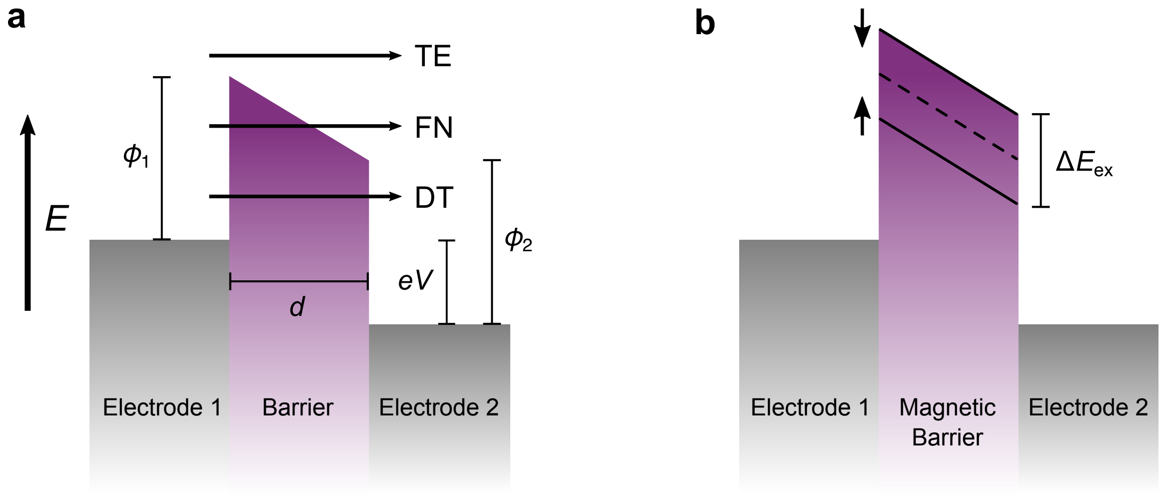

Figure 3-2: Tunnel junctions with a finite bias between the electrodes. **a.** There are three types of transmission regimes across an insulating barrier: direct tunneling (DT), Fowler-Nordheim tunneling (FN), and thermionic emission (TE) at high temperature. **b.** In a magnetic barrier, magnetic exchange splitting (ΔE_{ex}) results in different barrier heights for spin-up (↑) and spin-down (↓) electrons.

electrons can begin to tunnel through the slanted top of the trapezoidal barrier in the Fowler-Nordheim regime (FN in Fig. 3-2a) [96]. Third, at high temperature, the electrons emitted from an electrode can have enough thermal energy to enter the conduction band of the insulating barrier. In this case, called thermionic emission (TE in Fig. 3-2a), they are transported across without the use of tunneling. However, this transmission mechanism typically requires elevated temperatures well above the range used in tunneling measurements.

The current density of tunneling electrons can be modeled using Simmons' formula [97]. In his derivation, he uses the WKB approximation for the probability of tunneling across a 1D barrier and assumes an isotropic Fermi-Dirac distribution of electrons in each electrode. The resulting formula for the tunneling current density J is given by:

$$J = J_0(\phi - eV/2)e^{-A\sqrt{\phi - eV/2}} - J_0(\phi + eV/2)e^{-A\sqrt{\phi + eV/2}} \tag{3.1}$$

where $J_0 = e/2\pi h d^2$ and $A = (4\pi d/h)(2m^*)^{1/2}$. $\phi = (\phi_1 + \phi_2)/2$ is the average barrier height, d is the barrier thickness, and m^* is the effective mass of the barrier's conduction band. From Equation 3.1, it is evident that the tunneling current has a strong exponential dependence on the barrier height ϕ.

Simmons' formula includes contributions from tunneling across the entire trapezoidal barrier in an intermediate bias voltage range ($eV < \phi$). At low temperatures, one can distinguish between the DT and FN regimes by considering the relationship between current and bias voltage in the WKB approximation [98]. We end up with the following relations:

$$\ln \frac{I_{\mathrm{FN}}}{V^2} \propto -\frac{4d\sqrt{2m^*\phi^3}}{3\hbar e}\left(\frac{1}{V}\right) \tag{3.2a}$$

$$\ln \frac{I_{\mathrm{DT}}}{V^2} \propto \ln \frac{1}{V} - \frac{2d\sqrt{2m^*\phi}}{\hbar} \tag{3.2b}$$

Thus, a plot of $\ln\left(I/V^2\right)$ versus $1/V$ will result in a linear curve if Fowler-Nordheim tunneling dominates, whereas plotting $\ln\left(I/V^2\right)$ versus $\ln\left(1/V\right)$ will be linear in the direct tunneling regime.

Furthermore, temperature-dependent measurements reveal the onset of thermionic emission in which transport occurs via the insulating barrier's conduction band at sufficiently high temperatures. In this regime, the tunnel junction exhibits the relationship [99]:

$$\ln \frac{I(V)}{T^2} \propto -\frac{e\phi}{k_{\mathrm{B}}}\left(\frac{1}{T}\right) \tag{3.3}$$

Therefore, one can identify the thermionic emission regime by the linear region of a plot of $\ln\left(I/T^2\right)$ versus $1/T$.

The above discussion has assumed a nonmagnetic insulating barrier where the energy barrier is independent of spin. In a ferromagnet, however, magnetic exchange interactions split the band structure by an energy ΔE_{ex}. Without loss of generality, we can consider a ferromagnet with perpendicular anisotropy and magnetization in the $+z$ direction such that spin-up and spin-down electrons are parallel and antiparallel to the barrier's spins, respectively. This splitting introduces different barrier heights for spin-up ($\phi - \Delta E_{\mathrm{ex}}/2$) and spin-down ($\phi + \Delta E_{\mathrm{ex}}/2$) electrons tunneling across the barrier (Fig. 3-2b). Due to the exponential sensitivity of the tunneling probability on barrier height, a magnetic tunnel barrier effectively acts as a spin filter of electrons emitted from an unpolarized, nonmagnetic electrode.

Now, the total tunneling current density J is a sum of the components from both spin-up and spin-down electrons tunneling across the barrier ($J = J_\uparrow + J_\downarrow$), where:

$$J_\uparrow = J_0(\phi - \Delta E_{\text{ex}}/2 - eV/2)e^{-A\sqrt{\phi - \Delta E_{\text{ex}}/2 - eV/2}} \tag{3.4a}$$

$$-J_0(\phi - \Delta E_{\text{ex}}/2 + eV/2)e^{-A\sqrt{\phi - \Delta E_{\text{ex}}/2 + eV/2}}$$

$$J_\downarrow = J_0(\phi + \Delta E_{\text{ex}}/2 - eV/2)e^{-A\sqrt{\phi + \Delta E_{\text{ex}}/2 - eV/2}} \tag{3.4b}$$

$$-J_0(\phi + \Delta E_{\text{ex}}/2 + eV/2)e^{-A\sqrt{\phi + \Delta E_{\text{ex}}/2 + eV/2}}$$

The barrier is decreased for spin-up electrons and increased for spin-down electrons compared to the unpolarized paramagnetic state's barrier. Thus, $J_\uparrow$ dominates and this imbalance in tunneling current will result in a net spin-polarized current. The polarization can be calculated from the following formula:

$$P = \frac{J_\uparrow - J_\downarrow}{J_\uparrow + J_\downarrow} \tag{3.5}$$

Devices utilizing a magnetic insulating barrier, called spin-filter magnetic tunnel junctions, were first fabricated in the Moodera group at MIT in the late 1980s using EuS as the magnetic insulator and achieving P up to 80% [100]. Subsequent work using the antiferromagnet EuSe in the presence of an applied magnetic field led to an even larger P exceeding 97% [101].

In the early 2000s, theoretical proposals took these devices a step further by introducing the idea of a double spin-filter magnetic tunnel junction [102, 103]. In these devices, the tunnel barrier is comprised of two decoupled magnetic layers with different coercivities. As a result, one can use an applied magnetic field to selectively switch each of the magnetic barriers. When both of the layers' magnetizations $\vec{M}_{1,2}$ are aligned in the parallel state, electrons with spins aligned to the layers are preferentially tunneled across the entire junction — the junction behaves as a double spin filter with a large spin polarization (Fig. 3-3a). When $\vec{M}_{1,2}$ are antialigned in the antiparallel state, however, electrons that encounter a lower barrier for layer 1 then face a higher barrier for layer 2 and vice versa. This results in no net spin polarization and reduced electron transmission across the barrier (Fig. 3-3b).

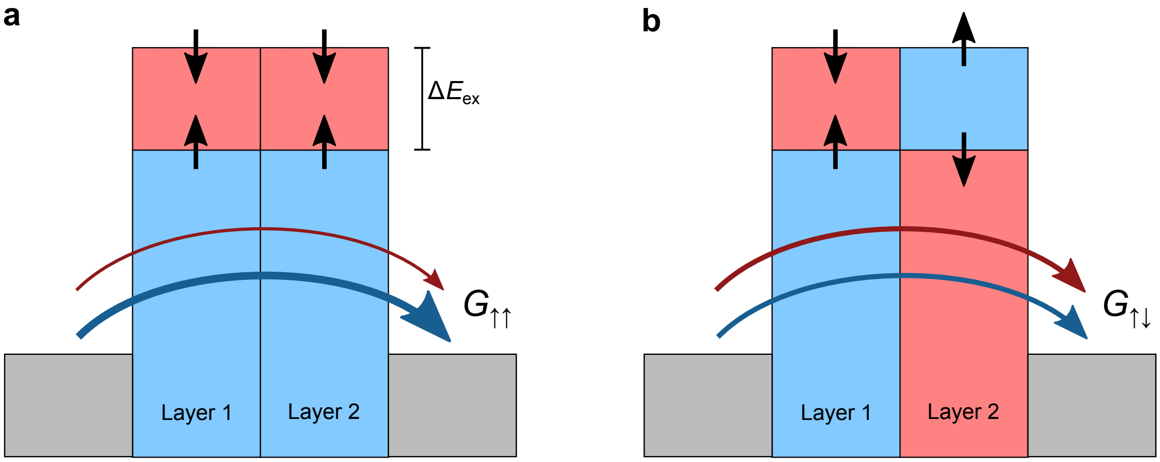

Figure 3-3: Schematic of a double spin-filter magnetic tunnel junction. **a.** In the parallel state, there is a large conductance $G_{\uparrow\uparrow}$ and a net spin polarization due to the reduced barrier for spin-up electrons aligned with both layers. **b.** In the antiparallel state, there is a small conductance $G_{\uparrow\downarrow}$ and no spin polarization of tunneling electrons.

In the simplified picture of two rectangular barriers with heights $\phi - \Delta E_{\mathrm{ex}}/2$ and $\phi + \Delta E_{\mathrm{ex}}/2$ for electrons with spins parallel (P) and antiparallel (AP) to the barrier, respectively, the transmission across each barrier in the free-electron approximation is given by [102]:

$$T_{P(AP)} = T_0 \exp\left[-2d\left(\frac{2m^*(\phi \mp \Delta E_{\mathrm{ex}}/2)}{\hbar^2}\right)^{1/2}\right] \tag{3.6}$$

The conductance across the barrier depends on the sum of transmissions for each spin channel:

$$G_{\uparrow\uparrow} = G_0(T_P T_P + T_{AP} T_{AP}) \tag{3.7a}$$

$$G_{\uparrow\downarrow} = G_0(T_P T_{AP} + T_{AP} T_P) \tag{3.7b}$$

where $G_{\uparrow\uparrow}$ and $G_{\uparrow\downarrow}$ correspond to the parallel and antiparallel $\vec{M}_{1,2}$ configurations, respectively. If we take the ratio of these two conductances and assume $(T_{AP})^2 \ll$

$(T_P)^2$, then:

$$\frac{G_{\uparrow\uparrow}}{G_{\uparrow\downarrow}} = \frac{(T_P)^2 + (T_{AP})^2}{2T_P T_{AP}} \approx \frac{(T_P)^2}{2T_P T_{AP}} = \frac{T_P}{2T_{AP}} \tag{3.8}$$

If we then define the wave vector $k_{P(AP)} = \left(\frac{2m^*(\phi \mp \Delta E_{\text{ex}}/2)}{\hbar^2}\right)^{1/2}$ from Eq. 3.6, we find that:

$$\frac{G_{\uparrow\uparrow}}{G_{\uparrow\downarrow}} = \frac{1}{2} e^{-2d(k_P - k_{AP})} \tag{3.9}$$

Thus, the magnetoresistance occurring when an applied magnetic field switches one of the layers is exponentially sensitive to the differences between parallel and antiparallel transmission of tunneling electrons. This simple model ignores many details of tunneling across an insulating barrier including complex-valued phases and resonant tunneling. Nevertheless, it demonstrates the potential for achieving a large, tunable magnetoresistance in a single tunnel junction device.

These proposed double spin filters were first experimentally realized by the Moodera group in 2009 using two EuS layers separated by an insulating spacer layer of 0.6 nm Al_2O_3 [104]. They achieved magnetoresistances up to 60%, defined as MR $= (G_{\uparrow\uparrow} - G_{\uparrow\downarrow})/G_{\uparrow\downarrow}$. Using different materials as the spin filters, there is the promise to achieve even larger magnetoresistances corresponding to P approaching unity.

3.3.1 Inelastic electron tunneling spectroscopy

So far, we have assumed that tunneling electrons are elastic, *i.e.* they do not gain or lose energy when tunneling across the barrier. This is a good approximation at zero bias, but once a small bias voltage is applied, another contribution must be considered. A tunneling electron can interact with the barrier either by losing a quantum of energy to excite a quasiparticle excitation in the barrier or by gaining a quantum of energy from an existing excitation. These quasiparticle excitations include phonons (collective lattice vibrations) [105] and magnons (collective spin waves) [106]. It should be noted that collective modes of the electrodes may also assist in electron tunneling [107]. All of these inelastic tunneling pathways contribute to the total conductance in addition to the elastic tunneling pathways previously discussed [108]. Therefore, by studying electron transmission as a function of bias voltage, one can perform inelastic electron tunneling spectroscopy (IETS) to probe the spectrum of the collective excitations in a material.

These additional tunneling channels become available once the bias energy eV exceeds the collective mode excitation energy $h\nu$. There are several experimental signatures once these tunneling pathways begin to contribute to the conductance, shown schematically in Fig. 3-4. Elastic processes alone yield an approximately linear relationship between I and V (Fig. 3-4a) [109]. If one measures dI/dV versus V using standard lock-in measurement techniques, the features will appear as steps as V is increased (Fig. 3-4b). By taking the derivative of those data, d^2I/dV^2 versus V then reveals peaks at the collective mode excitation energies (Fig. 3-4c).

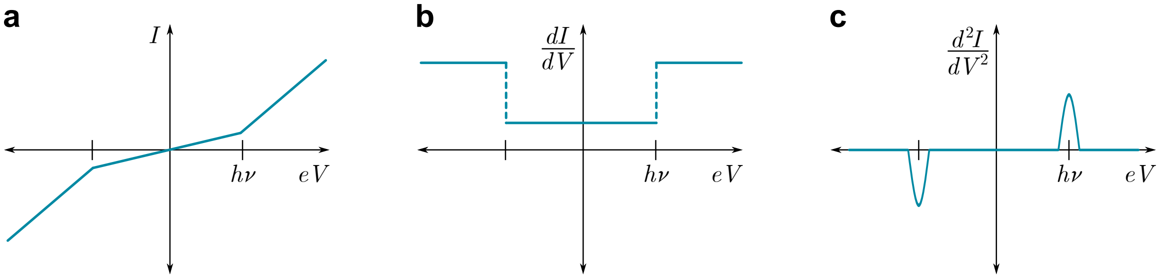

Figure 3-4: Experimental signatures of inelastic electron tunneling. These can be observed by plotting (**a**) I, (**b**) dI/dV, and (**c**)d^2I/dV^2 as a function of the bias energy eV. Figure adapted from Ref. [108].

The ability to detect inelastic features in a tunnel junction depends on several factors. First, the strength of interactions between tunneling electrons and the barrier (*e.g.* electron-phonon or electron-magnon coupling) influence the signal strength [106]. Second, the width of the peak has contributions from three main sources that add in quadrature: the natural intrinsic linewidth W_{int} of the mode, thermal broadening W_{therm}, and broadening from the finite modulation W_{mod} of the lock-in measurement setup [108]. The full width at half maximum (FWHM) of W_{therm} is $5.4k_{\text{B}}T$ [109], corresponding to FWHM of 2 meV at 4.2 K or 0.14 meV at 300 mK. Therefore, cryogenic temperatures are required to resolve the low-energy excitations of many materials. Moreover, the FWHM broadening from the AC voltage applied by the lock-in amplifier W_{mod} is $1.2V_{\text{AC}}$ [109]. Therefore, to minimize W_{mod}, one should apply a very small V_{AC}.

3.3.2 Tunneling through 2D magnetic insulators

Since the chromium trihalides are insulating magnets, a natural way to probe them is through spin-filter magnetic tunnel junctions with CrX_3 serving as the tunnel barrier. The van der Waals gap (0.35 nm in CrI_3) acts as a natural spacer layer to decouple the individual magnetic layers in the crystal. Thus, unlike for the $EuS/Al_2O_3/EuS$ barriers described in the previous section, we do not need to introduce an additional layer to separate the magnetic layers. We can therefore consider bilayer CrX_3 as an *intrinsic* double spin filter with only weak magnetic coupling across the gap compared to the strong intralayer exchange interactions.

Over the past several years, numerous studies have been published on van der Waals magnetic tunnel junctions fabricated from CrI_3 [110–115], $CrBr_3$ [114–116], and $CrCl_3$ [13, 114, 115, 117, 118]. Chapters 6 and 7 detail our studies on CrI_3 and $CrCl_3$ magnetic tunnel junctions, respectively. In all of these works, junctions are fabricated using dry-transfer van der Waals assembly to sandwich a thin CrX_3 crystal between two narrow strips of few-layer graphene, which are then contacted to metal electrodes (*e.g.* Au, Pd). The stack is aligned such that the only way for electrons to travel from one graphene flake to the other is to tunnel vertically through the CrX_3 barrier. In most cases, hexagonal boron nitride is used to fully encapsulate the junction and protect the CrX_3 flake from ambient conditions when loading the device into the cryostat.

These junctions reveal valuable information to help us better understand these materials in the ultrathin limit. For example, we can extract the magnetic interlayer exchange coupling between the layers in the antiferromagnet $CrCl_3$ by studying how they align to an applied magnetic field [13]. We can also study the magnetic ordering as a function of both in-plane and out-of-plane applied magnetic field and use it to probe in-plane magnetism (as in $CrCl_3$). This can be difficult to achieve through optical setups that rely on normal incidence (*e.g.* polar MOKE or polar helical-PL) and can only probe the out-of-plane magnetic signals. Moreover, we can learn about the CrX_3 magnon spectra through inelastic electron tunneling spectroscopy in these junctions [110, 115, 116].

These devices are also emerging as a new platform for van der Waals spintronics. They can have extremely large magnetoresistances up to $10^6\%$ when using a thick CrI_3 barrier from a multiple spin filter effect [112]. These MR values correspond to large spin polarization in the fully-aligned ferromagnetic state, which could be utilized by the spintronics community. Furthermore, magnetization switching of bilayer CrI_3 has been demonstrated using both electrical generation and detection in a single device [119]. While materials suitable for applications would ideally be air-stable and magnetic at room temperature, these initial experiments on CrX_3 serve as a proof of concept to demonstrate the potential for incorporating van der Waals magnets into spintronics devices.

3.4 Other probes of 2D magnetism

This thesis focuses on magneto-optical and tunneling measurements of 2D magnets. Beyond these two categories, there are other powerful techniques to study these materials. Several of these methods are described in the following section.

A nitrogen-vacancy (NV) center is a defect in the diamond crystal lattice that hosts a spin-1/2 magnetic moment. This isolated single spin has garnered attention from the quantum computing community as a new qubit platform, but has also found use as a highly sensitive magnetometer for condensed matter systems [120] including van der Waals materials [121]. It acts as a nonperturbative probe of stray magnetic fields, from which the magnetic texture can be reconstructed. It can also be used to detect spin waves (magnons) in a magnetic system, as was demonstrated in a 20 nm thick film of yttrium iron garnet (YIG) [122].

By implanting a single NV center on a diamond scanning probe tip, one can scan across a flat sample to spatially detect the stray fields coming from 2D material. Using this scanning NV technique, researchers have successfully imaged magnetic order and domains in few-layer CrI_3 [123]. While this technique applied to 2D magnets is in its infancy, it is a promising approach to nondestructively measure magnetic signals with greater spatial resolution (60-100 nm) than MOKE and other optical techniques that employ a laser of visible light (1-2 µm spot size).

Another method to sense magnetization is the anomalous Hall effect (AHE). In a nonmagnetic Hall bar device, the Hall effect yields a transverse resistance $R_{xy} = A\mu_0 H_z$, where $\mu_0 H_z$ is the applied out-of-plane magnetic field and A is a constant. However, in a sample with perpendicular magnetization M_z, the AHE manifests in a second term, giving an overall Hall resistance $R_{xy} = A\mu_0 H_z + BM_z$. This measurement has been used to demonstrate perpendicular magnetic order in the conducting ferromagnet Fe_3GeTe_2 down to the monolayer limit [9]. In a similar way, Hall micromagnetometry of insulating ferromagnets placed on top of a graphene Hall bar can also give quantitative information about their magnetization as a function of applied magnetic field [124].

Finally, there are numerous other techniques that have been previously used for thin-film magnets and could be extended to study van der Waals magnets in the coming years. These include spin-polarized scanning tunneling microscopy (SP-STM) [125], magnetic force microscopy (MFM) [126], and Brillouin light scattering (BLS) [127, 128].

Chapter 4

Layer-dependent ferromagnetism in a van der Waals crystal down to the monolayer limit

The following chapter is based on work published in *Nature* (Ref. [7]), and appears here with modifications, corrections, and expanded discussions.

4.1 Introduction

Since the discovery of graphene [1], the family of two-dimensional materials has grown, displaying a broad range of electronic properties. Recent additions include semiconductors with spin-valley coupling [129], Ising superconductors [6, 130, 131] that can be tuned into a quantum metal [132], possible Mott insulators with tunable charge-density waves [133], and topological semimetals with edge transport [12, 63, 134]. However, no two-dimensional crystal with intrinsic magnetism has yet been discovered [41, 86, 135–137]; such a crystal would be useful in many technologies from sensing to data storage [138]. Theoretically, magnetic order is prohibited in the two-dimensional isotropic Heisenberg model at finite temperatures by the Mermin-Wagner theorem [40]. Magnetic anisotropy removes this restriction, however, and enables, for instance, the occurrence of two-dimensional Ising ferromagnetism. Here we use magneto-optical Kerr effect microscopy to demonstrate that monolayer chromium triiodide (CrI_3) is an Ising ferromagnet with out-of-plane spin orientation. Its Curie temperature of 45 Kelvin is only slightly lower than that of the bulk crystal, 61 Kelvin, which is consistent with a weak interlayer coupling. Moreover, our studies suggest a layer-dependent magnetic phase, highlighting thickness-dependent physical properties typical of van der Waals crystals [4, 139, 140]. Remarkably, bilayer CrI_3 displays an antiferromagnetic ground state with a metamagnetic transition to ferromagnetic order [141]. This work creates opportunities for studying magnetism by harnessing the unusual features of atomically thin materials, such as electrical control for realizing magnetoelectronics [86], and van der Waals engineering to produce interface phenomena [138].

Magnetic anisotropy is an important requirement for realizing two-dimensional (2D) magnetism. In ultrathin metallic films, whether an easy axis can originate from symmetry reduction at the interface or surface is dependent on substrate properties and interface quality [142–144]. In contrast, most van der Waals magnets have an intrinsic magnetocrystalline anisotropy owing to the reduced crystal symmetry of their layered structures. Several layered magnets exhibit effective 2D magnetic interactions even in their bulk crystal form [145, 146]. This implies that it might be possible to retain a magnetic ground state in a monolayer. In addition to enabling the study of magnetism in naturally formed crystals in the true 2D limit, layered magnets provide a platform for studying the thickness dependence of magnetism in isolated single crystals where the interaction with the underlying substrate is weak. These covalently bonded van der Waals layers prevent complex magnetization reorientations induced by epitaxial lattice reconstruction and strain [144]. For layered materials, these advantages come at a low fabrication cost, since the micromechanical exfoliation technique is much simpler than conventional approaches requiring sputtering or sophisticated molecular beam epitaxy.

A variety of layered magnetic compounds have recently been investigated to determine whether their magnetic properties can be retained down to monolayer thickness [86, 136, 137, 147]. Recent Raman studies suggest ferromagnetic ordering in few-layer $Cr_2Ge_2Te_6$ and antiferromagnetic ordering in monolayer $FePS_3$ [148, 149]. However, no evidence yet exists for ferromagnetism persisting down to the monolayer limit. One promising candidate is bulk crystalline CrI_3. It shows layered Ising ferromagnetism below a Curie temperature (T_C) of 61 K with an out-of-plane easy axis ((Figs. 4-1a and b, Fig. 3-1)) [41,42]. Given its van der Waals nature, we expect magnetocrystalline anisotropy, which could possibly lift the Mermin–Wagner restriction to stabilize long-range ferromagnetic ordering even in a monolayer.

4.2 Characterization of bulk and thin CrI_3 crystals

In our experiment, we obtained atomically thin CrI_3 flakes by mechanical exfoliation of bulk crystals onto oxidized silicon substrates (see Section 4.7.1 for CrI_3 crystal growth details). Given the reactivity of CrI_3 flakes, sample preparation was carried out in a glovebox under an inert atmosphere. We mainly employed optical contrast based on the pixel red–green–blue (RGB) value to index the number of layers in a flake (see Section 4.7.3 for quantitative optical microscopy in CrI_3). Figure 4-1c is an optical micrograph of a typical multi-step CrI_3 flake on a 285 nm SiO_2/Si substrate, showing regions ranging from 1 to 6 layers in thickness. Figure 4-1d shows an optical contrast map of the same region illuminated by 631 nm filtered light. The extracted optical contrast as a function of layer thickness is in good agreement with models based on the Fresnel equations (Fig. 4-1e). To accurately determine the correspondence between optical contrast and flake thickness, we also measured the thickness of CrI_3 flakes by atomic force microscopy, determined to be 0.7 nm per layer, after encapsulation with few-layer graphene (see Figure 4-9).

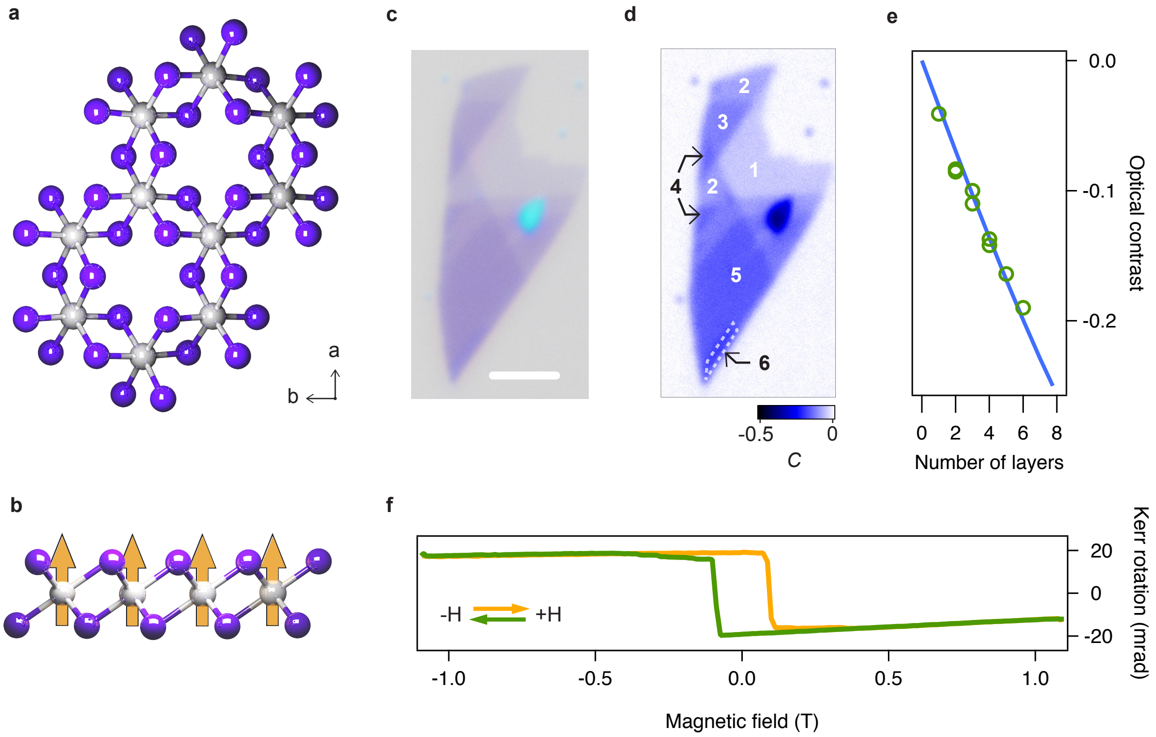

Figure 4-1: Crystal structure, layer thickness identification, and MOKE of bulk CrI_3. **a.** View of the in-plane atomic lattice of a single CrI_3 layer. Grey and purple balls represent Cr and I atoms, respectively. The Cr^{3+} ions are coordinated to six I^- ions to form edge-sharing octahedra arranged in a hexagonal honeycomb lattice. **b.** Out-of-plane view of the same CrI_3 structure depicting the Ising spin orientation. **c.** Optical micrograph of a representative CrI_3 flake. **d.** Calculated optical contrast map of the same flake with a 631 nm optical filter. The scale bar in **c** is 3 μm. **e.** Averaged optical contrast of the steps of the sample with different numbers of layers (circles) fitted by a model based on the Fresnel equations (solid line). **f.** Polar MOKE signal of a thin bulk CrI_3 crystal.

4.3 MOKE measurements of ferromagnetic order in monolayer CrI_3

To probe the magnetic order, we employed polar magneto-optical Kerr effect (MOKE) measurements as a function of applied external magnetic field perpendicular to the sample plane (Faraday geometry). This design is sensitive to out-of-plane magnetization, and can detect small Kerr rotations, θ_K, of linearly polarized light down to 100 μrad using an alternating-current polarization modulation technique as laid out in Fig. 4-4. All optical measurements were carried out using a 633 nm HeNe laser and at a temperature of 15 K, unless otherwise specified. Figure 1f illustrates the MOKE signal from a thin bulk flake of CrI_3. The observed hysteresis curve and remanent θ_K at zero magnetic field $\mu_0 H = 0$ T (where μ_0 is the magnetic constant) are hallmarks of ferromagnetic ordering, consistent with its bulk ferromagnetism with out-of-plane magnetization. The negative remanent θ_K when approaching zero field from a positive external field is a consequence of thin-film interference from reflections at the CrI_3–SiO_2 and SiO_2–Si interfaces (see Section 4.7.4 for thin-film interference and Fig. 4-8).

Remarkably, the ferromagnetic ordering remains in the monolayer limit. Figure 4-2a shows θ_K as a function of $\mu_0 H$ for a monolayer CrI_3 flake (inset to Fig. 4-2a). A single hysteresis loop in θ_K centred around $\mu_0 H = 0$ T, with a non-zero remanent Kerr rotation, demonstrates out-of-plane spin polarization. This implies Ising ferromagnetism in monolayer CrI_3. As expected, θ_K is independent of the excitation power (Fig. 4-2b). In the following, all data are taken with an excitation power of 10 µW. We have measured a total of 12 monolayer samples, which show similar MOKE behavior with consistent remanent θ_K values of about 5 ± 2 mrad at $\mu_0 H = 0$ T. The coercive field ($\mu_0 H_c$), which is approximately 50 mT for the sample in Fig. 4-2a, can vary between samples owing to the formation of domain structures in some samples.

Figure 4-2c shows spatial maps of θ_K for another monolayer, taken at selected magnetic field values. After cooling the sample from above T_C at $\mu_0 H = 0$ T, the entire monolayer is spontaneously magnetized (in blue, defined as spin down). As the field is increased to 0.15 T, the magnetization in the upper half of the flake switches direction (now spin up, in red). As the field is further increased to 0.3 T, the lower half of the monolayer flips and the entire flake becomes spin up, parallel to $\mu_0 H$. This observation of micrometer-scale lateral domains suggests different values of coercivity in each domain. Indeed, magnetic field sweeps (θ_K versus $\mu_0 H$) taken at discrete points ranging across both domains (Fig. 4-2d) show the difference in coercive field between the upper and lower half of the monolayer. Sweeps taken only on the upper domain (marked by a blue circle) show a much narrower hysteresis loop (about 50 mT) than sweeps from spots on the lower domain (orange and purple circles, about

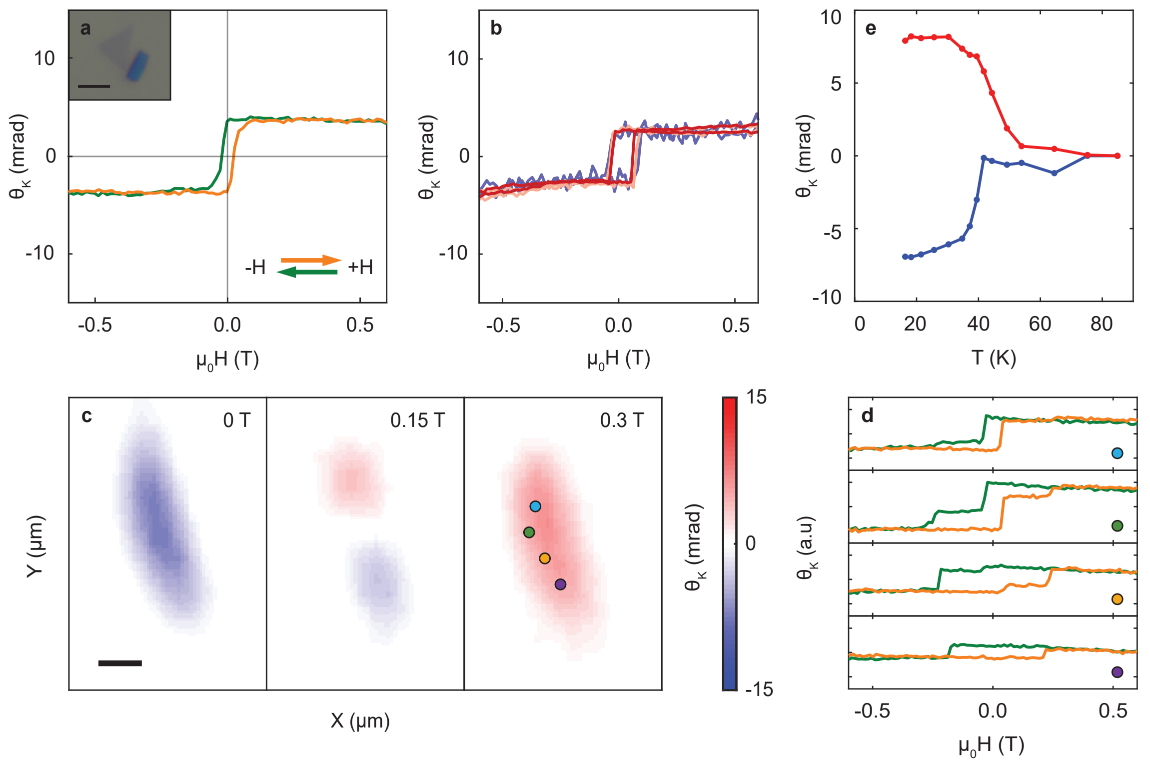

Figure 4-2: MOKE measurements of monolayer CrI_3. **a.** Polar MOKE signal for a CrI_3 monolayer. The inset shows an optical image of an isolated monolayer (the scale bar is 2 μm). **b.** Power dependence of the MOKE signal taken at incident powers of 3 μW (blue), 10 μW (pink), and 30 μW (red). **c.** MOKE maps at $\mu_0 H = 0$ T, 0.15 T, and 0.3 T on a different monolayer. The scale bar is 1 μm. **d.** θ_K versus $\mu_0 H$ sweeps taken at four points marked by dots on the $\mu_0 H = 0.3$ T map in **c**. **e.** Temperature dependence of MOKE signal with the sample initially cooled at $\mu_0 H = 0$ T (blue) and 0.15 T (red).

200 mT). When the beam spot is centred between the two domains, contributions from both can be seen in the resulting hysteresis loop (green circle), a consequence of the approximately 1 μm beam spot illuminating both domains.

To determine the monolayer T_C, we perform an analysis of the irreversible field-cooled (FC) and zero-field-cooled (ZFC) Kerr signal. ZFC sweeps were performed by measuring θ_K while cooling the sample in zero field. After warming up to a temperature well above T_C (90 K), the FC measurement is taken upon cooling down in the presence of a small external magnetic field ($\mu_0 H = 0.15$ T). Thermomagnetic irreversibility can be observed below T_C, at which point the ZFC sweep and the FC sweep diverge as illustrated in Fig. 4-2e. We measured the average T_C for the monolayer samples to be 45 K, slightly lower than the value (61 K) for bulk samples.

4.4 Layer-dependent magnetism in few-layer CrI_3 crystals

The layered structure of CrI_3 provides a unique opportunity to investigate ferromagnetism as a function of layer thickness. Figure 4-3a–c shows θ_K versus $\mu_0 H$ for representative one- to three-layer CrI_3 samples. All measured monolayer and trilayer samples consistently show ferromagnetic behavior with a single hysteresis loop centred at $\mu_0 H = 0$ T (Fig. 4-3a and c). Both remanent and saturation values of θ_K for trilayers are about 50±10 mrad, which is an order of magnitude larger than for monolayers. This drastic change in θ_K on moving from monolayer to trilayer may be due to a layer-dependent electronic structure, leading to weaker optical resonance effects at 633 nm for the monolayer than for the trilayer (see Section 4.7.4 for modeling the thin-film interference and MOKE signal in CrI_3). We find that for trilayers and thin bulk samples, T_C is consistent with the bulk value of 61 K. The relatively small decrease of T_C from bulk to few-layer and monolayer samples suggests that interlayer interactions do not dominate the ferromagnetic ordering in CrI_3. Compared with metallic magnetic thin films whose magnetic properties strongly depend on the underlying substrate [150], the weak layer-dependent T_C also implies a negligible substrate effect on the ferromagnetic phenomena in atomically thin CrI_3. As such, exfoliated CrI_3 of all thicknesses can be regarded as isolated single crystals.

A further observation is that bilayer CrI_3 shows a markedly different magnetic behavior from the monolayer (Fig. 4-3b). For all ten bilayer samples measured, the MOKE signal is strongly suppressed, with θ_K approaching zero (subject to slight variation between samples) at field values ±0.65 T. This observation implies a compensation for the out-of-plane magnetization. Upon crossing a critical field, θ_K shows a sharp jump, depicting a sudden recovery of the out-of-plane co-parallel orientation of the spins. This new magnetic state has a saturation θ_K (40±10 mrad) an order

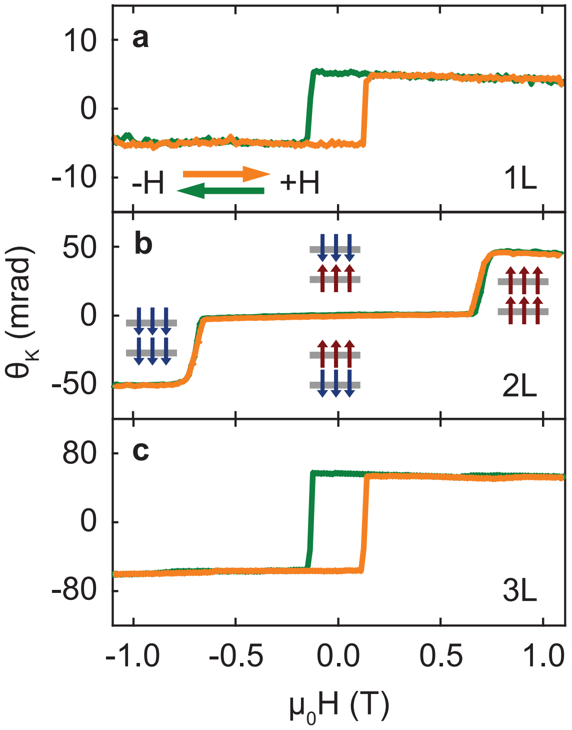

Figure 4-3: Layer-dependent magnetic ordering in atomically-thin CrI_3. **a.** MOKE signal on a monolayer (1L) CrI_3 flake, showing hysteresis in the Kerr rotation as a function of applied magnetic field, indicative of ferromagnetic behavior. **b.** MOKE signal from a bilayer CrI_3 showing vanishing Kerr rotation for applied fields ±0.65 T, suggesting antiferromagnetic behavior. Insets depict bilayer (2L) magnetic ground states for different applied fields. **c.** MOKE signal on a trilayer (3L) flake, showing a return to ferromagnetic behavior.

of magnitude larger than that of monolayer samples, and slightly smaller than for trilayers.

The suppression of the Kerr signal at zero magnetic field demonstrates that the ground state has zero out-of-plane magnetization. The plateau behavior of the magnetization curve—showing three horizontal regimes between magnetic field values of -1.1 T and 1.1 T (Fig. 4-3b)—further implies that there are no in-plane spin components; otherwise, one would expect a gradual increase of the MOKE signal with increasing perpendicular magnetic field. Rather, our observation suggests that each individual layer is ferromagnetically ordered (out-of-plane) while the interlayer coupling is antiferromagnetic. In this case, the strength of the interlayer coupling determines the field at which jumps between different plateaus occur, ±0.65 T. Although the detailed mechanism of this coupling remains unclear, the different magnetic phases observed in bilayers and trilayers emphasizes the strong layer-dependent interplay between different mechanisms that stabilize magnetic ordering in the atomically thin limit.

Another bilayer feature distinct from those of monolayers is the vanishingly small hysteresis around the jumps, suggesting negligible net perpendicular anisotropy. A possible interpretation is that the shape anisotropy (which prefers in-plane spin orientation) nearly compensates for the intrinsic magnetocrystalline anisotropy (which prefers out-of-plane spin orientation) so that the overall anisotropy is close to zero.

The insets in Fig. 4-3b display the layer-by-layer switching behavior that leads to plausible magnetic ground states of bilayer CrI_3. When the magnetic field is ± 0.65 T, the magnetization of the two layers are oppositely oriented to one another. Thus, the net magnetization vanishes and bilayer CrI_3 behaves as an antiferromagnet with an exchange field of about 0.65 T. When $|\mu_0 H| > 0.65$T, magnetization in one layer flips to align with the external magnetic field and restores out-of-plane magnetization, giving rise to the large MOKE signal. At around $|\mu_0 H| = 0.65$ T, the MOKE signal sharply increases from near zero to its saturation value within about 100 mT, suggesting an abrupt increase of out-of-plane magnetization triggered by a small change of magnetic field. Such behavior is indicative of metamagnetism, the magnetic-field-driven transition from antiferromagnetic ordering to a fully spin-polarized state [141].

4.5 Conclusion

In summary, here we demonstrated 2D ferromagnetism in exfoliated monolayer CrI_3. The observed monolayer T_C suggests that these 2D magnets are weakly coupled to their substrates and can be regarded as isolated magnets. This is in distinct contrast with conventional metallic monolayer films, whose magnetism is strongly affected by substrate coupling. We also observed strong evidence for layer-dependent magnetic phases, from ferromagnetism in the monolayer, to antiferromagnetism in the bilayer, and back to ferromagnetism in the trilayer and bulk. We envision that the demonstration of intrinsic ferromagnetism in monolayer CrI_3 as well as its layer-dependent magnetic behavior will provide opportunities for the investigation of quantum phenomena, such as topological effects in hybrid superconducting–ferromagnetic van der Waals heterostructures as well as the engineering of new magneto-optoelectronic devices at low temperature, such as ferromagnetic light emitters.

4.6 Epilogue

These initial experiments were instrumental in proving the existence of long-range ferromagnetic order in a monolayer van der Waals crystal. At the time, however, we were limited in the range of our applied magnetic field. As a result, we only could see one spin-flip transition in our trilayer crystals (Fig. 4-3c). Subsequent optical measurements using an expanded magnetic field range demonstrate a second spin-flip transition near 1.6 T [111]. This additional information corroborates the layered antiferromagnetism picture of ultrathin CrI_3, where the trilayer ground state (either $\uparrow\downarrow\uparrow$ or $\downarrow\uparrow\downarrow$) first undergoes a switch to an intermediate state (either $\uparrow\uparrow\downarrow$ or $\downarrow\uparrow\uparrow$) in the presence of an external field in the $+z$ direction before fully aligning to the external field at 1.6 T ($\uparrow\uparrow\uparrow$).

4.7 Supplemental Information

4.7.1 Growth of CrI_3 bulk crystals

Chromium powder (99.5%, Sigma-Aldrich) and anhydrous iodine beads (99.999%, Sigma-Aldrich) were mixed in a 1:3 ratio inside a glovebox with an argon atmosphere. 1.5 g of the mixture was then loaded in a silica ampule (inner diameter of 16 mm, outer diameter of 19 mm, and length of 550 mm). The ampule was extracted from the glovebox and immediately evacuated to a pressure of approximately 10^{-4} Torr. Once at that pressure, the closed end was dipped in liquid nitrogen to prevent the sublimation of the iodine beads. The ampule was then flame-sealed under dynamic vacuum and placed inside a three-zone furnace. A three-zone furnace provides the best control over the growth process by reducing nucleation, leading to the growth of large-size single isolated crystals. Following an inverted gradient step of several hours, the crystals were grown over a period of 7 days with source zone at 650°C (containing the solid mixture), middle growth zone at 550°C and third zone at 600°C. Crystals formed both in the source (shiny hexagonal platelets of several millimeters in size) and the middle (millimeter-long ribbon-like flakes) zones. The crystals were extracted from the ampule in an argon atmosphere and stored in anhydrous conditions.

The I:Cr elemental ratio was verified to be 2.8±0.2 in several crystals by energy-dispersive X-ray microanalysis performed on individual crystals in a Zeiss Merlin high-resolution scanning electron microscope equipped with an electron dispersive spectroscopy probe. To confirm the crystallographic phase of the material, a few single crystals were ground into a powder, loaded into a 0.3-mm outer-diameter capillary, and mounted on a Rigaku Smartlab Multipurpose Diffractometer setup in converging beam configuration with a D/teX detector. The room-temperature X-ray diffraction patterns of both the ribbon-like and hexagonal platelets were identical and consistent with the high-temperature monoclinic $AlCl_3$-type structure ($C2/m$) reported for CrI_3, with indexed unit cell parameters of a = 6.8735(2) Å, b = 11.8859(3) Å, c = 6.9944(1) Å, and $\beta = 108.535(2)°$ (Le-Bail refinement, $R_{\mathrm{Bragg}} = 5.27\%$). SQUID magnetometry performed on the single crystals depicts a T_{C} of 61 K and a saturation magnetization of $3\mu_{\mathrm{B}}$ per Cr atom, also in agreement with the values reported in the literature [41].

A more detailed discussion on the growth of bulk chromium trihalide crystals can be found in Appendix A.

4.7.2 MOKE setup

Power-stabilized light from a 633 nm HeNe laser source was linearly polarized at 45° to the photoelastic modulator (PEM) slow axis (Fig. 4-4) [91]. Transmitting through the PEM, the light was sinusoidally phase-modulated at 50.1 kHz, with a maximum retardance of $\lambda/4$. Upon phase modulation, the light was focused down onto the sample at normal incidence using an aspheric lens. At any point in time when the light was not circularly polarized, reflection off a magnetic sample would rotate the polarization axis (the major axis for elliptically polarized light) by what we define as the Kerr rotation, θ_K. This reflection was then separated from the incidence path via a laser line non-polarizing beamsplitter cube and projected onto the PEM slow axis using a second polarizer. For $\theta_K = 0$, the slow-axis component remains constant for all polarizations and hence is not time-dependent. With a non-zero θ_K, however, the slow-axis component depends on the polarization and oscillates at twice the modulation frequency, 100.2 kHz, with an amplitude that is proportional to the Kerr rotation. Therefore, to obtain θ_K, the reflection was detected using an amplified photodiode and two lock-in amplifiers: one tuned at 100.2 kHz to detect the Kerr rotation, and one tuned at the chopper frequency, 800 Hz, to normalize the Kerr signal to laser intensity fluctuations and the reflectivity of the sample.

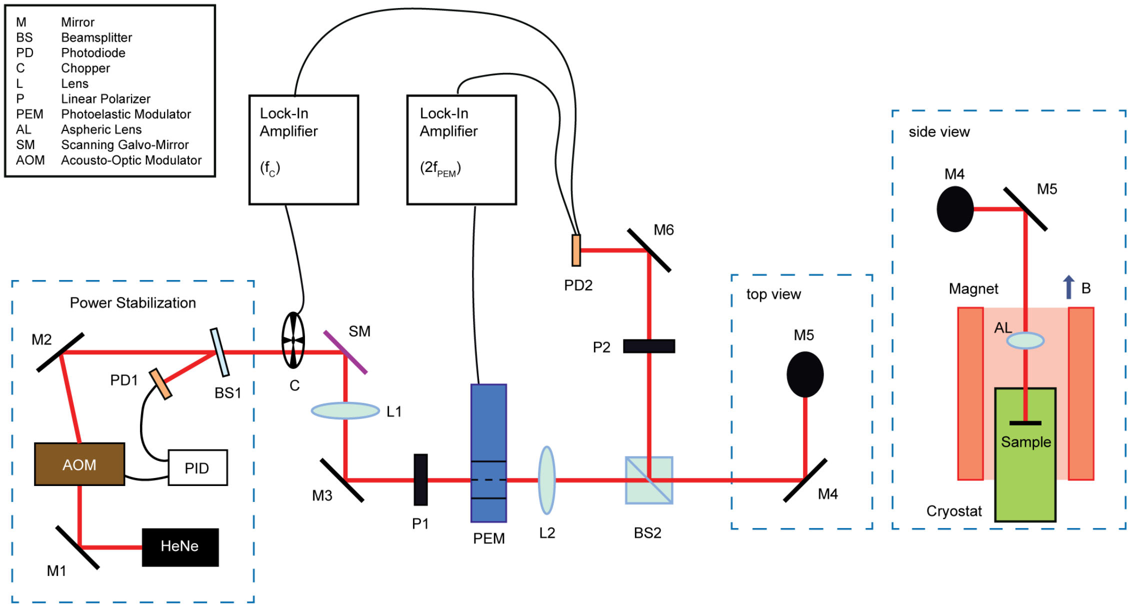

Figure 4-4: Magneto-optical Kerr effect experimental setup. Schematic of the optical setup used to measure the MOKE effect in CrI_3 samples. 633 nm optical excitation is provided by a power-stabilized HeNe laser. A mechanical chopper and photoelastic modulator provide intensity and polarization modulation, respectively. The modulated beam is directed through a polarizing beam splitter to the sample, housed in a closed-cycle cryostat at 15 K. A magnetic field is applied at the sample using a 7 T solenoidal superconducting magnet in Faraday geometry. The reflected beam passes through an analyser onto a photodiode, where lock-in detection measures the reflected intensity (at f_C) as well as the Kerr rotation (at f_{PEM}).

4.7.3 Quantitative optical microscopy in CrI_3

Optical microscopy images were taken using a Nikon Eclipse LV-CH 150NA optical microscope with a DS-Ri2 full-frame camera. The setup was located inside a glovebox (argon atmosphere) to prevent sample degradation. The quantitative optical contrast analysis required that images were captured with a 100× objective under monochromatic illumination at normal incidence. In practice, 10 nm full-width at half-maximum (FWHM) filters were used (Andover Corp.) to filter the light coming from a halogen lamp. The thickness of the flakes was determined by contact-mode AFM under ambient conditions. Given the extreme sensitivity of the samples to atmospheric moisture, the CrI_3 flakes were encapsulated between two pieces of few-layer graphite (typically 5 nm in thickness) before being extracted from the glovebox. For each optical-microscopy-filtered image, individual RGB values were extracted and averaged over each flake and substrate region to give the reflected intensities of the flake and substrate. The intensity was chosen to be exclusively the value of the channel with the highest number of counts. The experimental optical contrast value was then calculated according to the following expression:

$$C(d, \lambda) = \frac{I_{flake} - I_{substrate}}{I_{flake} + I_{substrate}} \tag{4.1}$$

Equation (4.1) expresses the relationship between the optical contrast C between each flake and the substrate using the reflected intensities from the flake (I_{flake}) and the substrate ($I_{\text{substrate}}$). Fig. 4-5 shows an example of a contrast map of a multi-step CrI_3 flake extracted from its optical micrograph.

For flakes that have been exfoliated on a SiO_2/Si substrate, C depends on the thickness of the flake and on the illumination wavelength [151, 152]. Following the quantitative microscopy analysis proposed for graphene on SiO_2/Si substrates [30], C can be computed for any kind of flake by using a model based on the Fresnel equations

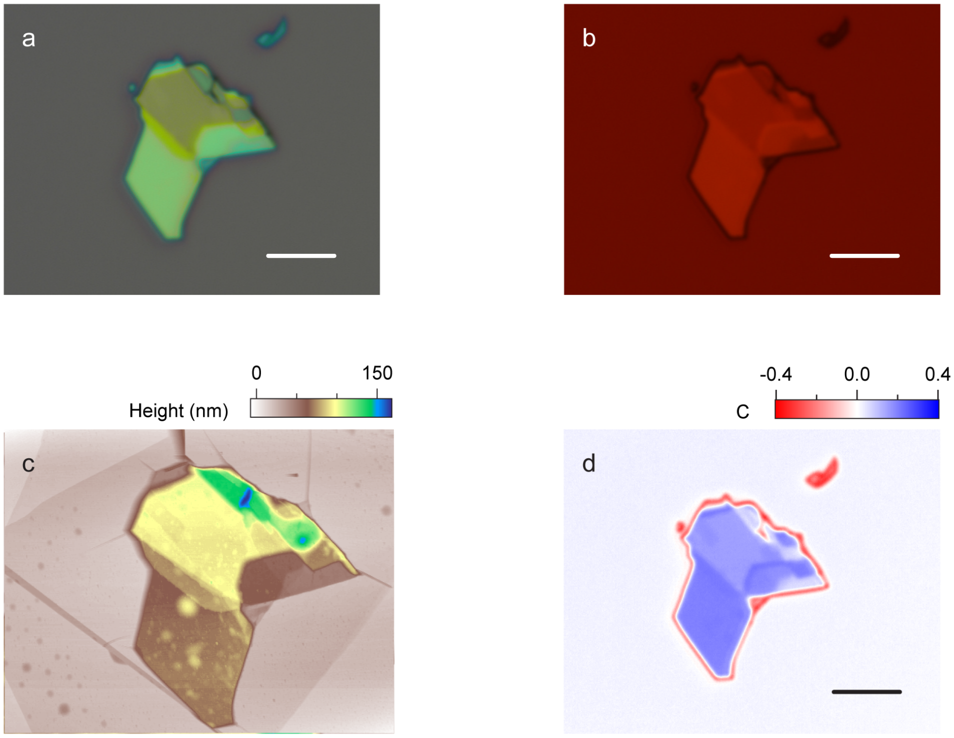

Figure 4-5: Thickness dependence of the optical contrast of the CrI_3 flakes. **a.** Optical micrograph of a CrI_3 sample illuminated with white light. **b.** Optical micrograph using a 631 nm (10 nm FWHM bandpass) filter. **c.** AFM topography image of the same sample. µd. Optical contrast map extracted from the 631 nm micrograph in **b**. Scale bars are 5 µm.

shown in equations (4.2a) and (4.2b):

$$I_{substrate}(\lambda) = \left| \frac{r_{02} + r_{23}e^{-2i\Phi_2}}{1 + r_{02}r_{23}e^{-2i\Phi_2}} \right|^2 \tag{4.2a}$$

$$I_{flake}(\lambda) = \left| \frac{r_{02}e^{i(\Phi_1+\Phi_2)} + r_{12}e^{-i(\Phi_1-\Phi_2)} + r_{23}e^{-i(\Phi_1+\Phi_2)} + r_{01}r_{12}r_{23}e^{i(\Phi_1-\Phi_2)}}{e^{i(\Phi_1+\Phi_2)} + r_{01}r_{12}e^{-i(\Phi_1-\Phi_2)} + r_{01}r_{23}e^{-i(\Phi_1+\Phi_2)} + r_{12}r_{23}e^{i(\Phi_1-\Phi_2)}} \right|^2 \tag{4.2b}$$

In this calculation, the subscripts 0, 1, 2 and 3 refer to air (treated as vacuum), CrI_3, SiO_2, and Si, respectively. The amplitude of the reflected path at the interface between media j and k is given by r_{jk} in equation (4.3b) and is calculated from the complex refractive indices defined in equation (4.3a). Φ_j is the phase shift introduced by the interaction between light of wavelength λ and medium j with thickness d_j

shown in equation (4.3c).

$$\tilde{n}_j(\lambda) = n_j - i\kappa_j \tag{4.3a}$$

$$r_{jk} = \frac{\tilde{n}_j - \tilde{n}_k}{\tilde{n}_j + \tilde{n}_k} \tag{4.3b}$$

$$\Phi_j = \frac{2\pi \tilde{n}_j d_j}{\lambda} \tag{4.3c}$$

As can be noted from the previous expressions, if one wants to model C using the Fresnel equations, the complex index of refraction of the material under study must be known. The reflectivity of CrI_3 measured in vacuum at 300 K at normal incidence of a single-crystal platelet of CrI_3 has been previously reported [153]. These data were used to calculate the phase of the amplitude reflection coefficient θ at energies in the visible range by numerical integration, according to the Kramers–Kronig relation (4.4a). The refractive index n and extinction coefficient κ of CrI_3 were then obtained throughout the visible range by combining equations (4.4b) and (4.4c) at each energy value. The results are plotted in Fig. 4-6.

$$\theta(E) = -\frac{E}{\pi}\int_0^\infty \frac{\ln\left[R(E')\right]}{(E')^2 - E^2} \tag{4.4a}$$

$$r(E) = \sqrt{R(E)}e^{i\theta(E)} \tag{4.4b}$$

$$r(E) = \frac{n(E) - 1 + i\kappa(E)}{n(E) + 1 + i\kappa(E)} \tag{4.4c}$$

Substituting for the complex indices of refraction [154] of CrI_3, Si, and SiO_2 in equations (4.2a) and (4.2b), we can calculate the expected value of C for flakes of different thicknesses as a function of the illumination wavelength. Fig. 4-7a shows the contrast map for CrI_3 considering a fixed thickness of 285 nm of the SiO_2 layer in the SiO_2/Si substrate. We also present a line cut of that plot at an illumination wavelength of 635 nm in Fig. 4-7b. It can be seen that the experimental data points closely follow the trend predicted by the model. Given that the method is non-destructive and can be performed inside a glovebox for many different illumination wavelengths, the error in the determination of the number of layers can be reduced.

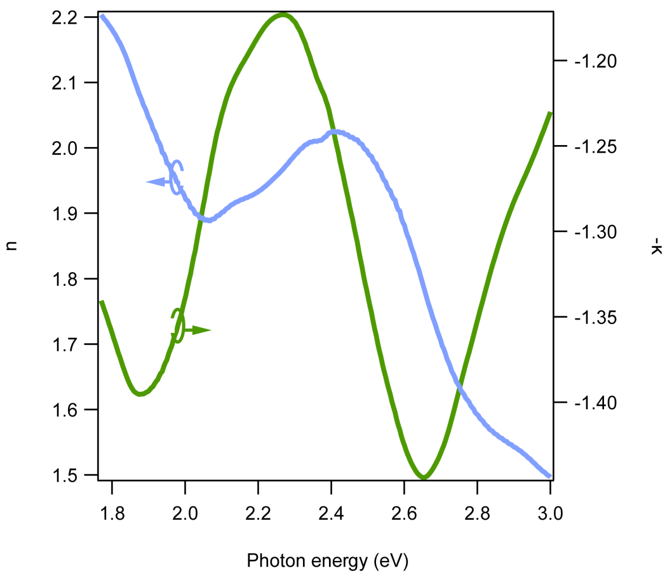

Figure 4-6: Computed index of refraction of bulk CrI_3. Real (n) and imaginary (κ) components are plotted as a function of photon energy in the visible range.

This provides a fast and reliable method for the characterization of few-layer CrI_3 flakes.

4.7.4 Thin film interferometry and the MOKE signal in CrI_3

Linearly polarized light is an equal superposition of right-circularly and left-circularly polarized light (RCP and LCP, respectively). When a phase difference accrues between the RCP and LCP components, the polarization axis of the linearly polarized light rotates. This rotation can be observed in any material that exhibits circular birefringence. In magnetic samples, such as CrI_3, this birefringence arises from a nonzero magnetization, $\boldsymbol{M}$, and is known as the magneto-optical Kerr effect (MOKE) when detected in reflection geometry. A MOKE measurement then detects changes in $\boldsymbol{M}$ by exploiting the functional dependence of the Kerr rotation on the magnetization, $\theta_{\mathrm{K}}(\boldsymbol{M})$. Additional interference terms must be accounted for, however, when we discuss the Kerr rotation of a thin-film material, because reflections from the material–substrate (CrI_3–SiO_2) interface will superimpose with the reflection off the magnetic sample (Fig. 4-8). As such, this motivates a model that uses the Fresnel equations (the same formalism as in Section 4.7.3) to calculate the reflection coeffi-

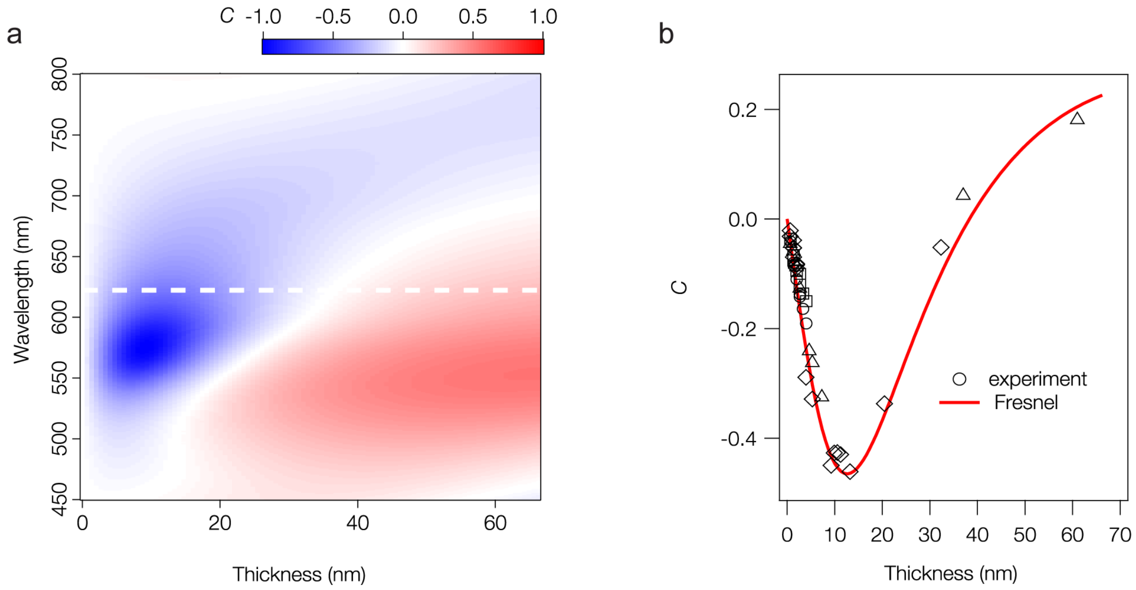

Figure 4-7: Fresnel model for the optical contrast C of CrI$_3$ flakes on 285 nm SiO$_2$/Si substrates. **a.** Dependence of C with the number of layers for a CrI$_3$ flake as a function of the illumination wavelength. **b.** Comparison of the experimental data with the computed thickness dependence of C for a sample with red light illumination (line cut at 631 nm as shown by the dashed line in **a**). The different shape markers indicate data coming from different exfoliated samples.

cients for RCP ($\tilde{\boldsymbol{r}}_+$) and for LCP ($\tilde{\boldsymbol{r}}_-$) light. The phase difference between $\tilde{\boldsymbol{r}}_+$ and $\tilde{\boldsymbol{r}}_-$ then, is the Kerr rotation:

$$\theta_{\mathrm{K}} = arg(\tilde{\boldsymbol{r}}_+) - arg(\tilde{\boldsymbol{r}}_-) \tag{4.5}$$

To obtain the index of refraction for CrI$_3$ when fully spin polarized, we work in Cartesian coordinates and use a dielectric tensor of the form [90]:

$$\boldsymbol{\varepsilon} = \begin{bmatrix} \tilde{\varepsilon}_{xx} & iQM & 0 \\ -iQM & \tilde{\varepsilon}_{xx} & 0 \\ 0 & 0 & \tilde{\varepsilon}_{zz} \end{bmatrix} \tag{4.6}$$

where Q is the complex Voigt constant and M is the out-of-plane (parallel to the z axis) component of the magnetization, which we assume is constant for all CrI$_3$ thicknesses when fully spin-polarized. This form of the dielectric tensor for a magnetic

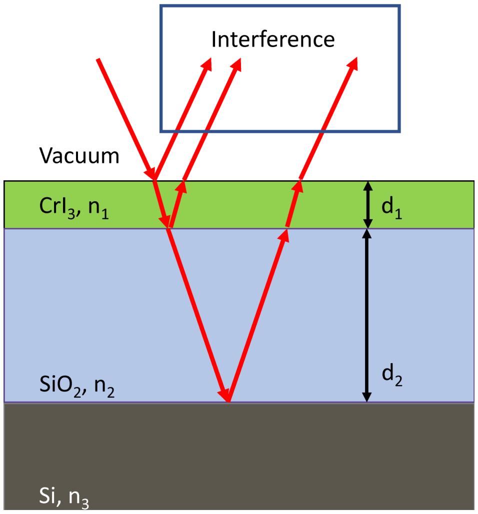

Figure 4-8: Thin-film interference ray diagram of CrI_3 on a silicon oxide/silicon substrate. Light incident on CrI_3 undergoes reflections at the CrI_3–SiO_2 interface (green–blue boundary) as well as the SiO_2–Si interface (blue–grey boundary). These reflections interfere with the initial reflection off the CrI_3 flake to produce thin-film interference that depends on the CrI_3 layer thickness, d_1, as well as the SiO_2 thickness, d_2. The underlying silicon wafer is assumed to be semi-infinite. The indices of refraction for CrI_3, SiO_2, and Si are n_1, n_2, and n_3, respectively.

sample is valid assuming (1) that the crystal exhibits at least threefold symmetry; (2) that $\boldsymbol{M}$ is parallel to the axis of rotation that gives rise to the threefold symmetry; and (3) that the axis of rotation is chosen to be the z axis. Solving for the normal modes, we obtain the eigenvalues:

$$\tilde{n}_{\pm} = \sqrt{\tilde{\varepsilon}_{xx} \pm QM} \tag{4.7}$$

and the eigenvectors:

$$\boldsymbol{D}_{\pm} = (E_x \pm iE_y)\hat{\boldsymbol{z}} \tag{4.8}$$

where $\tilde{n}_+$ and $\boldsymbol{D}_+$ denote the eigenvalue and eigenvector respectively of RCP light and $\tilde{n}_-$ and $\boldsymbol{D}_-$ denote the eigenvalue and eigenvector respectively of LCP light in CrI_3.

The complex dielectric component $\tilde{\varepsilon}_{xx}$, when related to the $\tilde{n}$ defined in equation (4.3a), is:

$$\tilde{\varepsilon}_{xx} = n^2 - \kappa^2 - 2in\kappa \tag{4.9}$$

where the value of $\tilde{\varepsilon}_{xx}$ derived from the n and κ values at about 1.96 eV (modeled in Fig. 4-6). It is apparent from equation (4.7) that we should not expect θ_K to depend linearly on $\boldsymbol{M}$ and layer number. In addition, interference from reflections off the CrI_3–SiO_2 interface will give rise to a non-trivial functional form of θ_K with respect to layer thickness. There is no determination of Q in the literature for CrI_3, so we varied Q as a complex parameter and constrained it to a small range that fitted experimental θ_K values from our MOKE measurements on trilayer and bulk CrI_3. These calculations qualitatively describe the large increase in θ_K moving from monolayer to trilayer, as well as the negative θ_K seen at positive $\mu_0 H$ for bulk flakes. However, this simple model does not incorporate layer-dependent electronic structure changes, seen in other atomically thin van der Waals materials such as MoS_2 [4], and evident in this system as a change in magnetic ground states from monolayer to bilayer.

4.7.5 Atomic force microscopy of encapsulated few-layer CrI_3

CrI_3 samples exfoliated under an inert atmosphere were encapsulated to preserve the CrI_3 flakes during atomic force microscopy (AFM) studies under ambient conditions. Using an all-dry viscoelastic stamping technique [31] inside the glovebox, CrI_3 flakes were sandwiched between two layers of approximately 5 nm thick graphite to prevent reaction with oxygen and moisture. Encapsulated CrI_3 flakes could then be safely removed from the glovebox for further study. AFM of graphite-encapsulated CrI_3 flakes was measured using a Bruker Dimension Edge atomic force microscope in tapping mode. Fig. 4-9 shows AFM results for bilayer and trilayer CrI_3 flakes encapsulated in approximately 5 nm thick graphite layers. Their corresponding MOKE data are consistent with bare samples.

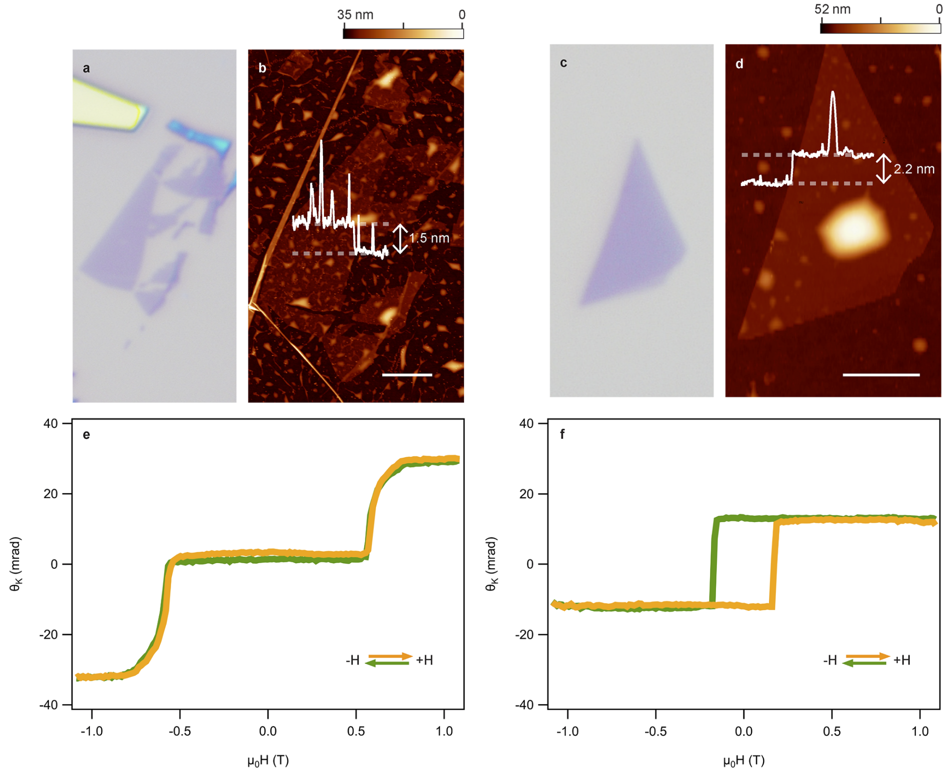

Figure 4-9: AFM and MOKE measurements of graphite-encapsulated few-layer CrI_3. **a.** Optical microscope image of a bilayer CrI_3 flake on a 285 nm SiO_2/Si substrate. **b.** AFM data for the CrI_3 flake in a encapsulated in graphite, showing a line cut across the flake with a step height of 1.5 nm. **c.** Optical microscope image of a trilayer CrI_3 flake on a 285 nm SiO_2/Si substrate. **d.** AFM data for the CrI_3 flake shown in **c** encapsulated in graphite. A line cut taken across the flake shows a step height of 2.2 nm. Both scale bars are 2 μm. **e** and **f** show the MOKE signal as a function of applied magnetic field for the encapsulated bilayer in **b** and the encapsulated trilayer in **d**, respectively.

Chapter 5

Electrical control of 2D magnetism in bilayer CrI_3

The following chapter is based on work published in *Nature Nanotechnology* (Ref. [155]), and appears here with modifications, corrections, and expanded discussions.

5.1 Introduction

Controlling magnetism via electric fields addresses fundamental questions of magnetic phenomena and phase transitions [156–158], and enables the development of electrically coupled spintronic devices, such as voltage-controlled magnetic memories with low operation energy [159–161]. Previous studies on dilute magnetic semiconductors such as (Ga,Mn)As and (In,Mn)Sb have demonstrated large modulations of the Curie temperatures and coercive fields by altering the magnetic anisotropy and exchange interaction [37, 157, 159, 162, 163]. Owing to their unique magnetic properties [8, 148, 149, 164, 165], the recently reported two-dimensional magnets provide a new system for studying these features [7, 41, 43, 92, 166]. For instance, a bilayer of chromium triiodide (CrI_3) behaves as a layered antiferromagnet with a magnetic field-driven metamagnetic transition [7, 92]. Here, we demonstrate electrostatic gate control of magnetism in CrI_3 bilayers, probed by magneto-optical Kerr effect (MOKE) microscopy. At fixed magnetic fields near the metamagnetic transition, we realize voltage-controlled switching between antiferromagnetic and ferromagnetic states. At zero magnetic field, we demonstrate a time-reversal pair of layered antiferromagnetic states that exhibit spin-layer locking, leading to a linear dependence of their MOKE signals on gate voltage with opposite slopes. Our results allow for the exploration of new magnetoelectric phenomena and van der Waals spintronics based on 2D materials.

5.2 Gated bilayer CrI_3 device structure

Bilayer CrI_3 is a layered antiferromagnet with a Néel temperature of about 45 K [7,92]. As shown in Fig. 5-1a, spins within each monolayer are aligned ferromagnetically (FM) out of plane, while their interlayer coupling is antiferromagnetic (AFM); this results in a vanishing net magnetization. In principle, there are two energetically degenerate AFM ground states, which form a time-reversal pair. We label this $\uparrow\downarrow$ and $\downarrow\uparrow$, where the first and second arrows denote the out-of-plane magnetizations in the top and bottom layers, respectively. Previous work has shown that, on increasing the magnetic field in the out-of-plane direction, bilayer CrI_3 undergoes a metamagnetic transition from a layered AFM state to an FM state ($\uparrow\uparrow$ or $\downarrow\downarrow$) [7,110,111]. Magnetic fields of about 0.6–0.8 T are sufficient to drive the metamagnetic transition, indicating that the interlayer AFM coupling is weak and on the same energy scale. This layered AFM ordering with weak AFM coupling across the van der Waals gap presents an opportunity to realize electrically tunable magnetism.

To explore gate-controlled magnetoelectric effects, we fabricated gated bilayer CrI_3 devices. Bulk CrI_3 crystals were mechanically exfoliated onto 285 nm SiO_2/Si substrates in an argon glovebox to obtain bilayer CrI_3 flakes (see Section 5.8.1). The structure of a representative bilayer CrI_3 device is shown in Fig. 5-1b. This device is a vertical stack composed of a bilayer CrI_3 flake and a graphite contact encapsulated between two hexagonal boron nitride (BN) flakes and a graphite top gate (see Section 5.8.1) [31]. The BN flakes protect the bilayer CrI_3 from degradation under ambient conditions and also act as dielectric layers for electrostatic doping upon gating. Figure

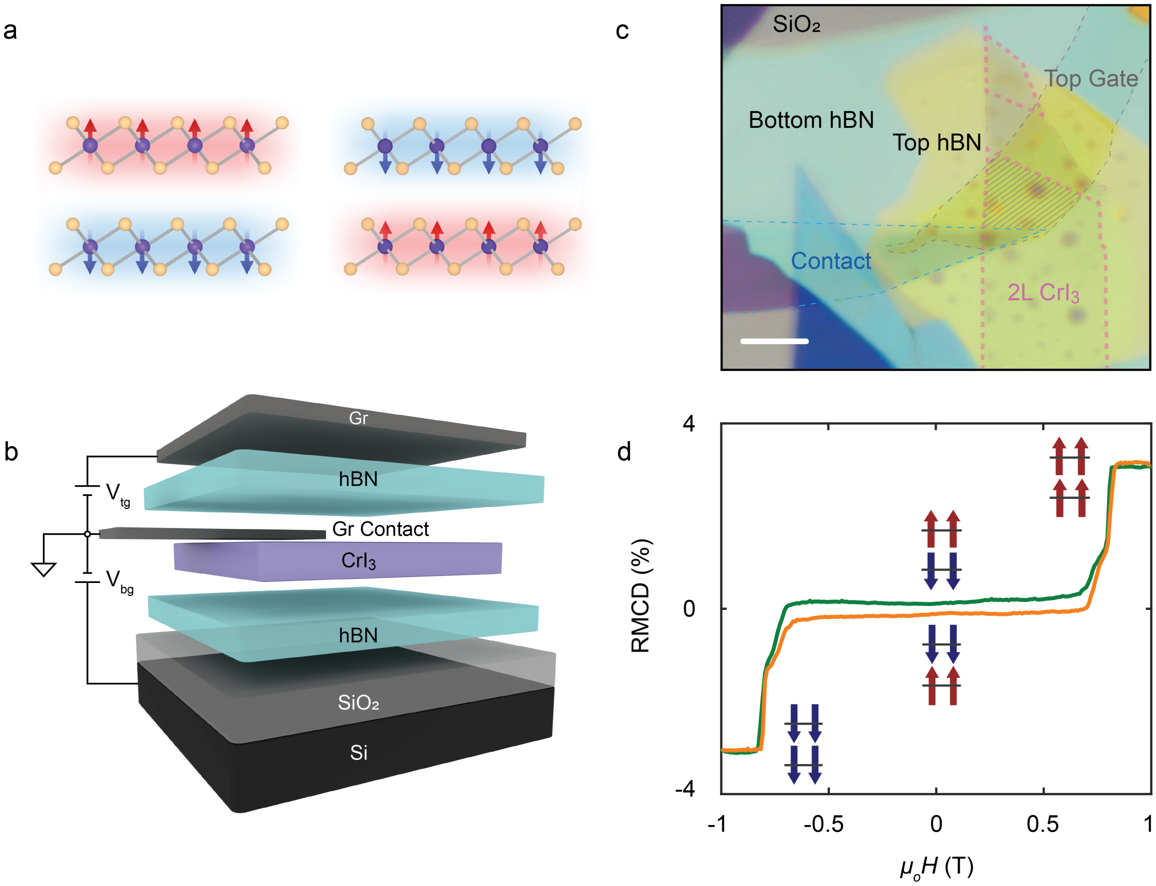

Figure 5-1: Bilayer CrI_3 spin ordering, gated device structure, and RMCD without gating. **a.** Magnetic ordering in bilayer CrI_3 in the two energetically degenerate AFM ground states, labelled ↑↓ (left) and ↓↑ (right) in the text, when cooled below the Néel temperature. Cr^{3+} and I^- ions are shown as purple and orange balls, respectively. **b.** Schematic of a dual-gated bilayer CrI_3 device fabricated by van der Waals assembly. **c.** False-color optical micrograph of a representative device (Device 1). Scale bar, 5 μm. A small four-layer CrI_3 piece (thin pink dashed line) interconnects the two bilayer (2L) sections of the flake (thick pink dashed line). **d.** RMCD signal of a bilayer CrI_3 device (Device 1) as a function of perpendicular magnetic field at zero gate voltage.

5-1c presents a bright-field micrograph of a gated bilayer CrI_3 device. The out-of-plane magnetization was probed either by polar magneto-optical Kerr effect (MOKE) microscopy for devices without a top gate or by reflectance magneto-circular dichroism (RMCD) microscopy for dual-gated devices. Both techniques directly measure the out-of-plane magnetization (see Section 5.8.2) [91]. A 633 nm HeNe laser focused to a 1 μm beam spot with 10 μW of optical power was used for all experiments, which were performed at 15 K unless otherwise specified.

Figure 5-1d shows a representative RMCD signal of dual-gated bilayer $\mathrm{CrI_3}$ (Device 1) as a function of an out-of-plane magnetic field ($\mu_0 H$) at zero gate voltage. The orange curve corresponds to sweeping $\mu_0 H$ from a negative to a positive value, and the green curve shows the time-reversed process. For magnetic fields smaller than 0.8 T, the RMCD signal nearly vanishes, corresponding to the layered AFM states, either ↑↓ or ↓↑. However, unlike the as-exfoliated bilayer samples measured without van der Waals assembly [7], there is a remnant RMCD signal, implying that the net magnetization is not completely suppressed in the AFM configurations. We often observe this remnant RMCD signal in bilayer devices that have been through the van der Waals assembly process. This could be caused by breaking out-of-plane symmetry of the bilayer during device fabrication such that the magnetizations from the two layers do not exactly cancel. At a critical field, $\mu_0 H_c = \pm 0.8$ T, we observe a sharp jump in the RMCD signal from near-zero up to 3%, and this increased signal is spatially homogeneous across the entire device (Fig. 5-5). This is consistent with the previous report for as-exfoliated bilayer $\mathrm{CrI_3}$, implying that an external magnetic field drives a metamagnetic transition in which the bilayer switches from the layered AFM states (↑↓ or ↓↑) to an FM state (↑↑ or ↓↓) [7].

5.3 Gate tunability of the metamagnetic transition in bilayer $\mathrm{CrI_3}$

Remarkably, the metamagnetic transition is highly controllable by electrostatic gating. We performed MOKE measurements on a second device fabricated with a single gate (Device 2) while varying both the magnetic field and gate voltage. In this device, we apply the gate voltage through a $\mathrm{SiO_2/Si}$ back gate while leaving the bilayer $\mathrm{CrI_3}$ uncovered to minimize the impact of device fabrication on the $\mathrm{CrI_3}$ bilayer. Figure 5-2a presents a plot of MOKE intensity, θ_{K}, as a function of the back-gate voltage V_{bg} and $\mu_0 H$ (sweeping down). In this magnetic phase diagram, the light color represents low MOKE signal arising from a layered AFM state, and the darker red and blue colors represent the two FM states with strong MOKE signals of opposite signs. Based on this phase diagram, the phase boundary, that is, the critical field for the metamagnetic transition, strongly depends on V_{bg}.

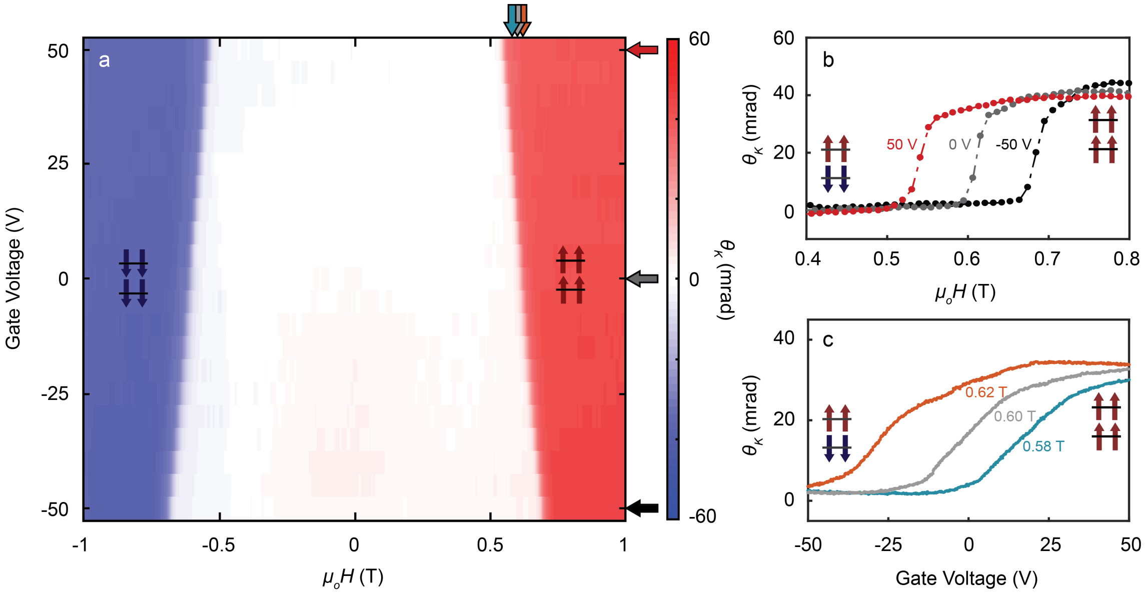

Figure 5-2: MOKE signal versus gate voltage and applied magnetic field. **a.** Intensity of the polar MOKE signal, θ_{K}, of a non-encapsulated bilayer $\mathrm{CrI_3}$ device (Device 2) as a function of both gate voltage and applied magnetic field. **b.** Selected horizontal line cuts from **a** demonstrating the gate-induced change in critical field of the metamagnetic transition at V_{bg} = -50 V (black), 0 V (grey), and 50 V (red). **c.** Gate-induced transition from layered AFM to FM states at selected $\mu_0 H$ = 0.58 T (blue), 0.60 T (grey), and 0.62 T (orange).

In Fig. 5-2b, we look closer at the metamagnetic transition by comparing the magnetic field dependence at $V_{\mathrm{bg}} = 0$ V and ±50 V (horizontal line cuts of the phase map of Fig. 5-2a). The critical field $\mu_0 H_c$ has shifted by roughly 0.2 T, from 0.7 T at -50 V to 0.5 T at 50 V. Considering that the critical field is about 0.6 T for V_{bg} = 0 V, this corresponds to tuning the critical field by around 30% via electrostatic gating. The shift in $\mu_0 H_c$ is bidirectional and linear; that is, when a positive gate voltage is applied, the absolute value of the critical field is decreased, and vice versa for negative gate voltages.

Due to this strong dependence of the critical field on the gate voltage, we can then realize an electrically controlled transition between the layered AFM and FM phases when the magnetic field is fixed near $\mu_0 H_c$. Figure 5-2c shows such an electrically controlled magnetic phase transition at three selected magnetic fields, corresponding to vertical line cuts on the phase map in Fig. 5-2a. The MOKE signal starts near zero at negative gate voltages, corresponding to AFM ordering. As the voltage increases to a critical value, the MOKE signal quickly rises and reaches a saturated value, demonstrating electrical switching to the FM state. For the three selected magnetic fields ranging from 0.58 to 0.62 T, the required voltage to initiate the transition from the layered AFM states to the FM $\uparrow\uparrow$ state shifts towards positive gate voltage with decreasing applied magnetic field.

In single-gated devices, an applied gate voltage introduces both an interlayer bias and layer-dependent electrostatic doping. To determine which of the two effects dominates the gate-tunable magnetic phase transition, we investigated a dual-gated device to enable independent control over the doping and electric field. Under application of a single gate, the dual-gated device behaves similarly to Device 2 (Figs. 5-6 and 5-7). After identifying the critical field for the metamagnetic transition, we fixed the magnetic field near the transition and measured the RMCD signal as a function of both gates.

5.4 Investigating the origin of voltage-controlled metamagnetism

Figure 5-3a shows the RMCD intensity plot as a function of both top- and back-gate voltages at $\mu_0 H = 0.78$ T. The graphite top gate was swept between +6 and -6 V and the silicon back gate between +15 and -15 V. The red region on the right is the large, positive signal from the $\uparrow\uparrow$ state, and the pink region on the left is the much smaller signal from the layered AFM state. Using a parallel-plate capacitor model [3, 14, 167], we estimated the constant-doping and constant-field contours on the phase map (see Section 5.8.3). The metamagnetic transition, that is, the boundary between the red and pink regions, lies nearly parallel to the constant-doping contours as indicated by the dashed line in Fig. 5-3a (for the time-reversal counterpart at negative magnetic fields, see Fig. 5-8). Though CrI_3 is insulating, recent transport measurements on few-layer devices have shown electron (n-type) conduction at room temperature, implying that it is possible to electrostatically dope CrI_3 [113]. To further confirm this, we performed magnetic field sweeps of the RMCD signal at several doping levels with the same displacement field (Fig. 5-3b), and at several displacement fields with the same doping level (Fig. 5-3c). These clearly show that the doping level dominantly affects the critical field. This is not surprising, because in other magnetic systems, doping leads to modulation of orbital occupation [157, 159, 162, 163], exchange interactions, and magnetic anisotropy [168–172], and thus a change in the magnetism. Our observation may stimulate theoretical investigations of whether doping in 2D magnets introduces similar modulation effects.

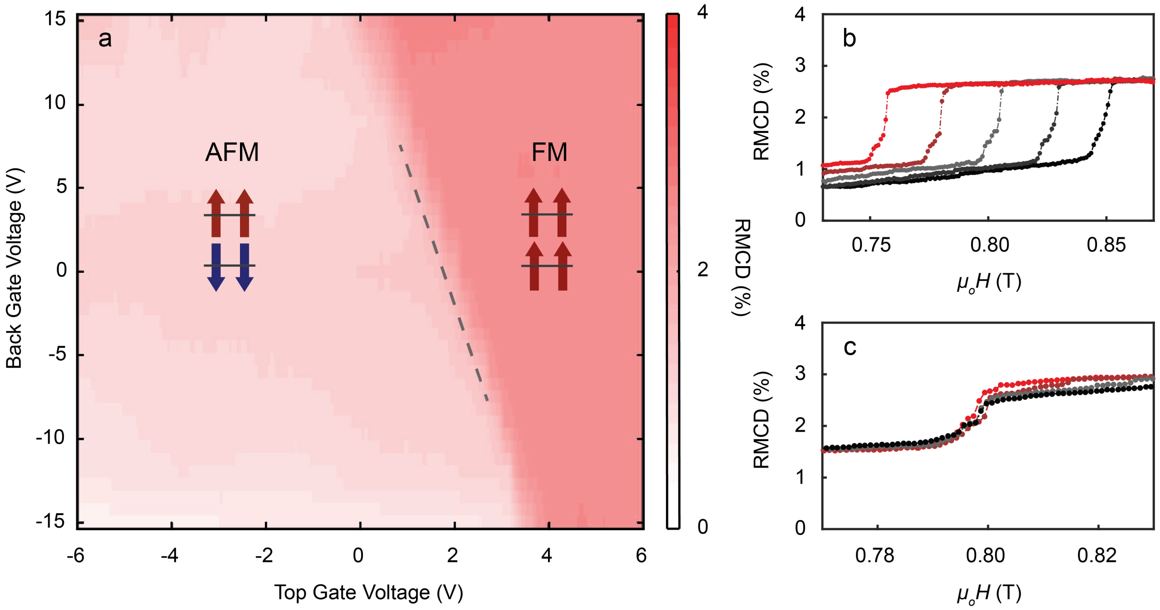

Figure 5-3: Origin of voltage-controlled metamagnetism. **a.** RMCD signal of a dual-gated device (Device 1) when sweeping both the graphite top gate and silicon back gate. The pink region reflects negligible RMCD signal, corresponding to the layered AFM states. The red region corresponds to the FM ↑↑ state. The boundary between them is parallel to a constant-doping contour (grey dashed line). **b.** RMCD signal of the same device as a function of applied magnetic field at estimated doping levels from 0 cm^{-2} (black) to 4.4×10^{12} cm^{-2} (red) for zero displacement field. **c.** RMCD signal as a function of applied magnetic field at several displacement fields ranging from 0 V/nm (red) to 0.6 V/nm (black) for zero doping. The metamagnetic transition is clearly insensitive to changes in the displacement field but strongly dependent on doping level.

5.5 Electrical control of layered magnetism at zero magnetic field

In addition to gate-voltage tuning of the metamagnetic transition, we also realized electrical control of the layered AFM states at zero magnetic field. We first prepared the system by starting in the ↑↑ state with an applied magnetic field of 1 T, and then swept the field back to zero (Initialization 1, inset Fig. 5-4a). Remaining at zero external magnetic field, we swept the back-gate voltage and observed a MOKE signal linearly dependent on the voltage with a slope of -0.04 mrad/V (Fig. 5-4a). Similarly, we prepared the bilayer for its time-reversal state by starting in the ↓↓ state with a magnetic field of -1 T and sweeping the field back to zero (Initialization 2, inset Fig. 4b). In Fig. 5-4b, the MOKE signal also exhibits a linear dependence on the gate voltage, but with an opposite slope of 0.04 mrad/V. These results demonstrate that the two initialization processes lead to two distinct layered AFM states, ↑↓ and ↓↑, which are a time-reversed pair, and that we have full electrical tunability over the AFM states even at zero magnetic field.

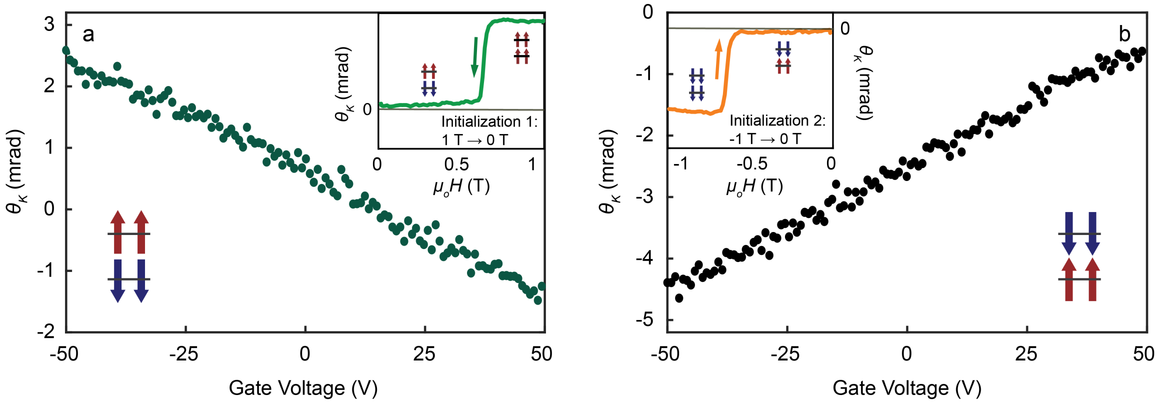

Figure 5-4: Gate-voltage-induced MOKE of layered AFM states at zero magnetic field. **a.** Gate-dependent MOKE signal of a non-encapsulated bilayer CrI_3 device (Device 2) prepared in the ↑↓ state following the initialization depicted in the inset (see main text for details). **b.** Equivalent measurement performed on the device prepared in the ↓↑ state by the initialization process in the inset. The opposite slopes of the MOKE signal for ↑↓ and ↓↑ highlight the spin-layer locking effect with gate-induced MOKE. Insets, initialization processes for preparing AFM states at zero field (discussed in the main text).

This observed magnetoelectric coupling in the layered AFM states is a result of broken time-reversal and inversion symmetry due to the applied gate voltage [173], and can be intuitively explained by the spin-layer locking effect. For an AFM state at zero field, the spin (magnetization) orientation is locked to the layer pseudospin that labels the geometric top and bottom layers (Fig. 5-1a). A direct consequence of this spin-layer locking effect is that the creation of a layer polarization is accompanied by a net magnetization [174,175]. In the AFM configuration, the opposite spin orientations of the two layers quench the interlayer hopping and hence the layer hybridization [167,174]. Application of an electrostatic gate voltage then creates a layer polarization of the carriers, resulting in net magnetizations of opposite signs in the ↑↓ and ↓↑ states.

The layer polarization and hence net magnetization has a linear dependence on the gate voltage, consistent with the observed gate dependence of the MOKE signal in Fig. 5-4. Tunability of the net magnetization with gate voltage also disappears when the bilayer device is warmed to ∼40 K, showing that the bilayer Néel temperature is unaffected within the applied gate voltage range (Fig. 5-9a,b).

Furthermore, this allows us to identify and controllably access the two energetically degenerate AFM states. The application of a positive gate voltage results in a larger electron density in the bottom layer than in the top layer. If the bilayer is in the $\uparrow\downarrow$ state, the net magnetization then points down with a negative slope of the MOKE signal as a function of gate voltage. The $\downarrow\uparrow$ state will then have a positive slope in the gate-dependent MOKE signal. Though the device assembly process may already break the degeneracy between the $\uparrow\downarrow$ and $\downarrow\uparrow$ states, the signs of the gate-dependent MOKE slopes are nevertheless fingerprints for distinguishing between the two AFM states. Based on Fig. 5-4a,b, we can definitively determine that, by using Initialization 1, the $\uparrow\uparrow$ state transitions to the $\uparrow\downarrow$ state, and by using Initialization 2, the $\downarrow\downarrow$ state transitions to the $\downarrow\uparrow$ state.

5.6 Conclusion

In summary, we have demonstrated two forms of electrical control of magnetism in a van der Waals layered AFM insulator, bilayer CrI_3. First, in an applied magnetic field, the critical field for the metamagnetic transition can be tuned by up to 30% by applying a gate voltage, allowing a gate-voltage-driven phase transition from a layered AFM phase to an FM phase. Dual gate studies show that the mechanism is dominated by electrostatic doping. Second, at zero magnetic field, the net magnetization can be continuously tuned by gate voltage. The two AFM states, $\uparrow\downarrow$ and $\downarrow\uparrow$, show the same linear dependence of the MOKE signal on gate voltage but with opposite signs, which provides an experimental measure to distinguish these two degenerate magnetic states. Our work shows that van der Waals magnets provide a new system for exploring magnetoelectric effects and their potential applications in gate-tunable spintronics.

5.7 Epilogue

At the same time of this publication, another group released similar results on the gate control of bilayer CrI_3 [176,177]. The first paper [176] demonstrates the same effect of electrostatic doping on the magnetic order. Upon application of a gate voltage of 30 V, corresponding to a gate-induced doping density of approximately 2.5×10^{13} cm^{-2}, they achieve a coercive field reaching 0. At this point, the bilayer adopts a ferromagnetic ground state in the absence of an applied magnetic field. The magnetization and transition temperature also follow a direct dependence on the doping level.

In the second paper [177], they observe a linear magnetoelectric (ME) effect in which the displacement electric field does indeed influence the observed RMCD signal at fixed density. They find a linear response in magnetization $\Delta M/M_0$ with D at zero magnetic field. Importantly, the responses are equal and opposite after training at large positive and negative fields. These results agree with our observations of a degeneracy breaking between the two antiferromagnetic states $\uparrow\downarrow$ and $\downarrow\uparrow$ (Fig. 5-4). At an applied magnetic field above the coercive field, when 2L CrI_3 is in the ferromagnetic state, they find negligible ME effect. These observations can be understood by considering the symmetry conditions required for a linear ME effect. Both time-reversal and spatial-inversion symmetries must be simultaneously broken. While both AFM and FM 2L CrI_3 break time-reversal symmetry, only the AFM state also breaks spatial-inversion symmetry to enable this ME effect to occur. The exact microscopic mechanism behind this coupling between magnetization and electric field is still unknown and would be an interesting direction of further research.

5.8 Supplemental Information

5.8.1 Device fabrication

Bulk CrI_3 crystals were grown by the direct vapor transport method as previously reported [7,41]. All fabrication using these crystals was performed in a glovebox with an argon atmosphere. The crystals were mechanically exfoliated onto either 285 nm SiO_2/Si substrates for dual-gated devices (for example, Device 1) or the commercially available viscoelastic polymer gel film from Gel-Pak (for example, Device 2). Bilayer monocrystalline flakes were identified by their optical contrast relative to the substrate using methods discussed in Section 4.7.3.

Van der Waals assembly of the stack for a dual-gated device was performed in the glovebox using the dry transfer polymer technique with a poly(bisphenol A carbonate) (PC) film placed over a polydimethylsiloxane (PDMS) square serving as our stamp [31]. The flakes were picked up sequentially: graphite top gate, top BN, graphite contact, bilayer CrI_3, bottom BN.

Metallic Cr/Pd contacts on 285 nm SiO_2/Si substrates were prepared using standard electron-beam lithography and bilayer poly(methyl methacrylate) (PMMA) resist fabrication techniques. Each chip was fixed to a dual in-line package socket with silver paint and wire-bonded to the socket.

The completed dual-gated stacks were transferred on top of the Cr/Pd contacts and released by heating to 170°C. The non-encapsulated devices were fabricated by transferring the as-exfoliated bilayer CrI_3 flake on gel film directly onto the metallic contacts. Finally, each socket was sealed with a glass coverslip using Crystalbond 509 (Ted Pella) under inert conditions to permit optical measurements. Additional details on sealing air-sensitive devices can be found in Appendix B.

5.8.2 MOKE and RMCD microscopy

Materials that exhibit an out-of-plane magnetization $\boldsymbol{M}$ may also display magnetic circular birefringence (MCB) and magnetic circular dichroism (MCD). Both MCB and MCD accrue a difference in the phase and amplitude, respectively, between right- and left-circularly polarized (RCP, LCP) light that vary as a function of $\boldsymbol{M}$. When linearly polarized light, an equal superposition of RCP and LCP, is normally incident and reflects off the magnetized material, the phase difference between RCP and LCP leads to a rotation of the linear polarization through an angle θ_{K} from the magneto-optical Kerr effect (MOKE) and induces ellipticity through RMCD.

Both MOKE and RMCD measurements were performed in a closed-cycle helium cryostat with a base temperature of 15 K. A superconducting solenoidal magnet allowed fields of up to 7 T in the Faraday geometry to be applied on all devices. The AC lock-in measurement technique used to measure the MOKE and RMCD signal closely follows previous characterizations of the magnetic order in atomically thin $\mathrm{CrI_3}$. For RMCD measurements, the analyzing polarizer was removed, and the lock-in frequency was set to the fundamental frequency of the photoelastic modulator (PEM) rather than its second harmonic [7,91].

5.8.3 Calculation of constant doping line

Following the methodology from refs. [14,167], our dual-gated bilayer $\mathrm{CrI_3}$ device can be approximated as a parallel-plate capacitor to obtain the constant doping (n) and constant electric displacement field ($\boldsymbol{D}$) contours for the dual gate phase map. The parallel-plate capacitor model can be an oversimplified calculation for obtaining the doping levels. Nonetheless, we use it to estimate the doping level n, which has the form

$$n = C_{\mathrm{bg}}(V_{\mathrm{bg}} - V_{\mathrm{bg}}^{D}) + C_{\mathrm{tg}}(V_{\mathrm{tg}} - V_{\mathrm{tg}}^{D}) \tag{5.1}$$

where C is the areal capacitance, V_{bg} and V_{tg} are the back- and top-gate voltages, respectively, and V_{bg}^{D} and V_{tg}^{D} are the charge neutral point voltages. Because the aim of this calculation is to show whether the metamagnetic transition shown in Fig. 5-3a arises from a change in n or a change in $\boldsymbol{D}$, we can find one such constant-doping contour by setting $n = V_{\mathrm{tg}} = V_{\mathrm{bg}} = 0$, as these terms only offset the contour by an arbitrary constant. The areal capacitance is given as $C = \varepsilon/d$, where ε is the permittivity of the dielectric layer and d is the thickness of the dielectric layer. Including the bottom BN encapsulation layer with the $\mathrm{SiO_2}$ dielectric layer in the bottom areal capacitance, equation (5.1) for Device 1 simplifies to

$$V_{\mathrm{tg}} = -\frac{d_{\mathrm{BN}}}{\frac{\varepsilon_{\mathrm{BN}}}{\varepsilon_{\mathrm{SiO_2}}} d_{\mathrm{SiO_2}} + d_{\mathrm{BN}}} V_{\mathrm{bg}} \tag{5.2}$$

The out-of-plane static dielectric constants of BN and SiO_2, $\varepsilon_{\mathrm{BN}}$ and $\varepsilon_{\mathrm{SiO_2}}$, respectively, are 4 and 3.9 (ref. [110]). The device sits on top of 285 nm SiO_2 substrate, and both top and bottom BN flakes were 30 nm. Similarly, we can also obtain the zero-displacement field contour by starting with the general expression for the applied displacement field:

$$D = C_{\mathrm{bg}}(V_{\mathrm{bg}} - V_{\mathrm{bg}}^{D}) - C_{\mathrm{tg}}(V_{\mathrm{tg}} - V_{\mathrm{tg}}^{D}) \tag{5.3}$$

and removing the same terms as when obtaining equation (5.2):

$$V_{\mathrm{tg}} = \frac{d_{\mathrm{BN}}}{\frac{\varepsilon_{\mathrm{BN}}}{\varepsilon_{\mathrm{SiO_2}}} d_{\mathrm{SiO_2}} + d_{\mathrm{BN}}} V_{\mathrm{bg}} \tag{5.4}$$

5.8.4 Additional RMCD measurements of Device 1

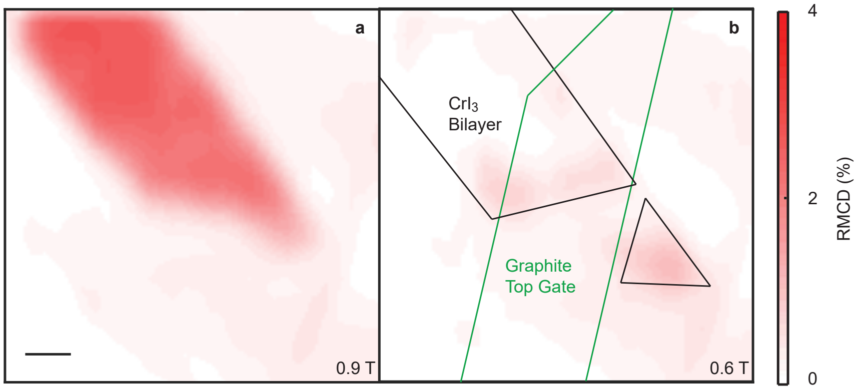

Figure 5-5: RMCD maps at fixed magnetic fields near the metamagnetic transition. RMCD map of Device 1 in the absence of gate voltage with an applied magnetic field values of (**a**) 0.9 T and (**b**) 0.6 T. These maps show the metamagnetic transition from the fully spin-polarized ferromagnetic state ↑↑ (red) to the layered antiferromagnetic state ↑↓ (white) near the critical field regime. The ferromagnetism beyond the metamagnetic transition is homogeneous across the entire bilayer. The scale bar is 5 µm.

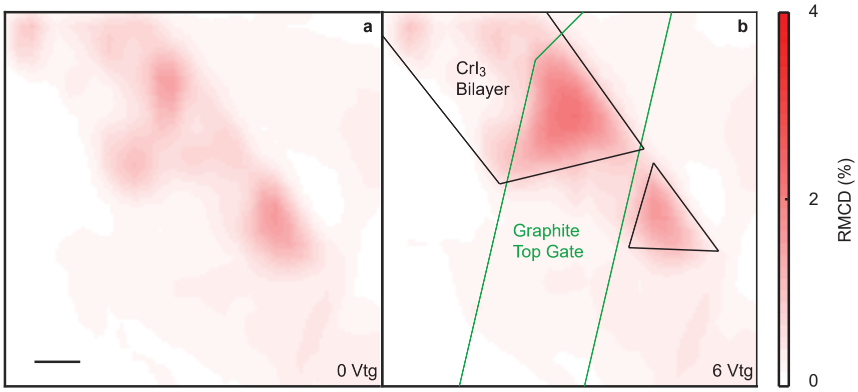

Figure 5-6: RMCD maps at fixed top gate voltages. **a.** RMCD map of Device 1 with an applied magnetic field of 0.8 T in the absence of gating. The scale bar is 5 μm. **b.** RMCD map of the same region as in **a** at a magnetic field of 0.8 T with zero back gate voltage and 6 V applied to the graphite top gate. Similar to the gate voltage sweeps of the RMCD signal in Fig. 5-2c, we are able to electrically switch the antiferromagnetic state (light pink) to the ferromagnetic ↑↑ state (red) by applying a positive top gate voltage on the bilayer CrI_3 flake. This also illustrates the homogeneity of the gating across the portion of the bilayer flake under the graphite top gate.

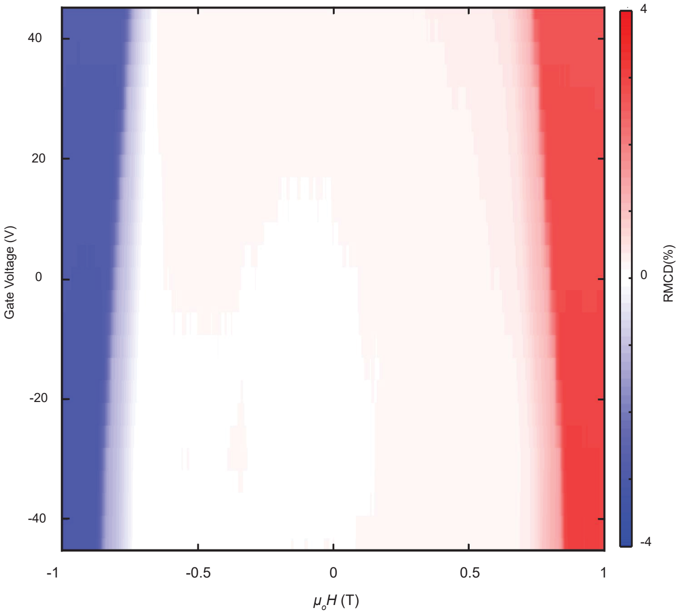

Figure 5-7: Single-gate RMCD measurements vs. gate-voltage and magnetic field on Device 1. RMCD intensity as a function of applied back gate voltage and magnetic field. Maintaining the same convention as in Fig. 5-2a, the bright red region corresponds to a large positive RMCD signal associated with the ferromagnetic ↑↑ state, while the dark blue region shows large negative RMCD signal that corresponds to the ↓↓ state. The light regions in between the blue and red regions are instances where the RMCD signal is near-zero and when the bilayer is in a layered antiferromagnetic state. Consistent with Device 2, the critical field of the metamagnetic transition lowers as a positive gate voltage is applied and vice versa for negative gate voltages.

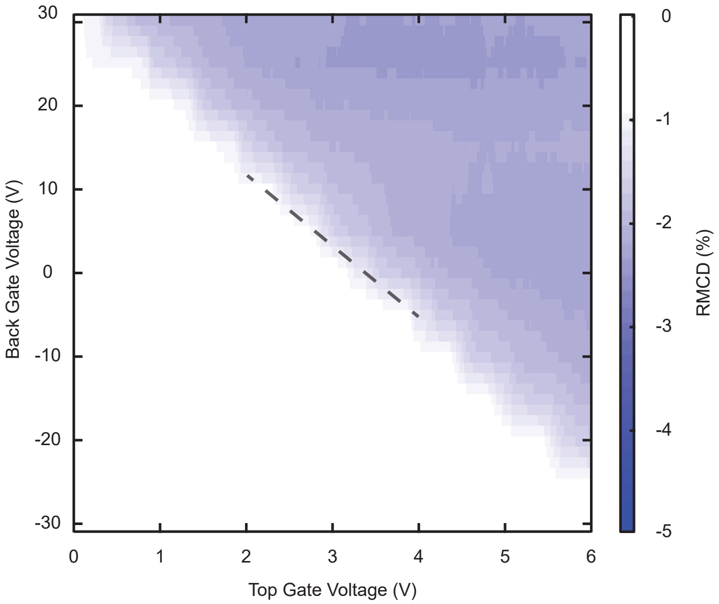

Figure 5-8: Dual-gate phase map at the negative metamagnetic transition. Phase map of the RMCD signal as a function of both the top gate and back gate voltages in Device 1. The blue region represents a strong, negative RMCD signal, *i.e.* when the bilayer is in the ferromagnetic ↓↓ state, whereas the white region represents the absence of RMCD signal of the antiferromagnetic ↓↑ state. The grey dashed line shows a constant doping contour. Similar to the phase boundary seen in the positive metamagnetic transition dual-gate phase map (Fig. 5-3a), the negative metamagnetic transition also reveals doping to be the dominant factor in tuning the magnetic states at large negative fields.

5.8.5 Gate-dependent MOKE signal versus temperature

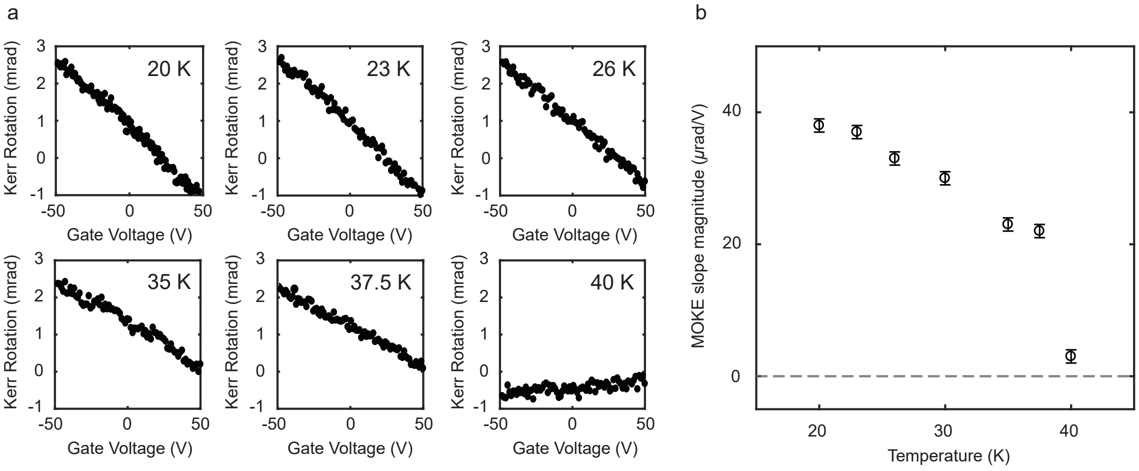

Figure 5-9: Gate-dependent MOKE at increasing fixed temperatures with no applied magnetic field. **a.** MOKE signal of the bilayer (Device 2) prepared in the ↑↓ AFM state with no applied magnetic field at several fixed temperatures ranging from 20 K to 40 K. **b.** The extracted slope magnitudes of the linear gate-dependent MOKE signal at each fixed temperature from **a**, as well as at 30 K, using a least-squares fit. The error bars are a standard deviation of the fitted slopes. As the device is warmed, the linear dependence of the MOKE signal on gate voltage decreases, showing that the tunability of the net magnetization weakens and is inversely related to the temperature. Above the Néel temperature at ∼40 K, there is no dependence of the MOKE signal on the gate voltage, signalling that the layered antiferromagnetic order and hence the spin-layer locking effect is destroyed. In addition, the disappearance of the MOKE signal for all gate voltages at 40 K implies that the Néel temperature is the same regardless of the applied gate voltage. Therefore, the electric field effect does not affect the Néel temperature of bilayer CrI_3.

Chapter 6

Probing magnetism in 2D van der Waals crystalline insulators via electron tunneling

The following chapter is based on work published in *Science* (Ref. [110]), and appears here with modifications, corrections, and expanded discussions.

6.1 Abstract

Magnetic insulators are a key resource for next-generation spintronic and topological devices. The family of layered metal halides promises varied magnetic states, including ultrathin insulating multiferroics, spin liquids, and ferromagnets, but device-oriented characterization methods are needed to unlock their potential. Here, we report tunneling through the layered magnetic insulator CrI_3 as a function of temperature and applied magnetic field. We electrically detect the magnetic ground state and interlayer coupling and observe a field-induced metamagnetic transition. The metamagnetic transition results in magnetoresistances of 95, 300, and 550% for bilayer, trilayer, and tetralayer CrI_3 barriers, respectively. We further measure inelastic tunneling spectra for our junctions, unveiling a rich spectrum consistent with collective magnetic excitations (magnons) in CrI_3.

6.2 Introduction

Van der Waals magnetic insulators are a materials system that may enable designer topological states [178] and spintronic technologies [19]. The recent isolation [7, 41] of few-layer magnets with either ferromagnetic ($\mathrm{CrI_3}$, $\mathrm{Cr_2Ge_2Te_6}$) or antiferromagnetic order [43, 148] is just the tip of the iceberg. The vast family of layered metal halides [44] contains spin orders from multiferroics [179] to proximate spin liquids [54], of key interest to both fundamental and applied physics. Existing studies have focused on magneto-optical effects [7, 8, 41, 92] as a characterization tool, but a more general, device-oriented approach is needed.

Here we demonstrate that tunneling through layered insulators is a versatile probe of magnetism on the nanoscale in these materials. We report the conductance of graphite/$\mathrm{CrI_3}$/graphite junctions (Fig. 6-1A) as a function of magnetic field and temperature and electrically detect an antiferromagnetic ground state and a field-induced metamagnetic transition. The metamagnetic transition is revealed by large magnetoresistances (up to 550%) arising from the antiparallel-to-parallel reorientation of chromium spins in adjacent crystal layers. A similar effect was previously proposed [102] for synthetic multilayer magnets, but experimental realizations [104] were limited to magnetoresistances below 70%. The performance of our devices is an order of magnitude higher, corresponding to estimated spin polarization above 95%. Furthermore, the two-dimensional magnetism of $\mathrm{CrI_3}$ enables ultrathin tunnel barriers (< 3 nm) and a concomitant 10,000-fold increase in conductance (per unit area) compared to previous results [104]. The noninvasive van der Waals transfer of the magnetic layer ensures substrate-independent device integration, and together with high magnetoresistance, spin polarization, and conductance, may enable noninvasive spin injectors and detectors for next-generation spintronics experiments incorporating topological insulators [180], superconductors [181], antiferromagnets [182], and low-symmetry crystals [183–186].

Tunneling through magnetic insulators was first studied in the pioneering experiments of Ref. [187] and later in Refs. [100, 101]. When electrons tunnel through a

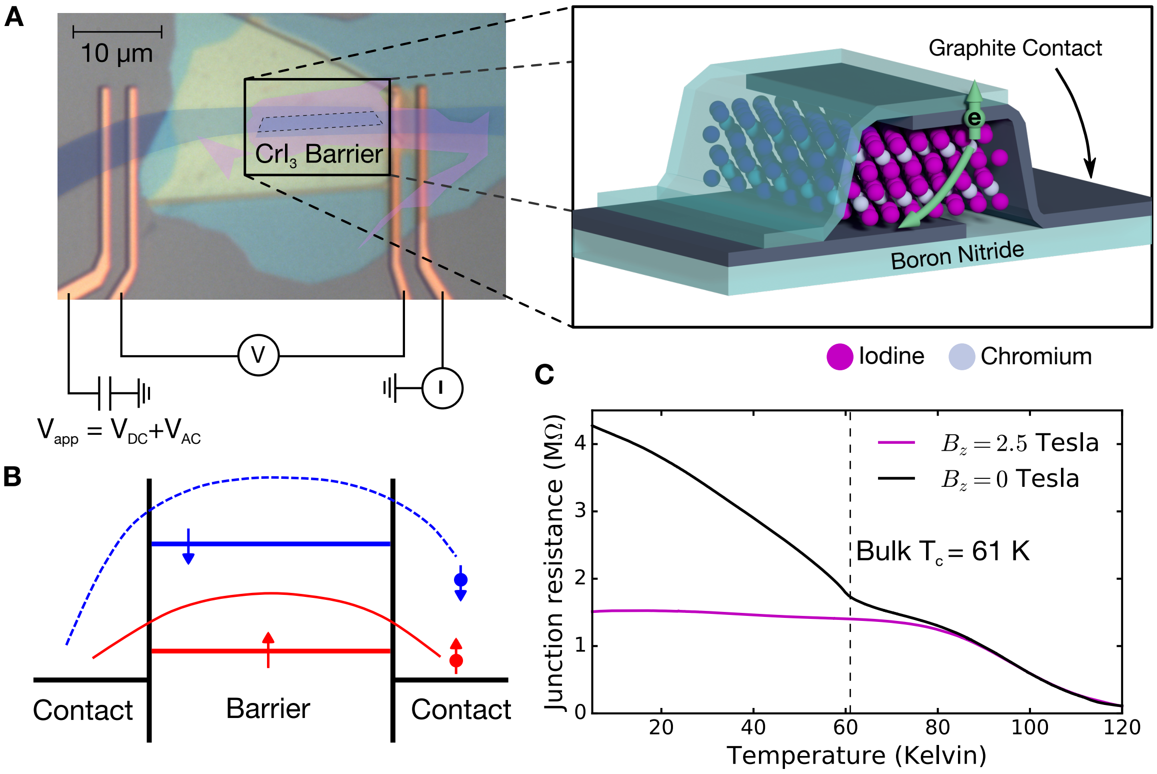

Figure 6-1: Experimental setup. **A.** Optical micrograph of a tetralayer CrI_3 tunnel junction device (device D1, false color). The dashed line encloses the tunnel junction area. The graphite contacts are themselves contacted by Au/Cr wires in a four-point geometry. Inset: Schematic of the van der Waals heterostructures studied in this work. Electrons tunnel between two graphite sheets separated by a magnetic CrI_3 tunnel barrier. The entire stack is encapsulated in hexagonal boron nitride. **B.** Schematic energy diagram of a metal/ferromagnetic insulator/metal junction. The red and blue lines in the barrier region represent the spin-up and spin-down energy barriers, respectively. The lower barrier for spin-up electrons leads to spin-polarized tunneling and reduced resistance for a ferromagnetic barrier. **C.** Zero-bias junction resistance versus temperature for device D1 cooled with (purple) and without (black) an applied magnetic field. The curves begin to deviate around the bulk Curie temperature (61 K), giving evidence for magnetic order in the CrI_3 barrier and for spin-polarized tunneling. The magnetic field was applied perpendicular to the CrI_3 layers.

ferromagnetic insulator, spin-up and spin-down electrons see different barrier heights (Fig. 6-1B). As a result, the tunneling rate can vary by orders of magnitude for electrons of opposite spins [100, 102], called the spin filter effect. The smaller gap for spin-up electrons tends to decrease the junction resistance as the barrier is cooled below its Curie temperature, T_C. The situation is more complicated for spatially textured magnetism. For example, the resistance of Ag/EuSe/Al tunnel junctions increases significantly when EuSe becomes antiferromagnetic [101]. However, the exponential dependence of the tunneling current on the barrier electronic structure generally provides a clear resistive signature of magnetism. We will use these effects to electrically detect the magnetic ground state and field-induced metamagnetic transition of few-layer CrI_3.

The resistance of a graphite/tetralayer CrI_3/graphite junction (device D1) as a function of temperature is shown in Fig. 6-1C. We measure the resistance in a four-point geometry using a 30 mV root-mean-square AC excitation (see Section 6.8.1). The temperature dependence was measured by cooling the sample down with (purple line) and without (black line) the application of an external magnetic field. The magnetic field is applied perpendicular to the layers, along the magnetic easy axis of CrI_3. Above 90 K, the resistance is independent of the applied field and shows Arrhenius behavior with a thermal activation gap of roughly 159 meV (Fig. 6-5). The resistance becomes field-dependent as the temperature approaches the bulk T_C of 61 K. When the sample is cooled in a 2.5 T magnetic field, the resistance plateaus below 80 K, signaling the onset of tunneling conductance [101, 187]. By contrast, when the sample is cooled without an external field, the resistance exhibits a kink near T_C and continues to increase below 60 K. The dependence of the tunneling resistance on magnetic field and temperature shows that the tunnel conductance is sensitive to the magnetization of the barrier.

6.3 Electrical detection of magnetic switching in few-layer CrI_3

To further investigate the magnetic phase diagram, we study the zero-bias conductance (500 µV AC excitation) of devices with two- to four-layer CrI_3 barriers as a function of applied magnetic field at low temperatures (300 mK to 4.2 K). We start with an analysis of a graphite/bilayer CrI_3/graphite junction (D2, Fig. 6-2A). For this device, the junction conductance increases almost twofold in a sharp step as the external field is increased above 0.85 T. The corresponding magnetoresistance is 95%, defined as

$$\mathrm{MR} = 100\% \times \frac{G_{\mathrm{HI}} - G_{\mathrm{LO}}}{G_{\mathrm{LO}}} \tag{6.1}$$

where G_{HI} is the high-field conductance maximum and G_{LO} is the low-field conductance minimum. No further steps are observed up to the largest fields studied (8 T; see Fig. 6-6). As the field is reduced from 2.4 T, the conductance decreases to its original zero-field value in a sharp step at 0.35 T. The well-defined steps and hysteretic field dependence demonstrate that the conductance changes originate from switching events of the magnetization. The tunneling current is most sensitive to the interlayer magnetization alignment, so the large steps we observe likely arise from vertical domains, *i.e.* regions where the magnetization points in different directions in different layers of $\mathrm{CrI_3}$.

Recently, magneto-optical Kerr effect (MOKE) data have revealed an antiferromagnetic state in bilayer $\mathrm{CrI_3}$ for fields below about 0.6 T [7]. In this state, the Cr moments order ferromagnetically within each layer but point in opposite directions in adjacent layers (Fig. 6-2B). The layers are fully aligned when the external magnetic field is increased above a critical value (Fig. 6-2C); *i.e.* it undergoes a metamagnetic transition to a ferromagnetic state. When the field is reduced, the magnetization spontaneously reverts to the antiparallel configuration. The switching behavior we observe in magnetoconductance reflects these previous MOKE data, confirming that the conductance change arises from the metamagnetic transition. We note, however, that little to no hysteresis was previously observed in the MOKE results for bilayer $\mathrm{CrI_3}$ [7], whereas we observe a clear hysteresis in the tunneling measurements. The reasons for this may be related to the lower temperature for these tunneling experiments as well as the fact that $\mathrm{CrI_3}$ remains closer to equilibrium (no photoexcitation).

We have also studied tunnel junctions with three- and four-layer $\mathrm{CrI_3}$ as the barrier. The zero-bias junction resistance of a graphite/4L $\mathrm{CrI_3}$/graphite junction (D3) is shown as a function of external magnetic field in Fig. 6-2D. The overall phenomenology is similar to that of junctions with a bilayer barrier, with well-defined steps and a

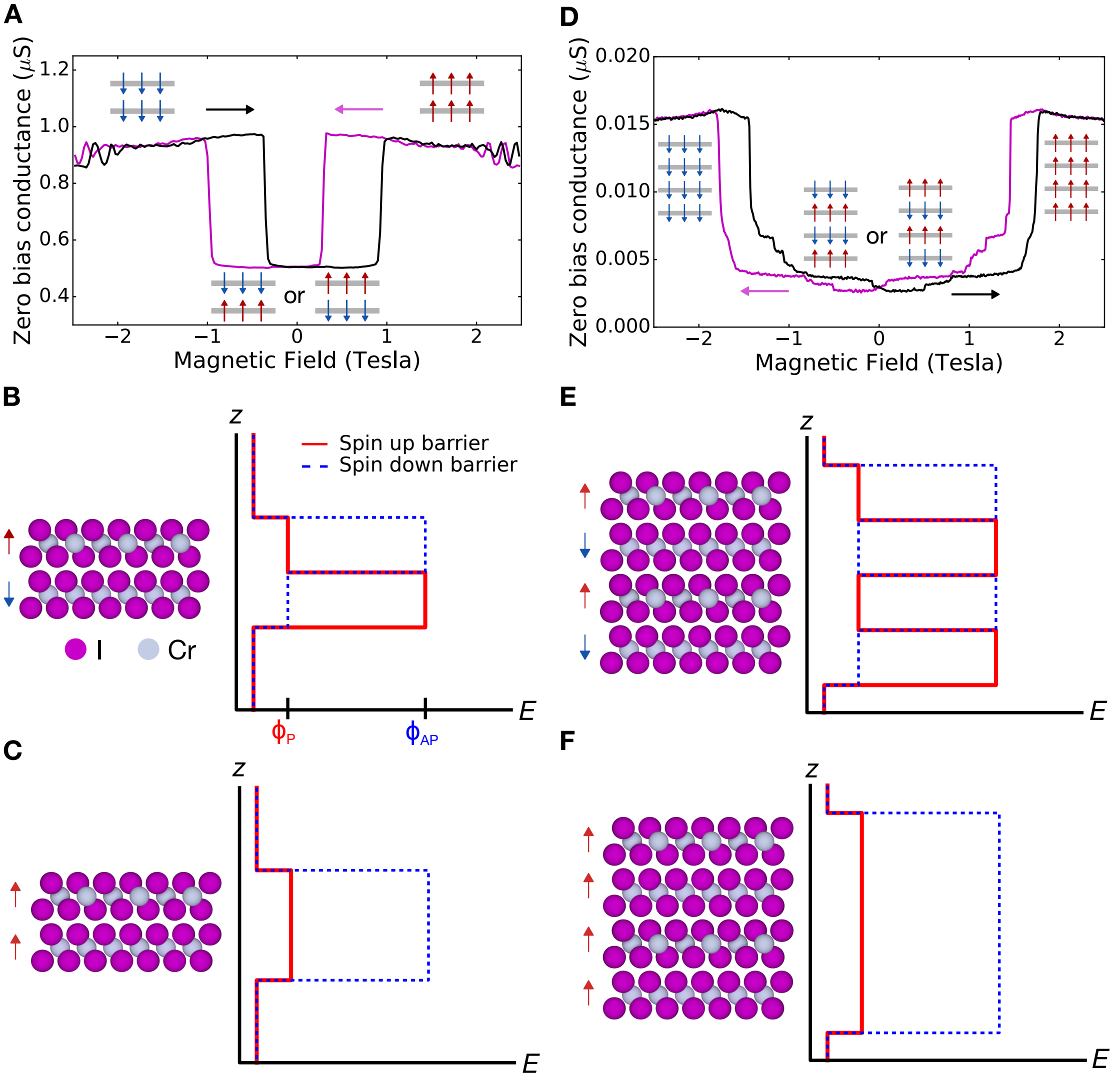

Figure 6-2: Magnetoconductance of few-layer $\mathrm{CrI_3}$. **A.** Conductance through a bilayer $\mathrm{CrI_3}$ tunnel barrier (device D2) as a function of an out-of-plane applied magnetic field with 500 µV AC excitation. The data were taken both for decreasing (purple line, left arrow) and increasing (black line, right arrow) magnetic field. The magnetoconductance traces are consistent with previous magnetometry data [7] for bilayer $\mathrm{CrI_3}$ showing that the two layers are antiparallel at zero field but can be aligned with an external field below 1 T. **B,C.** Schematic of barriers experienced by spin-up and spin-down electrons tunneling through bilayer $\mathrm{CrI_3}$ in the low-field (**B**) and high-field (**C**) states. In the low-field state, the two layers are antiparallel, and both spins see a high barrier. In the high-field state, the layers are aligned and up spins see a low-energy barrier, leading to increased conductance. **D-F.** Analogous data and schematics for a tetralayer $\mathrm{CrI_3}$ barrier device (device D3). In both cases, the sample temperature was 300 mK.

total magnetoresistance of 550%. In addition to the large jump around 1.8 T, we see multiple smaller steps that may correspond to lateral domains within the junction. This is consistent with a lateral domain size on the order of 2 µm observed in previous optical studies [7, 19]. The behavior of our trilayer junctions is again similar, with magnetoresistances up to 300% (Fig. 6-7). On the basis of these results, we hypothesize that few-layer CrI_3 is antiferromagnetic without an external magnetic field (Fig. 6-2E). Such behavior is consistent with magneto-optical data for bilayer CrI_3 [7], but those MOKE data suggested a ferromagnetic configuration for thicker crystals (*e.g.* 3L CrI_3). Nevertheless, our data strongly support an antiparallel alignment between layers extending over most of the junction area. Once more, the different temperatures and absence of photoexcitation may be responsible for the different behavior observed.

6.4 Spin filter model for magnetoresistance in CrI_3

To understand the large magnetoresistance and its thickness dependence, we analyze a spin filter model [102] for transmission through a CrI_3 barrier. The model treats each crystal layer of CrI_3 as an independent tunnel barrier, with a transmission coefficient of T_{P} and T_{AP} for spins parallel and antiparallel to the local spin direction, respectively. Ignoring multiple reflections and quantum interference effects, the transmission through the entire crystal is then a product of the transmission coefficients for each layer. For example, for a CrI_3 bilayer in the high-field magnetization configuration (Fig. 6-2C), spin-up electrons have a transmission probability ${T_{\mathrm{P}}}^2$ whereas spin-down electrons have transition probability ${T_{\mathrm{AP}}}^2$. The high-field conductance is $G_{\mathrm{HI}} \propto {T_{\mathrm{P}}}^2 + {T_{\mathrm{AP}}}^2$. Similarly, for the low-field configuration with antiparallel magnetizations (Fig. 6-2B), the conductance is $G_{\mathrm{LO}} \propto 2T_{\mathrm{P}}T_{\mathrm{AP}}$. The ratio of high-field to low-field conductances is then $G_{\mathrm{HI}}/G_{\mathrm{LO}} = ({T_{\mathrm{P}}}^2+{T_{\mathrm{AP}}}^2)/2T_{\mathrm{P}}T_{\mathrm{AP}} \approx T_{\mathrm{P}}/2T_{\mathrm{AP}}$. We have carried out similar calculations for $N = 3$- and 4-layer CrI_3 barriers, summarized in Section 6.8.4. In Fig. 6-3A, we plot the measured magnetoresistance (black circles) as a function of N, along with a one-parameter fit to the spin filter model (purple stars). The model reproduces the overall experimental trend with a best-fit value of $T_{\mathrm{P}}/T_{\mathrm{AP}} = 3.5$. For a summary of all measured devices, see Table 6.8.10.

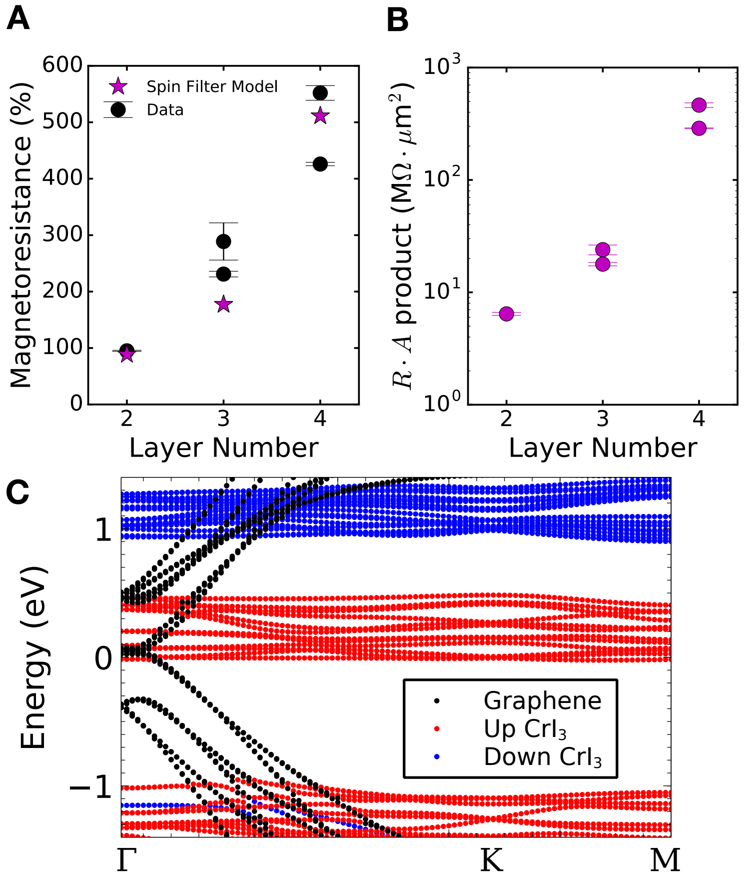

Figure 6-3: Origin of magnetoresistance in $\mathrm{CrI_3}$. **A.** Magnetoresistance ratio (black circles) versus $\mathrm{CrI_3}$ layer number for multiple devices at 300 mK. We also plot a fit to the spin filter model (purple stars). The only fitting parameter, $T_{\mathrm{P}}/T_{\mathrm{AP}} = 3.5$, gives the ratio of spin-up to spin-down transmission through a $\mathrm{CrI_3}$ monolayer. **B.** Resistance-area product versus $\mathrm{CrI_3}$ layer number for multiple devices. The resistances are measured in the fully aligned magnetic configuration and were taken at zero bias. **C.** Electronic structure of a trilayer graphite/trilayer $\mathrm{CrI_3}$ heterostructure calculated with density functional theory. $\mathrm{CrI_3}$ is in the fully ferromagnetic configuration, and its bands are projected on the spin-up and spin-down channels. Although the minority spins do not show states close to the Fermi energy, there are a large number of states in the majority channel. The difference establishes a microscopic basis for the large $T_{\mathrm{P}}/T_{\mathrm{AP}}$ that we observe.

We can also estimate the spin polarization of the current within the spin filter model. When $\mathrm{CrI_3}$ is fully polarized, the transmission probability of up and down spins through an N-layer $\mathrm{CrI_3}$ barrier is ${T_{\mathrm{P}}}^N$ and ${T_{\mathrm{AP}}}^N$, respectively. Therefore, the ratio of spin-up to spin-down conductance is approximately $G_\uparrow/G_\downarrow = (T_\mathrm{P}/T_\mathrm{AP})^N$. From $T_\mathrm{P}/T_\mathrm{AP} \approx 3.5$, we estimate a spin polarization of $(G_\uparrow - G_\downarrow)/(G_\uparrow + G_\downarrow) \approx 85$, 95, and 99% for $N = 2$, 3, and 4, respectively. These values are comparable to the largest values obtained with EuSe and EuS magnetic insulator barriers [101, 104], so that $\mathrm{CrI_3}$ tunnel barriers can enable future spin-sensitive transport devices.

In the spin filter approximation, the calculation of the magnetoresistance is reduced to a calculation of $T_\mathrm{P}/T_\mathrm{AP}$, related to the different barrier heights for spin-up and spin-down electrons. To investigate the barrier heights, we carried out density functional theory (DFT) calculations for three layers of $\mathrm{CrI_3}$ and three layers of graphite (see Section 6.8.1). Calculations portray $\mathrm{CrI_3}$ as a ferromagnetic insulator with magnetic moments localized on the chromium atoms and spin-split energy bands (Fig. 6-3C). Notably, when the magnetization of the three layers is aligned, we find that spin-up bands of $\mathrm{CrI_3}$ lie very close to the graphite Fermi energy, whereas the nearest spin-down bands are much higher in energy (>1 eV). Therefore, the transparency of the barrier has to be much smaller for spin-down electrons and provides a microscopic foundation for the large $T_\mathrm{P}/T_\mathrm{AP}$. Note that even though the DFT calculations show a $\mathrm{CrI_3}$ majority band very close to or crossing the graphite Fermi energy, the exponential thickness dependence of the junction resistance (Fig. 6-3B) shows that our junctions are in the tunneling-dominated regime with a finite barrier height. Further transport calculations should elucidate the precise tunneling pathways in $\mathrm{CrI_3}$/graphite junctions leading to finite energy barriers with chromium $3d$ orbital bands very close to the Fermi level.

6.5 Inelastic electron tunneling spectroscopy

In addition to the zero-bias conductance, we measured the differential conductance dI/dV as a function of the applied DC offset V_DC. The dI/dV versus V_DC traces reveal a rich spectrum, whose most prominent features are a series of step-like increases, symmetric in bias, below 25 meV (Figs. 6-4 and 6-8). These steps are characteristic of inelastic electron tunneling where electrons lose energy to collective excitations of the barrier or electrodes. When the tunneling energy (eV_{DC}) exceeds the collective excitation energy, the introduction of these additional tunneling pathways results in steps in the dI/dV versus V_{DC} trace. The energies of phonons [105, 107, 188] and magnons [106, 189–191] can therefore be measured as peaks (dips) in d^2I/dV^2 versus V_{DC} for positive (negative) V_{DC}. The bottom panel of Fig. 6-4A shows $|d^2I/dV^2|$ obtained by numerical differentiation of the dI/dV data for a bilayer $\mathrm{CrI_3}$ barrier device (D2). The inelastic tunneling spectrum (IETS) reveals three peaks at 3, 7, and 17 meV. These features were visible in every $\mathrm{CrI_3}$ tunneling device that we measured. Past IETS data on graphite/boron nitride/graphite heterostructures in a geometry similar to that of our junctions [107] do not contain any inelastic contributions from graphite phonons below 17 meV. Earlier scanning tunneling studies of graphite surfaces similarly find an onset of prominent graphite inelastic peaks at 16 meV [188]. Thus, the inner two peaks must arise from $\mathrm{CrI_3}$ phonons or magnons. The inelastic features start forming just below the onset of magnetism (Fig. 6-9), suggesting a magnon excitation origin.

Another signature of magnon-assisted tunneling is the stiffening of the magnon modes as an external magnetic field is applied [189,190]. A single magnon corresponds to a delocalized spin-flip ($|S_z| = 1$) within the $\mathrm{CrI_3}$ barrier, which carries a magnetic moment of approximately $2\mu_{\mathrm{B}}$ (where μ_{B} is the Bohr magneton) antiparallel to the external magnetic field. Therefore, magnon IETS peaks should blueshift at 0.12 meV/T by the Zeeman effect. Figure 6-4B shows $|d^2I/dV^2|$ as a function of both applied magnetic field and bias voltage. Even to the eye, a strong linear increase of all three IETS peaks is visible. In Fig. 6-4C, we plot the peak energies (determined by Gaussian fits) of the innermost peaks versus magnetic field. We also plot the expected energy shift $2\mu_{\mathrm{B}}B$ due to the Zeeman effect (dashed gray line). This line roughly fits the magnetic field dependence of the 3 meV peak, but the 7 meV peak clearly has much higher dispersion corresponding to $8\mu_{\mathrm{B}}$. The latter effect might be caused by magnon renormalization effects, as discussed below.

To model the magnon spectrum, we write an effective spin Hamiltonian for $\mathrm{CrI_3}$ [75] that includes nearest- and next-nearest–neighbor exchange, together with an easy

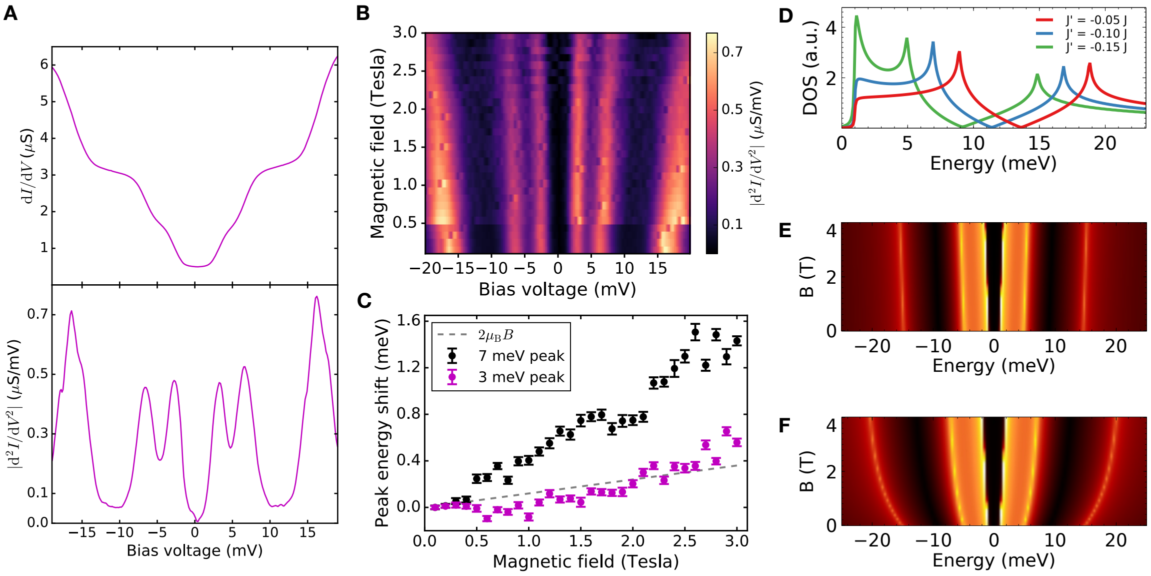

Figure 6-4: Inelastic tunneling spectroscopy. **A.** Top panel: Differential conductance versus a DC bias voltage for a bilayer CrI_3 barrier device (D2) at zero applied magnetic field. The AC excitation was 200 μV and the temperature was 300 mK. Bottom panel: Absolute value of d^2I/dV^2 versus a DC bias voltage, obtained via numerical differentiation of the data in the top panel. According to the theory of inelastic tunneling spectroscopy, the peaks in d^2I/dV^2 correspond to phonon or magnon excitations of the barrier or electrodes. **B.** $|d^2I/dV^2|$ (color scale at right) versus applied magnetic field and DC bias voltage. All three inelastic peaks increase in energy as the applied field is increased. **C.** Energy of the two lowest-energy inelastic peaks versus applied magnetic field. The zero-field energy is subtracted from both peaks for clarity. The peak locations were determined by Gaussian fits to the data. The error bars represent estimated standard deviations calculated from the least-squares fitting procedure. The dashed gray line shows the Zeeman energy shift of a $2\mu_B$ magnetic moment (0.12 meV/T), which roughly matches the evolution of the 3 meV peak. **D.** Calculated magnon density of states (DOS) for CrI_3. The details of the calculations are described in Section 6.8.7. **E.** Calculated dispersion of magnons with applied magnetic field at zero temperature. **F.** Calculated renormalized magnon dispersion with magnetic field at finite temperature ($T = 0.033J$, where J is the nearest-neighbor exchange).

axis anisotropy term (see Section 6.8.7 for details). Using this model, we find that the calculated magnon density of states (Fig. 6-4D) can qualitatively reproduce the experimental inelastic spectrum. We used a nearest-neighbor exchange parameter consistent with previous first principles calculations and experiment [75, 86, 192] and chose the next-nearest–neighbor value to match our data (see Section 6.8.7). At zero temperature, the magnon energies are still expected to blueshift at 0.12 meV/T in an applied magnetic field (Fig. 6-4E). However, at finite temperature and $B = 0$, thermally excited magnons deplete the magnetization, resulting in an effective reduction of the spin stiffness and a redshift of the magnon spectrum with respect to the case without thermal renormalization of the exchange constants. Application of a magnetic field increases the spin wave gap, decreasing the population of thermal spin waves and increasing the spin stiffness. This renormalizes the effective magnon hopping parameters, leading to a shift of the spin wave spectrum that adds to the Zeeman term and results in a nonlinear field dependence (Fig. 6-4F and Section 6.8.7).

6.6 Conclusion

Our devices are an example of a "double spin filter" where a magnetic tunnel barrier with decoupled magnetic layers is used as a magnetic memory bit [102]. We overcome the limitations of previous double spin filters [104] owing to the unique decoupling of magnetic layers across the atomic-scale van der Waals gap. This decoupling provides electrical readout of the CrI_3 magnetization state without additional ferromagnetic sensor layers, enabling facile detection of spin-orbit torques on layered magnetic insulators. Further exploration is required to understand the electron-magnon coupling in these devices and to potentially study bosonic topological matter in honeycomb ferromagnets [193, 194].

6.7 Epilogue

This paper was published alongside a similar paper on CrI_3 magnetic tunnel junctions [111]. Here, the authors also fabricate graphite/CrI_3/graphite heterostructures and probe the tunneling response. In contrast to our work, they focus on applying higher bias voltages (200-400 meV). Under these conditions, they observe extremely large magnetoresistances, reaching 19,000% magnetoresistance in a fully-polarized tetralayer CrI_3 device with the application of a 9 T in-plane magnetic field and a bias voltage around 250 meV. These results further demonstrate the potential for incorporating van der Waals magnetic tunnel junctions in spintronics applications.

Furthermore, there have been subsequent IETS experiments in the low-bias regime (0-20 meV) of $CrBr_3$ [116] and of all three CrX_3 [115] magnetic tunnel junctions. In the first paper, the authors find two inelastic features that disperse with magnetic field, suggestive of magnon-assisted tunneling in $CrBr_3$ devices in analogy to our findings in CrI_3 devices in Section 6.5. They also observe enhanced dispersion in both peaks of approximately $5\mu_B$ (in contrast to the expected value of $2\mu_B$). However, in the second paper, the authors find that the magnon mode dispersions in all three CrX_3 devices have the expected slope of $2\mu_B$. Moreover, in their CrI_3 IETS spectrum, they observe the 7 meV and 16 meV peaks but do not detect the additional dispersive mode at 3 meV that we have observed in our devices. Further investigation is needed to fully understand how magnon-magnon interactions renormalize the magnon spectra in the magnetic honeycomb lattices of CrX_3 and account for these differences.

6.8 Supplemental Information

6.8.1 Methods

Our fabrication starts with preparation of Au/Cr wires and bond pads on a 295 nm SiO_2/Si wafer. The Au is 33 nm thick and the Cr is 2 nm thick. The wires are prepared by electron beam lithography using bilayer PMMA resist and lift-off processing. The chip with wires is fixed to a ceramic chip carrier using silver paint and wire bonded to the carrier. This assembly is loaded into a glovebox for further processing (in which we transfer the heterostructure onto the wires, described below).

The van der Waals assembly of the graphite/CrI_3/graphite heterostructure was carried out in an inert argon environment (H_2O and O_2 < 0.1 ppm). The stack was prepared by sequentially picking up each crystal (top boron nitride, top graphite, CrI_3, bottom graphite, and finally bottom boron nitride) from SiO_2/Si substrates. We used a stamp-based dry transfer technique similar to those reported elsewhere [31].

For our stamp, we used a poly(bisphenol A carbonate) film stretched over a piece of polydimethylsiloxane.

After the heterostructure was assembled on the stamp, the assembly was pressed onto the Au/Cr wires so that two wires contacted each of the graphite fingers. The heterostructure was released by heating to 170°C. Finally, a glass coverslip was attached to the top of the chip carrier using Crystalbond in order to hermetically seal the device (see Appendix B for details).

Following fabrication, the device was loaded into a helium-3 cryostat. Conductance measurements were carried out using standard low frequency lock-in techniques (the excitation frequency was always < 20 Hz). We verified our results using DC measurements where a DC bias was applied to the sample and the resulting DC current was measured with a current preamplifier. For all conductance measurements, unless noted otherwise, the sample temperature was held at either 300 mK or 4.2 K, without strong temperature dependence in this range.

Density functional theory calculations were performed with Quantum Espresso [195] using PAW pseudopotentials and GGA exchange correlation functional. We used a geometry consisting of three layers of CrI_3 and three layers of graphite, consisting of a 3 by 3 unit cell of graphite with periodic boundary conditions in the z direction and ABC stacking. Structural relaxations were performed with spin polarization. Band structure calculations show that the majority CrI_3 bands are located close to the charge neutrality point of graphite, and we expect a very small charge transfer from graphite to CrI_3. Minority spin bands reside in the gap of CrI_3, and are located 1 eV away from minority t_{2g} bands of CrI_3. We also computed heterostructures made of monolayer graphene on top of monolayer CrI_3 and monolayer graphene on top of bilayer CrI_3. In all instances the charge neutrality point is located in the majority CrI_3 bands.

6.8.2 Thermally activated transport in CrI_3 tunnel junctions

Figure 6-5 shows the tunnel conductance for a tetralayer CrI_3 barrier (device D1) as a function of inverse temperature above the magnetic transition, plotted on a semilogarithmic scale. The AC excitation voltage is 5 mV. At higher temperatures the order of magnitude changes linearly with $1/T$, indicating thermally activated transport. The thermal activation gap Δ is calculated by a fit to:

$$\frac{dI}{dV} = Ce^{-\frac{\Delta}{2k_\mathrm{B}T}} \tag{6.2}$$

where C is a constant and k_B is the Boltzmann constant. Our fit gives a value of approximately 158 meV for this junction, consistent with data from other devices.

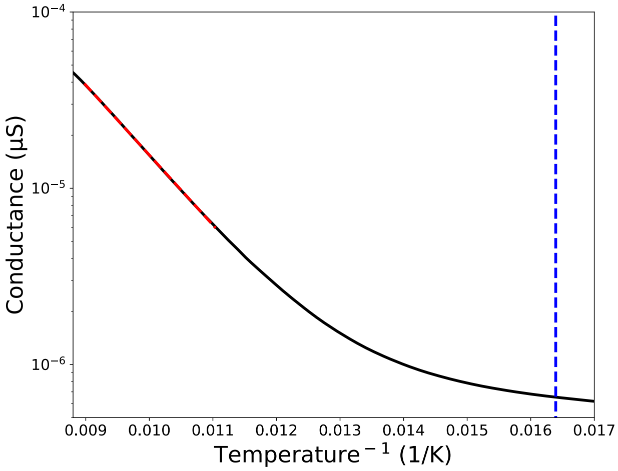

Figure 6-5: Arrhenius plot of zero bias junction conductance vs. inverse temperature for a graphite/tetralayer CrI_3/graphite junction (device D1) cooled with 5 mV AC excitation and without an applied magnetic field. The red line indicates the linear fit used to extract the thermal activation gap above the metamagnetic transition. The bulk Curie temperature (61 K) is shown with the blue dashed line.

6.8.3 Transport through CrI_3 barriers in high magnetic fields

In Figure 6-6A, we show the zero bias conductance of a graphite/bilayer CrI_3/graphite junction (device D2) up to 8 Tesla with an AC excitation of 200 μV. There is a single sharp step in conductance when the external field is increased beyond 0.85 T. At this transition, the junction conductance increases by a factor of about 1.9. There are no steps in the conductance above this transition, consistent with previous magnetization data for bilayer CrI_3. We have not observed switching events above 2 T for CrI_3

barriers of any thickness. For this device, we detect the onset of Shubnikov-de Haas oscillations above 2 T from the thin graphite contacts. Surprisingly, the zero bias conductance drops to zero as the field is increased. We have further explored this feature as a function of the DC bias and magnetic field, finding that it corresponds to a gap-like feature that opens at high field (Fig. 6-6B). The origin of this behavior is not presently understood.

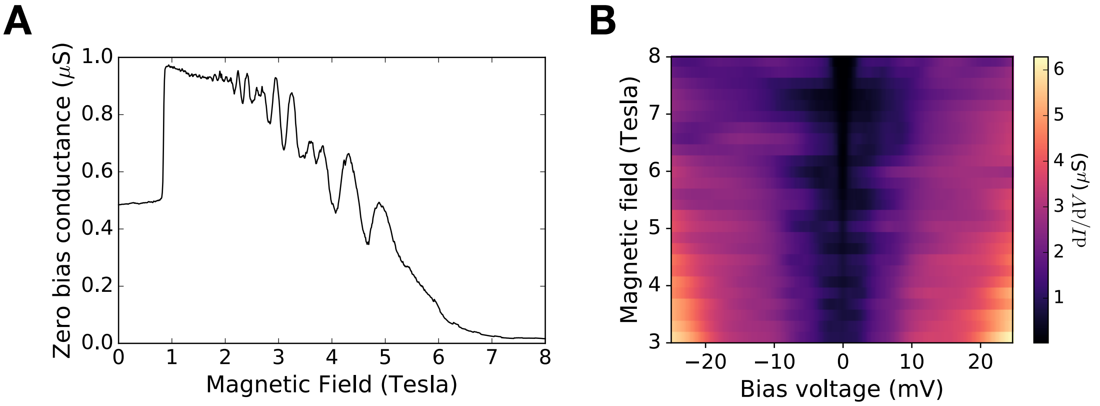

Figure 6-6: **A.** Conductance through a bilayer $\mathrm{CrI_3}$ tunnel barrier (device D2) as a function of an out-of-plane applied magnetic field with 200 μV AC excitation at 300 mK. The external field is swept up from zero. Beyond 2 Tesla, we observe Shubnikov-de Haas oscillations in conductance due to the graphite contacts in the device. **B.** Differential conductance as a function of DC bias and applied magnetic field with 200 μV AC excitation at 300 mK. In addition to the linearly dispersing inelastic features, Shubnikov-de Haas and a pronounced gap opening at high field are visible.

6.8.4 Magnetoresistance models for trilayer and tetralayer $\mathrm{CrI_3}$ barriers

For a trilayer barrier, the total conductance in the aligned configuration is ${T_\mathrm{P}}^3 + {T_\mathrm{AP}}^3$, whereas the conductance in the antiparallel configuration is $T_\mathrm{P} T_\mathrm{AP} T_\mathrm{P} + T_\mathrm{AP} T_\mathrm{P} T_\mathrm{AP}$. The ratio of high field to low field conductance is:

$$\frac{G_\mathrm{HI}}{G_\mathrm{LO}} = \frac{{T_\mathrm{P}}^3 + {T_\mathrm{AP}}^3}{{T_\mathrm{P}}^2 T_\mathrm{AP} + {T_\mathrm{AP}}^2 T_\mathrm{P}} \tag{6.3}$$

Based on a similar calculation, we can calculate the equivalent ratio for a four layer $\mathrm{CrI_3}$ barrier:

$$\frac{G_{\mathrm{HI}}}{G_{\mathrm{LO}}} = \frac{{T_{\mathrm{P}}}^{4} + {T_{\mathrm{AP}}}^{4}}{2{T_{\mathrm{P}}}^{2}{T_{\mathrm{AP}}}^{2}} \tag{6.4}$$

We use Eq. 6.3 and 6.4, together with the formula for bilayer $\mathrm{CrI_3}$ given in Section 6.4, to produce the spin filter model fits shown in Fig. 6-3A . Note that the above ratios depend only on $T_{\mathrm{P}}/T_{\mathrm{AP}}$.

6.8.5 Conductance versus magnetic field for trilayer $\mathrm{CrI_3}$ barriers

In Figure 6-7 we plot the conductance of graphite/$\mathrm{CrI_3}$/graphite junction with a trilayer $\mathrm{CrI_3}$ barrier (device D4) as a function of magnetic field at a temperature of 4.2 K. The AC excitation voltage was 300 µV. The purple and black lines indicate increasing and decreasing direction of the magnetic field sweep, respectively. Shubnikov-de Hass oscillations onset around 2 T from the few-layer graphite contacts.

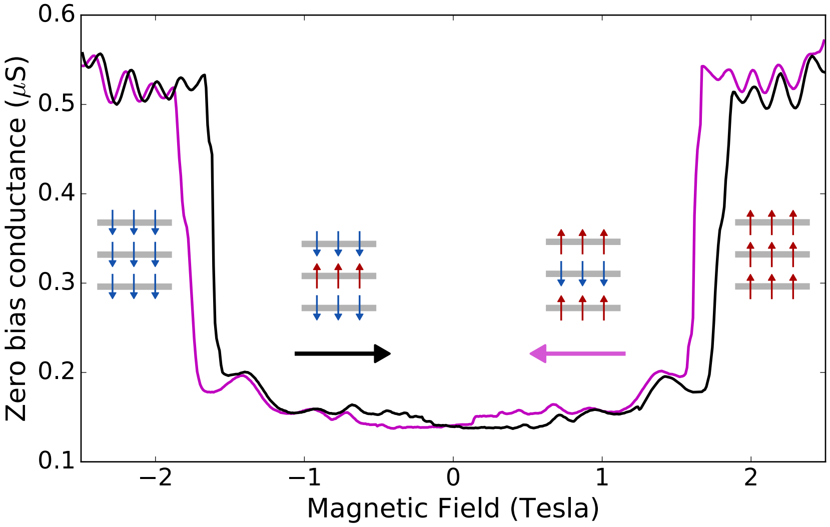

Figure 6-7: Magnetic field dependence of the junction conductance for a graphite/$\mathrm{CrI_3}$/graphite junction with a trilayer $\mathrm{CrI_3}$ barrier (device D4), with a 300 µV AC excitation voltage at 4.2 K.

6.8.6 Tunneling measurements at large applied bias

Section 6.5 reports dI/dV and d^2I/dV^2 data as a function of the applied DC bias V_{DC}. We showed data for a bilayer $\mathrm{CrI_3}$ tunnel barrier and for applied bias below 25 mV. We have also measured dI/dV versus V_{DC} for multiple devices and for generator voltages up to 300 mV. This dataset reveals a broader spectrum of inelastic features and the onset of Fowler-Nordheim tunneling around 200 mV.

Figure 6-8A shows dI/dV (top panel) and d^2I/dV^2 (bottom panel) for a tetralayer $\mathrm{CrI_3}$ barrier (device D1). The AC excitation was 1 mV and the temperature was 4.2 K. The prominent low bias inelastic features discussed in Sec. 6.5 are visible, along with additional features at higher bias. We have indicated the energies of graphite phonons commonly observed in inelastic tunneling experiments [107, 188] as grey dashed lines. Many of the graphite phonon lines are accompanied by apparent features in $|d^2I/dV^2|$, although the 3 meV, 7 meV, and 16 meV peaks are far more prominent. (Note that the 16 meV peak in fact coincides with the Γ point ZA phonon of graphite.) There also appears to be a rapid increase in the conductance around 200 meV, which we investigate by pushing to higher DC bias voltages across another $\mathrm{CrI_3}$ barrier.

Figure 6-8B shows the DC current (calculated from the integrated dI/dV) as a function of the DC voltage for a trilayer $\mathrm{CrI_3}$ barrier (device D5, black line) at 4.2 K and with an applied magnetic field of 2.5 T. The tunneling current can be estimated using Simmons' model [97]:

$$I(V_{\mathrm{DC}}) \propto \int_0^{eV_{\mathrm{DC}}} dE\,E\,T(E) + eV_{\mathrm{DC}} \int_{eV_{\mathrm{DC}}}^{E_{\mathrm{F}}} dE\,T(E) \tag{6.5}$$

where $T(E)$ is the transmission probability as a function of energy below the Fermi level, E_{F}. For large DC biases, above a few tens of meV in our parameter range, the second term becomes negligible (and exactly zero for $V_{\mathrm{DC}} > E_{\mathrm{F}}/e$). We therefore ignore this term in our fits. We can estimate the transmission probability in the WKB

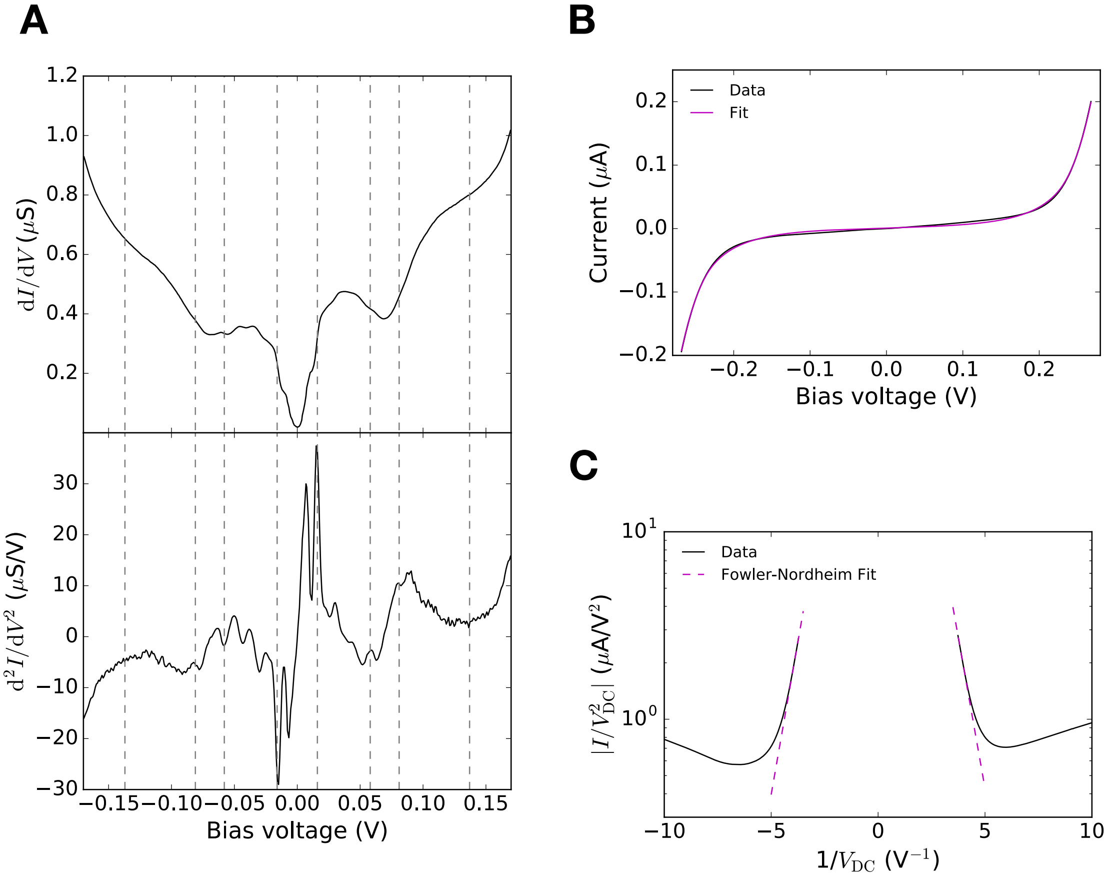

Figure 6-8: **A.** Top panel: Differential conductance through a tetralayer $\mathrm{CrI_3}$ tunnel barrier (device D1) as a function of DC bias in the absence of an applied magnetic field. The temperature was 4.2 K and the AC excitation was 1 mV. Bottom panel: d^2I/dV^2 as a function of DC bias calculated as the numerical derivative of the data in top panel. The grey lines indicate the energies of graphite phonons that have been observed in previous inelastic tunneling experiments. **B.** Current versus DC bias (black line) for a trilayer $\mathrm{CrI_3}$ tunnel barrier (device D5) at 4.2 K and 2.5 T magnetic field. The purple line is a fit to Eq. 6.7. **C.** $|I/{V_{\mathrm{DC}}}^2|$ versus $1/V_{\mathrm{DC}}$ on a semilog scale (black line). The data are the same as **B**, but over a restricted bias range. The dashed purple lines are fits of the high bias data to the Fowler-Nordheim formula (Eq. 6.7).

approximation:

$$T(E) = \left| \exp\left(-\frac{2\sqrt{2m_*}}{\hbar} \int_0^d dx \sqrt{\Phi - \frac{eV_{\mathrm{DC}}x}{d} + E} \right) \right| \tag{6.6}$$

where m_* is the effective mass of the barrier, Φ is the barrier height, $\hbar$ is the reduced

Planck constant, e is the elementary charge, and d is barrier thickness. The purple line in Fig. 6-8B is a fit of the measured $I(V)$ curve to Eq. 6.5 (without the second term) giving $m_* = 1.8$ electron masses and $\Phi = 0.2$ eV, both reasonable values.

As a consistency check, we can also fit the data to the usual Fowler-Nordheim equation [97] strictly valid only for $eV_{\mathrm{DC}} > \Phi$:

$$\frac{I}{{V_{\mathrm{DC}}}^2} = C \exp\left(-\frac{4d\sqrt{2m_*\Phi^3}}{3\hbar e}\frac{1}{V_{\mathrm{DC}}}\right) \tag{6.7}$$

where C is a constant. Figure 6-8C shows $|I/{V_{\mathrm{DC}}}^2|$ versus $1/V_{\mathrm{DC}}$ on a semilog scale (the x axis has been restricted to emphasize the high bias behavior). For $V_{\mathrm{DC}} > \Phi$ the plot shows the expected linear trend. Linear fits (dashed purple lines) give $4d\sqrt{2m_*\Phi^3}/3\hbar e \approx 1.5$ V, whereas the previously determined effective mass and barrier height gives 1.9 V.

6.8.7 Derivation of the magnon density of states for monolayer CrI$_3$

In the following we derive an effective Hamiltonian for the spin waves in these systems. We start with a Heisenberg Hamiltonian in the honeycomb lattice for the Cr^{3+} ions:

$$\mathcal{H} = -J\sum_{<ij>} \vec{S}_i \cdot \vec{S}_j - J' \sum_{\ll ij \gg} \vec{S}_i \cdot \vec{S}_j - K \sum_{<ij>} S_i^z S_j^z + B_z \sum_i S_i^z \tag{6.8}$$

where J is the exchange between nearest neighbors, J' is the exchange between next-nearest neighbors, K is the anisotropic exchange, $< >$ denotes the sum over nearest neighbors, and $\ll \gg$ denotes the sum over next-nearest neighbors. We take J, $K > 0$ and $J > K$. This results in a ferromagnetic ground state with easy axis anisotropy along the z axis. Finally, the term J' controls the location of the peaks of the magnon spectra. We take $K = 0.13J$ (Fig. 6-4D-F) and $J' = -0.15J$ (Fig. 6-4D,E). For J we use two different values, depending on the level of approximation used to compute magnon properties. In Fig. 6-4D and 6-4E, where nonlinear magnon renormalization effects are ignored, we take $J = 3.3$ meV. In Fig. 6-4F, where we compute magnon density of states using the nonlinear theory outlined below, we take $J = 4.5$ meV.

The magnon spectra of the previous Hamiltonian is obtained by a Holstein-Primakoff transformation, which to second order in bosonic b_i reads:

$$S_i^+ \approx \sqrt{2S}\left(1 - \frac{b_i^\dagger b_i}{4S}\right) b_i \tag{6.9a}$$

$$S_i^- \approx \sqrt{2S} b_i^\dagger \left(1 - \frac{b_i^\dagger b_i}{4S}\right) \tag{6.9b}$$

$$S_i^z = S - b_i^\dagger b_i \tag{6.9c}$$

Substituting the previous formulas in the Heisenberg Hamiltonian we obtain an interacting bosonic Hamiltonian of the form:

$$\mathcal{H} = B_z \sum_i b_i^\dagger b_i - \sum_{ij} (t_{ij} b_i^\dagger b_j + u_{ij} b_i^\dagger b_j b_i^\dagger b_j + v_{ij} b_i^\dagger b_i b_j^\dagger b_j) \tag{6.10}$$

where t_{ij}, u_{ij}, and v_{ij} are functions of J, J', and K. The previous Hamiltonian has four field operators so it cannot generically be solved analytically. The Hamiltonian can be made quadratic with the mean field ansatz:

$$b_i^\dagger b_j b_i^\dagger b_j \approx 2\langle b_i^\dagger b_j \rangle b_i^\dagger b_j + \langle b_i^\dagger b_i \rangle b_j^\dagger b_j + \langle b_j^\dagger b_j \rangle b_i^\dagger b_i \tag{6.11}$$

where we calculate the occupation numbers of the normal modes b_k at low temperature as:

$$\langle b_k^\dagger b_k \rangle = \frac{1}{e^{\beta(\Delta + \rho k^2)} - 1} \approx e^{-\beta(\Delta + \rho k^2)} \tag{6.12}$$

Approximating $\langle b_i^\dagger b_j \rangle \approx \langle b_i^\dagger b_i \rangle$, we can express the effective magnon hopping in the low temperature limit as:

$$t_{ij}(B_z) = t_{ij}(\infty)\left(1 - C_3 e^{-\beta |B_z|}\right) \tag{6.13}$$

where C_3 is the prefactor obtained when performing theintegration over k-space necessary to compute $\langle b_i^\dagger b_i \rangle$. Eq. 6.13 permits us to write the effective mean field spin wave Hamiltonian:

$$\mathcal{H}_{\mathrm{MF}} = -\sum_{ij} t_{ij}(B_z) b_i^\dagger b_j + B_z \sum_i b_i^\dagger b_i \tag{6.14}$$

This shows that the effect of the out-of-plane magnetic field is to renormalize the effective magnon hopping, and in particular the effective g-factor. The spectrum of the previous Hamiltonian yields the field-dependent magnon density of states:

$$D(E) = \int \delta\left(E - \varepsilon(\vec{k})\right) d^2\vec{k} \tag{6.15}$$

where $\varepsilon(\vec{k})$ are the eigenvalues of the magnonic Bloch Hamiltonian. In general, the spectrum shows three peaks: two peaks that can be related to the van Hove singularities of the honeycomb lattice, and a third low energy peak controlled by the next-nearest neighbor exchange. We note that although the next-nearest neighbor exchange is antiferromagnetic, the combination of nearest neighbor exchange and anisotropic exchange will impose a ferromagnetic ground state for small values of the next-nearest neighbor exchange. The exchange constants of the parent Heisenberg Hamiltonian were chosen so that the spin wave peaks at located at the energies found in the experiment.

Intuitively, the external magnetic field increases the spin wave gap, decreasing the population of thermally excited spin waves and thus modifying the effective exchange coupling in a mean field picture. This field dependent renormalization of the exchange constants J, J', and K adds to the conventional Zeeman shift, yielding a nonlinear field evolution of the peaks. The position of the 3 meV peak (Fig. 6-4) is determined by only anisotropic exchange renormalization whereas the 7 meV peak is determined by the additive contributions both isotropic and anisotropic exchange renormalization. Thus, the nonlinear effects will be more pronounced for the 7 meV peak.

6.8.8 Temperature dependence of the inelastic tunneling features

We measured the differential conductance as a function of both temperature and applied bias for a tetralayer $\mathrm{CrI_3}$ barrier junction (device D3). This was done by heating the sample to about 65 K, and letting it cool slowly while sweeping the DC offset voltage back and forth. The temperature decrease during the voltage sweep was always less than 2 K. We applied a magnetic field of 1.8 T during the measurements to keep the sample in the fully aligned magnetic configuration. This makes the data easier to interpret and collect since the conductance has a strong temperature dependence in the antiferromagnetic state. We then took the numerical derivative to obtain $|d^2I/d^2V|$ as a function of temperature and applied bias, plotted in Fig. 6-9B. The dashed white line indicates the magnetic transition at 51 K, as determined from the temperature dependence of the resistance in the antiferromagnetic state (Fig. 6-9A).

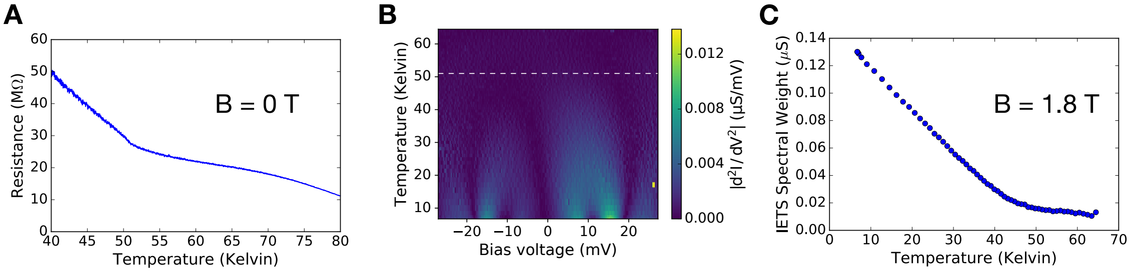

Figure 6-9: **A.** Temperature dependence of the resistance for a tetralayer $\mathrm{CrI_3}$ device (device D3), taken with an AC excitation of 300 μV without an applied magnetic field. The onset of the magnetoresistance effect (appearing as a kink) gives the Néel temperature, 51 K, of this sample. **B.** $|d^2I/dV^2|$ for the same device, plotted as a function of the DC bias voltage and temperature. The AC excitation was 500 μV. The dashed white line is at 51 K. The applied magnetic field for these data was 1.8 T, to avoid artifacts from the large resistance increase at zero magnetic field. **C.** IETS data from panel **B** integrated from -20 meV to 20 meV, showing the onset of inelastic tunneling below 50 K. The error bars are significantly smaller than the marker size.

The sharp inelastic features at low temperature quickly evolve into a single broad feature, which then decreases in intensity, disappearing completely just below the magnetic transition. We can quantify this trend by plotting the total IETS spectral weight (implemented by summing the IETS spectra over the range -20 meV to 20 meV). This is plotted in Fig. 6-9C, where we see that the IETS signal begins to onset just below 50 K. We do not expect a complete loss of spectral weight at this temperature from thermal broadening alone [109], suggesting some relation between the onset of magnetism and the inelastic tunneling features.

6.8.9 Bias dependence of the magnetoresistance ratio

In previous sections we have focused on the zero-bias magnetoresistance. Here, we examine the differential magnetoresistance ratio as a function of bias. We define this quantity as the ratio of the differential conductance taken with an external field of 2.5 T (in the fully aligned state) and -0.2 T (in the antiferromagnetic state). We plot this ratio in Figure 6-10A for a tetralayer CrI_3 barrier (device D1). The AC excitation was 500 µV and the temperature was 4.2 K. We see that, although the differential magnetoresistance ratio remains high for all bias values, it has a peak around zero bias. This has been observed in other magnetic tunnel junctions and could be a product of spin flip magnon scattering. For Figure 6-10A, the AC excitation frequency was reduced until the in-phase component of the tunneling current saturated, giving the correct quasi-DC value of the magnetoresistance ratio.

Figure 6-10B shows an analogous measurement for a CrI_3 bilayer tunnel barrier (device D2). Here, the temperature was 300 mK and the AC excitation was 200 µV. The data for the ferromagnetic configuration were taken with an applied magnetic field of 0.6 T and the data for the antiferromagnetic configuration were taken with 0.1 T applied magnetic field. These data also show a sharp decrease in differential magnetoresistance ratio around zero bias, but in this case the differential magnetoresistance ratio drops as low as 10% to 20%. This indicates that electrons tunneling through bilayer CrI_3 with energy above a few meV are likely not strongly spin polarized.

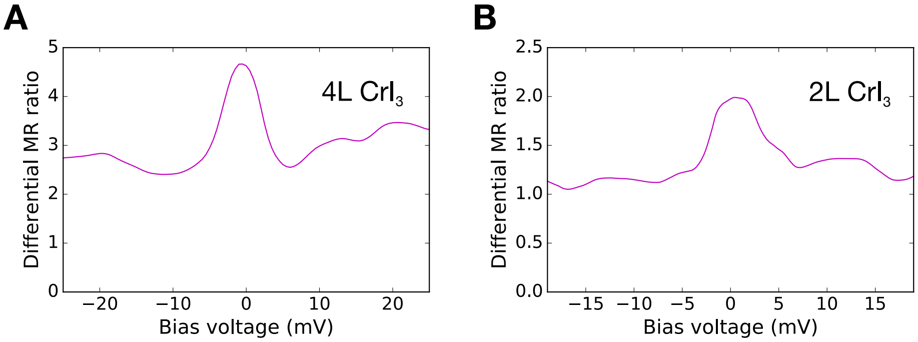

Figure 6-10: **A.** Ratio of differential conductance in the ferromagnetic configuration (with an applied field of 2.5 T) to differential conductance in the antiferromagnetic configuration (with an applied field of -0.2 T) as a function of a DC bias voltage. These data were taken on a tetralayer CrI_3 barrier junction (device D1) with a 500 µV AC excitation at 4.2 K. **B.** Ratio of differential conductance in the ferromagnetic configuration (with an applied field of 0.6 T) to differential conductance in the antiferromagnetic configuration (with an applied field of 0.1 T) as a function of a DC bias voltage. These data were taken on a bilayer CrI_3 barrier junction (device D2) with a 200 µV AC excitation at 300 mK.

6.8.10 Summary of CrI_3 tunneling devices

The following table presents CrI_3 layer number N, junction area A, zero-bias conductance G in the fully aligned magnetic configurations, and magnetoresistance for each measured device.

Table 6.1: Summary of CrI_3 tunneling devices

Device	N	A (µm^2)	G (µS)	**MR (%)**
D1	4	34 ± 2	0.073 ± 0.001	426 ± 3
D2	2	6.3 ± 0.2	0.977 ± 0.004	95 ± 1
D3	4	4.64 ± 0.04	0.0161 ± 0.0003	550 ± 10
D4	3	9.3 ± 0.3	0.52 ± 0.02	290 ± 30
D5	3	0.90 ± 0.09	0.0374 ± 0.0004	231 ± 5

Chapter 7

Enhancement of interlayer exchange in an ultrathin two-dimensional magnet

The following chapter is based on work published in *Nature Physics* (Ref. [13]), and appears here with modifications, corrections, and expanded discussions.

7.1 Abstract

Following the recent isolation of monolayer $\mathrm{CrI_3}$ [7], many more two-dimensional van der Waals magnetic materials have been isolated [8, 43, 45, 92, 110–113, 116, 155, 196]. Their incorporation in van der Waals heterostructures offers a new platform for spintronics [110–113, 116], proximity magnetism [19] and quantum spin liquids [54]. A primary question in this field is how exfoliating crystals to the few-layer limit influences their magnetism. Studies of $\mathrm{CrI_3}$ have shown a different magnetic ground state for ultrathin exfoliated films [7, 110, 111] compared with the bulk, but the origin is not yet understood. Here, we use electron tunneling through few-layer crystals of the layered antiferromagnetic insulator $\mathrm{CrCl_3}$ to probe its magnetic order and find a tenfold enhancement of the interlayer exchange compared with bulk crystals. Moreover, temperature- and polarization-dependent Raman spectroscopy reveals that

the crystallographic phase transition of bulk crystals does not occur in exfoliated films. This results in a different low-temperature stacking order and, we hypothesize, increased interlayer exchange. Our study provides insight into the connection between stacking order and interlayer interactions in two-dimensional magnets, which may be relevant for correlating stacking faults and mechanical deformations with the magnetic ground states of other more exotic layered magnets such as $RuCl_3$ [54].

7.2 Introduction

The layered transition metal trihalides are an important family of van der Waals magnets and have been studied for decades as prototypical magnetic insulators [42, 58] and as a platform for quasi-two-dimensional magnetism [197, 198]. In the chromium trihalides, the chromium atoms are arranged in a honeycomb structure, with each chromium atom surrounded by six halide atoms in an octahedral geometry (Fig. 7-1a). The bulk crystals undergo a crystallographic phase transition from a monoclinic phase (space group $C2/m$) at room temperature to a rhombohedral phase (space group $R\bar{3}$) at low temperatures (below about 240 K for $CrCl_3$ [49]). While the intralayer lattice spacings are largely unaffected by this transition, the layer stacking sequence changes from rhombohedral ABC ordering at low temperatures to $AA_{1/3}$ stacking above 240 K, where each layer is displaced along the a axis by 1/3 of a lattice vector (Fig. 7-1a). Bulk CrI_3 and $CrBr_3$ are ferromagnetic (FM) below their Curie temperatures, with moments aligned perpendicular to the ab plane; in contrast, bulk $CrCl_3$ is antiferromagnetic (AFM) below its Néel temperature (T_N) of 14 K [41, 44, 49]. The chromium moments in each layer of $CrCl_3$ are ferromagnetically coupled, but couple antiferromagnetically across the van der Waals gap (Fig. 7-1b). However, this interlayer exchange coupling is weak, and the magnetization of adjacent layers in bulk $CrCl_3$ can be aligned with a small in-plane magnetic field, $\mu_0 H_\parallel$, of about 0.2–0.25 T [49, 85].

The nature of stacking in few-layer chromium trihalides has recently attracted attention because of the observation of an AFM ground state and interlayer exchange

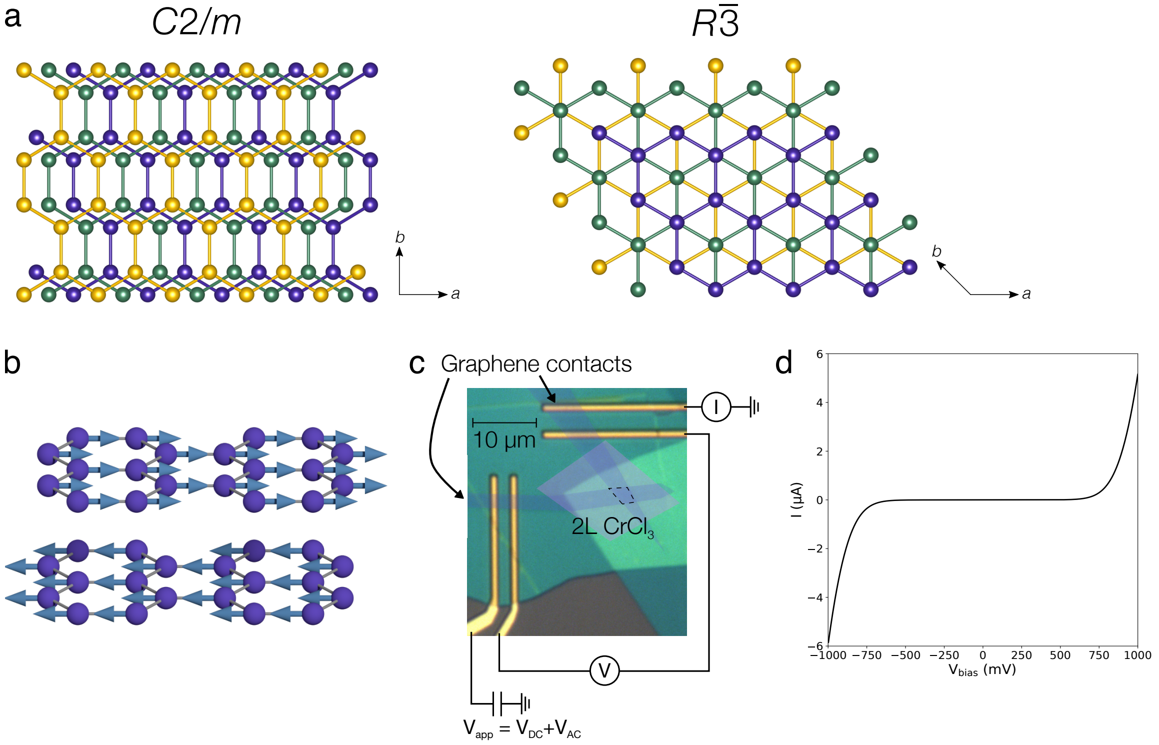

Figure 7-1: $CrCl_3$ stacking order and device characteristics. **a.** Stacking sequence of the chromium honeycomb sublattice in the $C2/m$ (high temperature, left) and $R\bar{3}$ (low temperature, right) phases of $CrCl_3$, viewed perpendicular to the ab plane. The colored spheres represent Cr^{3+} ions in three adjacent layers. In both cases, the first and fourth layers are approximately aligned. **b.** Schematic of moments in two adjacent layers at equilibrium. The moments lie in the ab plane. **c.** False-color optical microscope image of a bilayer $CrCl_3$ tunnel junction device with four-point contact geometry for differential conductance measurements (V_{app}, applied voltage; V_{DC}, DC voltage; V_{AC}, AC voltage). **d.** Current versus bias voltage (V_{bias}) for a trilayer tunnel junction at 4.2 K. The current was obtained by integration of the differential conductance with an AC bias voltage excitation of 50 mV.

in few-layer CrI_3, in contrast to the FM ground state of bulk crystals [7,110,111,123, 155,176]. This crossover from FM to AFM interlayer coupling has led to theoretical investigations centred on the origin of the AFM ground state in bilayer CrI_3 [81–83]. First-principles calculations predict that while the rhombohedral phase favors FM interlayer exchange, the monoclinic phase prefers an AFM alignment between the layers [81]. Thus, it is natural to propose that the observed AFM coupling results from a monoclinic stacking that persists to low temperatures in ultrathin CrI_3. However, this proposal has not been verified experimentally. For $CrCl_3$, both the crystal and magnetic structures of ultrathin films are unknown and could provide valuable insight into how stacking order and exfoliation couple to interlayer interactions in these materials.

In this work, we use electron tunneling to probe the magnetic structure and interlayer exchange coupling of few-layer $CrCl_3$ crystals. We first use mechanical exfoliation to obtain crystallites ranging from two to four layers in thickness. We then fabricate vertical magnetic tunnel junctions using two few-layer graphite electrodes above and below each $CrCl_3$ flake and encapsulated with hexagonal boron nitride (Fig. 7-1c, see Section 7.8.1). In the final step, each stack is transferred onto a silicon substrate with a 285 nm oxide layer and prepatterned titanium/palladium (Ti/Pd) wires contacting the graphite electrodes. The junctions show a high resistance (Fig. 7-1) with a nonlinear current–voltage (I–V) relationship characteristic of tunneling in the Fowler–Nordheim regime [97].

7.3 Magnetoresistance in $CrCl_3$ magnetic tunnel junctions

We find that the junction conductance increases when a magnetic field is applied in the plane of the crystal layers. Figure 7-2a shows the differential conductance for a tetralayer device as a function of bias, at 300 mK and with in-plane applied fields of 0 T and 2 T, where the AC excitation is 50 mV. The junction differential magnetoresistance

$$\mathrm{MR} = \frac{\frac{dI}{dV}\left(\mu_0 H_\parallel\right) - \frac{dI}{dV}\left(\mu_0 H_\parallel = 0\right)}{\frac{dI}{dV}\left(\mu_0 H_\parallel = 0\right)} \times 100\% \tag{7.1}$$

is plotted in Fig. 7-2b, where μ_0 is the permeability of free space, and $\mu_0 H_\parallel = 2$ T for the high-field measurement. Note that our definition of MR is mathematically equivalent to $(R_{\mathrm{LO}} - R_{\mathrm{HI}})/R_{\mathrm{HI}}$, where R_{HI} and R_{LO} refer to resistances with and without an applied magnetic field, respectively. Consistent with previous results [111] and the theory of spin filter tunneling [104], the differential magnetoresistance peaks

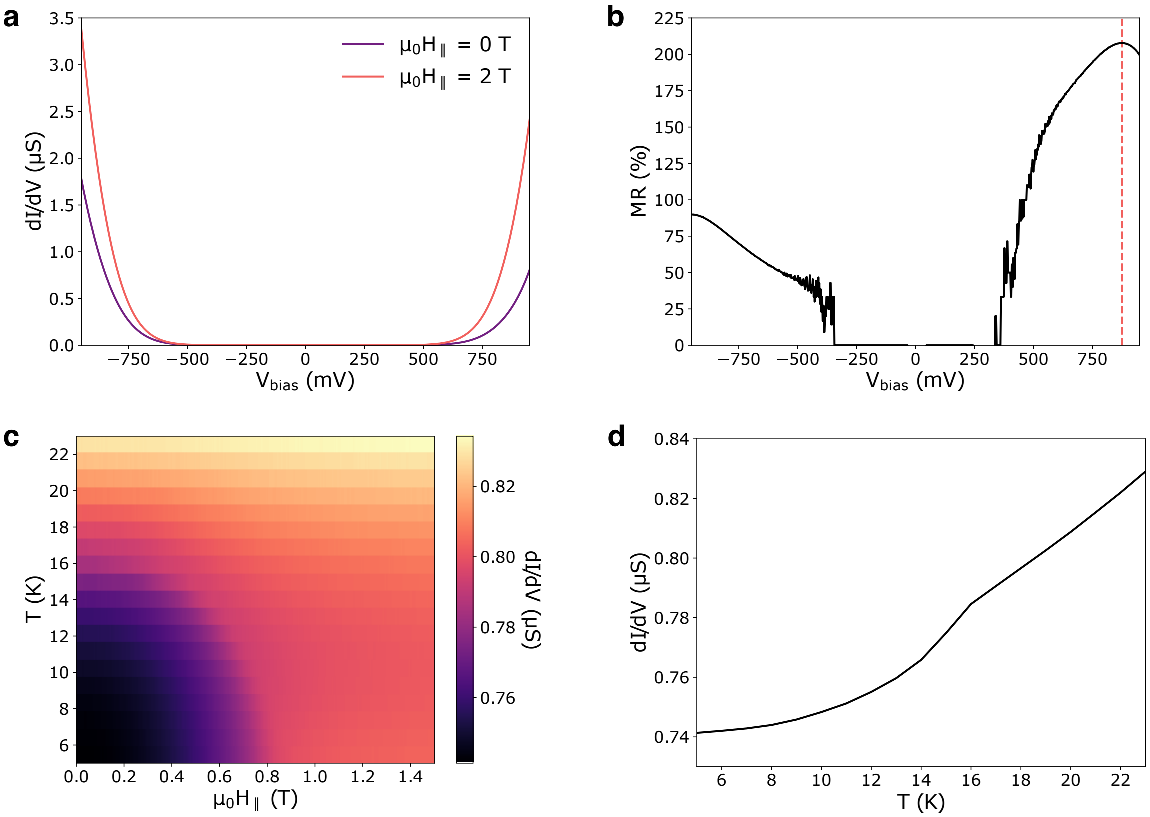

Figure 7-2: Magnetoresistance in $CrCl_3$ magnetic tunnel junctions. **a.** Differential conductance versus bias voltage for a tetralayer tunnel junction with an AC excitation of 50 mV at 300 mK. The data are taken at zero applied field (purple) and with an in-plane magnetic field of 2 T (pink). **b.** Magnetoresistance percent versus applied bias voltage for a tetralayer tunnel junction with a high-field in-plane magnetic field of 2 T, extracted from **a**. The dashed line at a bias of 875 mV indicates the optimum bias for magnetoresistance. **c.** Differential conductance versus applied in-plane magnetic field and temperature for a bilayer tunnel junction. The DC bias is -625 mV and the AC excitation is 50 mV. **d.** Vertical line cut from **c** at zero applied magnetic field. The kink between 15 K and 16 K indicates T_N.

at a finite bias value near the onset of Fowler–Nordheim tunneling (between 625 mV and 875 mV). This peak corresponds to a maximum of spin-polarized tunneling when the applied bias is sufficient to allow efficient Fowler–Nordheim tunneling for majority-spin electrons, which experience a lower energy barrier in the $CrCl_3$ when it is polarized, but not for minority-spin electrons, which experience a larger energy barrier. We investigate the temperature and field dependence of this phenomenon by plotting the tunneling conductance of a $CrCl_3$ bilayer device as a function of both magnetic field and temperature (Fig. 7-2c). A vertical line cut of conductance versus temperature at zero applied field (Fig. 7-2d) shows a marked decrease in the conductance between 15 K and 16 K. This drop reflects the onset of AFM alignment between the two layers in the junction, similar to the bulk Néel temperature [49]. If the interlayer exchange were FM instead, we would expect increased conductance in the magnetic state due to the lowering of the energy barrier for majority-spin electrons [97].

In principle, two mechanisms can provide magnetoresistance in our junctions: increasing the saturation magnetization within each layer (which decreases the majority-spin barrier [101]), and rotation of the magnetization in adjacent layers from antiparallel to parallel as the external field is increased (called the double spin filter effect [102, 104]). We expect that the latter effect is dominant in our junctions because (1) the observed Néel temperature is similar to bulk crystals, in which case, the magnetization in each layer is nearly saturated at $3\mu_\mathrm{B}$ per chromium atom by 10 K, and (2) we observe only a single kink in the conductance versus magnetic field curves, rather than the two that would be expected for an alignment of the layers followed by a saturation of the intralayer magnetization.

7.4 Thickness dependence of $CrCl_3$ magnetic tunnel junctions

To analyze our conductance versus applied magnetic field data at 4.2 K, and to extract the interlayer exchange, we model the magnetization as fully saturated within each layer and coupled between layers via an AFM exchange field, H_E (see Section 7.8.2 for the precise definition of our model and interlayer exchange field). The experimental magnetoresistance curves are shown in Fig. 7-3a. Consistent with the spin filter effect when tunneling through a magnetic insulating barrier [102, 199], the magnetoresistance increases with barrier thickness from 9% in a bilayer $CrCl_3$ device up to 208% in a tetralayer $CrCl_3$ device (Fig. 7-3c). The normalized magnetoresistance curves are displayed in Fig. 7-3b to emphasize the difference in saturation fields. In

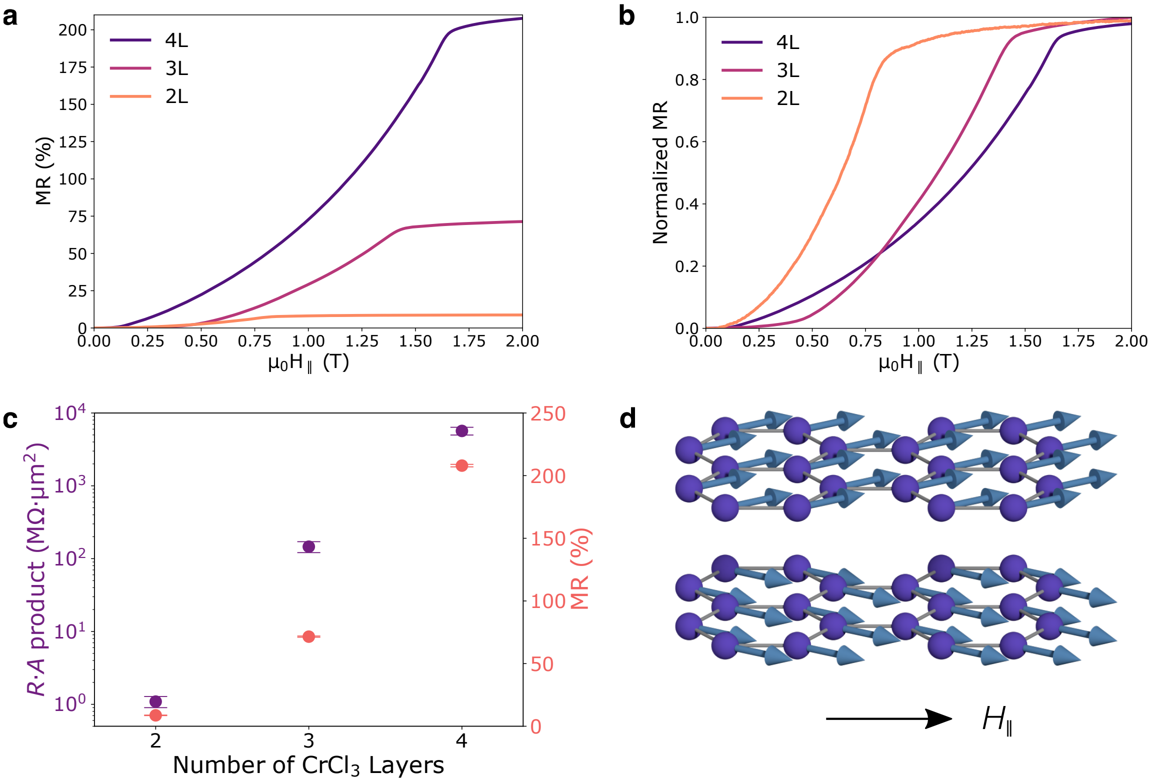

Figure 7-3: Thickness dependence of CrCl$_3$ magnetic tunnel junctions. **a.** Magnetoresistance versus applied in-plane magnetic field for bilayer, trilayer, and tetralayer tunnel junctions at finite applied bias and an AC excitation of 50 mV at 4 K. **b.** Normalized magnetoresistance versus applied in-plane magnetic field, obtained by dividing the value by the MR value at 2 T. **c.** Differential resistance–area ($R \cdot A$) product (purple) and magnetoresistance (pink) versus CrCl$_3$ layer number. The differential resistance was measured with an applied DC bias of 500 mV at 4 K for each device. Error bars in the differential resistance–area product and magnetoresistance represent estimated standard deviations arising from calculation of junction areas from optical microscope images and estimation of magnetoresistance plateaus, respectively. **d.** Schematic of moments in two layers canting towards the in-plane applied field.

all devices, the AFM to FM transition occurs at a much higher field than for bulk crystals (roughly 0.2–0.25 T) [49, 85]. These AFM–FM transition fields range from 0.85 T in the bilayer junction to 1.65 T in the tetralayer junction. The reported bulk interlayer exchange field is 0.084 T [197]. However, on the basis of the saturation fields in Fig. 7-3a, we calculate increased values for the exchange coupling of 0.86 T, 0.96 T, and 0.97 T in bilayer, trilayer, and tetralayer CrCl$_3$, respectively (see Section 7.8.2 for calculation of the interlayer exchange from the experimentally observed metamagnetic transition). The consistency of the extracted interlayer exchange coupling for different thicknesses, despite large differences in the saturation field, supports our hypothesis that the magnetoresistance arises from alignment of magnetic moments in adjacent layers.

These magnetoresistances thus demonstrate a more than tenfold increase in the interlayer exchange strength when $CrCl_3$ is cleaved to the few-layer limit. Furthermore, the thickness dependence of the interlayer exchange in the few-layer films is weak, and the interlayer exchange is seen to slightly increase with thickness in our devices. This suggests that the dramatic enhancement is due to a qualitatively different property of the exfoliated films compared with bulk (that is, their stacking order).

7.5 Raman spectroscopy of bulk and exfoliated $CrCl_3$

To explore our hypothesis of stacking order as the origin of enhanced interlayer exchange, we performed Raman spectroscopy on both bulk and exfoliated thin $CrCl_3$ crystals (Fig. 7-4). The experiments were performed in a backscattering geometry with a 532 nm laser, incident perpendicular to the crystal *ab* plane. The incident light was linearly polarized, and inelastically scattered photons were detected in the parallel-polarized channel (XX polarization geometry). The 247 cm^{-1} Raman mode of bulk $CrCl_3$ undergoes a marked peak shift close to 2 cm^{-1} at the crystallographic phase transition near 240 K [200]. This excitation corresponds to out-of-plane vibrations of chlorine atoms in the *ab* plane, which depend sensitively on the shearing of layers with respect to one another. To calibrate the peak position, we also fit the 209 cm^{-1} Raman mode, which does not shift at the phase transition, and plot the difference between the two peak energies.

We first studied the evolution of this energy difference when cooling a bulk crystal (Fig. 7-4a). Consistent with previous work [200], we observe a sharp shift in the peak energy difference between 240 K and 250 K (see Section 7.8.6 for complete spectra). Next, we examined the same peaks in an exfoliated crystal (35 nm thick) on a SiO_2/Si substrate. The peak difference shows minimal temperature dependence

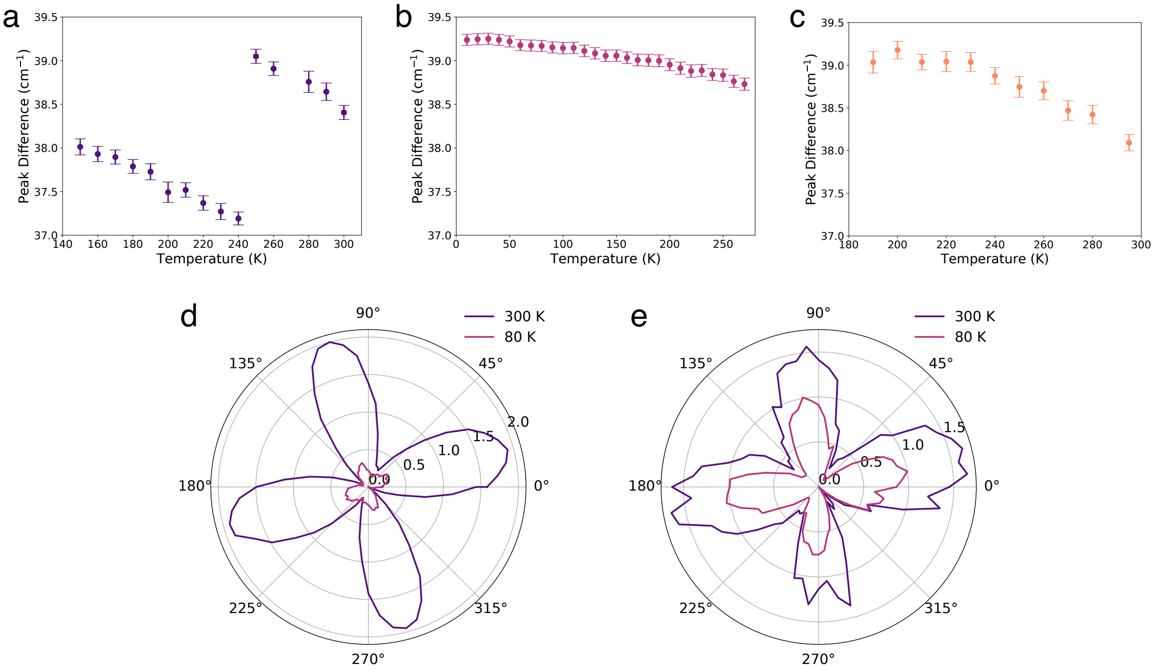

Figure 7-4: Raman spectroscopy of bulk and exfoliated $CrCl_3$. **a.** Difference between Raman peak positions of the 247 cm^{-1} and 209 cm^{-1} modes versus temperature for a bulk crystal of $CrCl_3$. A jump in the peak difference occurs around the crystallographic phase transition near 240 K. **b.** The same peak difference versus temperature for an exfoliated 35 nm thick flake of $CrCl_3$ on a 90 nm SiO_2/Si substrate. The peak difference smoothly evolves down to 10 K without evidence of a phase transition. **c.** The same peak difference versus temperature for an exfoliated 8 nm flake. **d.** Peak position shift (in cm^{-1}) relative to minimum of 247 cm^{-1} mode versus polarization angle for a bulk crystal. **e.** Same as **d** for an exfoliated 17 nm thick flake on a 90 nm SiO_2/Si substrate. All error bars reflect a 2σ confidence interval in fit parameters for the Raman peak positions.

and no evidence of a transition, even down to 10 K (Fig. 7-4b). We find similar results in an even thinner (8 nm thick) exfoliated crystal, with no apparent phase transition down to 180 K (Fig. 7-4c). This absence of a peak shift suggests that thin exfoliated $CrCl_3$ crystals remain in the high-temperature monoclinic phase at low temperatures. Another explanation is that deformation of the crystal during the aggressive exfoliation process introduces stacking faults. In fact, repeated deformation of a bulk α-$RuCl_3$ crystal by bending back and forth gives rise to stacking faults, leading to a change in the Néel temperature [201]. Thus, the exfoliation process itself probably plays a role in modifying the physical properties of thin van der Waals crystals, compared with their original bulk structures.

To further study the crystal phases of exfoliated versus bulk $CrCl_3$, we analyzed the energy of the 247 cm^{-1} Raman peak as a function of polarization angle. In the rhombohedral $R\bar{3}$ phase, this peak is produced by a doubly degenerate E_g mode, whereas in the monoclinic $C2/m$ phase, it arises from a combination of closely spaced A_g and B_g modes [202,203]. In both cases, the two modes contributing to the observed peak have opposite polarization dependence. When they are degenerate, the opposite polarization dependences of these modes cancel out, leading to a single peak with constant intensity at one energy, as seen in the $R\bar{3}$ phase. However, when the two modes are slightly offset in energy, their out-of-phase intensity variations lead to the observation of a combined peak whose position displays a fourfold modulation as a function of polarization angle (see Section 7.5 for a detailed analysis).

On the basis of these symmetry arguments, we can determine the crystal structure of bulk and thin films via polarized Raman spectroscopy. For a bulk crystal at 300 K (and therefore in the $C2/m$ phase), we observe a fourfold variation in the energy of this peak as we sweep the polarization angle (Fig. 7-4d). However, when cooling the bulk sample to 80 K, the peak energy oscillations become an order of magnitude smaller. This change is indicative of the crystallographic phase transition to the $R\bar{3}$ phase by 80 K (the small, resolution-limited residual signal may arise from some regions pinned in the high-temperature structure; see ref. [41]). In contrast, we found that a thin (17 nm thick) exfoliated flake on a SiO_2/Si substrate has fourfold variation in the 247 cm^{-1} mode peak position at both 300 K and 80 K (Fig. 7-4e). This result gives additional evidence that exfoliated $CrCl_3$ is in the monoclinic phase even at lower temperatures.

Note that the oscillation of the 247 cm^{-1} Raman peak energy in the exfoliated crystal is smaller at 80 K than at 300 K. This could arise from either a partial transition of the crystal into the low-temperature phase or some inherent temperature dependence of the peak oscillation due to inhomogeneous hardening of the closely lying phonon lines. We cannot rule out either scenario, but expect that our junctions are uniformly in the monoclinic stacking order. This is because we observe only a single kink in the magnetoresistance versus field traces, ruling out the presence of a highly non-uniform interlayer exchange coupling. In one trilayer device (Fig. 7-12), we did see a sharp increase in the magnetoresistance saturating around 0.15 T, which could arise from a stacking fault within the barrier creating coexisting regions of monoclinic and rhombohedral stacking.

To understand the dependence of the interlayer exchange on the stacking type, we carried out density functional theory (DFT) calculations of the energy difference between the FM and AFM states for bilayer $CrCl_3$ with various stacking arrangements (see Section 7.8.4). We find that the $C2/m$-type stacking in the bilayer favors an AFM interlayer alignment, whereas the $R\bar{3}$-type phase can favor AFM or FM coupling, depending on the chosen DFT functional and interlayer spacing. Furthermore, the difference in interlayer exchange energy between the $C2/m$-type and $R\bar{3}$-type structures is not very sensitive to the DFT functional used and shows that the $C2/m$-type phase always has notably larger AFM coupling than the $R\bar{3}$-type phase. For a realistic range of interlayer spacings from 0.55 nm to 0.65 nm, the calculated value of the interlayer exchange difference is of the same order as our experimental estimate. Overall, our calculations show that the $C2/m$-type phase has stronger AFM interlayer coupling than the $R\bar{3}$-type phase, consistent with the observed giant enhancement of interlayer exchange in ultrathin $C2/m$ $CrCl_3$.

7.6 Conclusion

In summary, we have demonstrated a tenfold increase in the interlayer exchange of ultrathin $CrCl_3$ crystals. We attribute this dramatic enhancement to the monoclinic low-temperature crystal structure of exfoliated crystals. It is currently unknown whether this stacking structure is the lowest energy configuration or is a metastable state pinned by disorder introduced by the exfoliation process. The low-temperature monoclinic order even in very thick exfoliated crystals suggests that the latter explanation is correct. This result has important implications for understanding the unexpected magnetic behaviour in the ultrathin chromium trihalides. For example, the FM to AFM transition observed in ultrathin CrI_3 is probably also a result of $C2/m$ stacking in the few-layer crystals, as has been predicted from first-principles calculations [81]. We have also noticed a small increase in the Néel temperature in our devices compared with the bulk. It is important to see whether the Néel temperature can be correlated with spatially resolved changes, such as stacking faults, using electron microscopy or second-harmonic generation spectroscopy. Finally, our study opens up the possibility to modify exchange couplings in other van der Waals magnets through strain, twisting and other methods [22].

7.7 Epilogue

In addition to this work on $CrCl_3$, other papers have since supported the claim that ultrathin CrI_3 crystals adopt monoclinic stacking at low temperatures, resulting in different interlayer magnetic couplings than in their bulk counterparts. An analysis of low-temperature second harmonic generation (SHG) in 2L CrI_3 is consistent with monoclinic stacking and additionally rules out rhombohedral stacking by symmetry arguments [204]. Furthermore, application of hydrostatic pressure has been shown to irreversibly transform few-layer CrI_3 from AFM to FM interlayer coupling, presumably from a change in stacking order [205, 206]. A study of a 9L CrI_3 flake using scanning NV magnetometry also demonstrated a 9-fold increase in magnetization accompanied by a change in the Raman spectrum after an unintentional puncture of the flake with the NV cantilever tip [123]. These results can also be attributed to a relaxation from the monoclinic to rhombohedral stacking, leading to a transition from AFM to FM behavior fully consistent with the 9-fold magnetization increase.

A more recent paper uses magnetic force microscopy (MFM) on intermediate thickness CrI_3 flakes (25-200 nm) to identify a crossover scale for this behavior [207]. Interestingly, they report that, regardless of thickness, the outer layers of approximately 12 nm on either side of the crystal remain pinned in the monoclinic stacking (AFM coupling), whereas the inner layers undergo the expected stacking transition to rhombohedral stacking (FM coupling). This is consistent with the picture of the few-layer CrI_3 flakes studied residing entirely in the monoclinic phase and behaving as layered antiferromagnets. In contrast, in bulk crystals, the approximately 25 nm of AFM-coupled monoclinic outer layers will be dwarfed by the majority of the layers in the rhombohedral phase behaving ferromagnetically.

It is worth noting that $CrBr_3$ has thus far demonstrated nearly identical properties in the bulk and exfoliated ultrathin limits, and that its structural phase transition to the low-temperature rhombohedral stacking occurs at 420 Kelvin, well above room temperature [41]. Unlike CrI_3 and $CrCl_3$, $CrBr_3$ is likely entirely in the rhombohedral stacking for all thicknesses.

The above experiments all involve thin crystals of CrX_3 obtained by exfoliating bulk crystals. However, one study using molecular beam epitaxy (MBE) to synthesize 2L $CrBr_3$ crystals demonstrates that alternative stacking configurations and thus interlayer magnetic couplings may be possible from a bottom-up synthesis approach [208]. Using spin-polarized scanning tunneling microscopy (SP-STM), they discover both FM and AFM couplings which are directly tied to the stacking order between the two $CrBr_3$ monolayers. In the future, more complex spin textures may also be enabled by twist-angle control in moiré superlattices of exfoliated ultrathin CrX_3 crystals [39].

7.8 Supplemental Information

7.8.1 Methods

Bulk $CrCl_3$ crystals were grown by recrystallization of anhydrous $CrCl_3$ flakes. Approximately 1.0 g of the flakes (99.9%, Alfa Aesar) was loaded into a silica ampule in an inert environment and sealed under vacuum. The ampule was placed in a three-zone tube furnace with source, growth and third zones held at 700°C, 550°C and 625°C, respectively, for a duration of six days. The source material was fully transported to the middle growth zone, where it recrystallized into flat platelet crystals.

Exfoliation of few-layer flakes from the bulk $CrCl_3$ was carried out in an argon glovebox to prevent hydration of the crystals. Optical contrast was employed to determine the thickness of each flake. The van der Waals magnetic tunnel junctions were then assembled by the dry transfer process in an argon environment.

The magnetic tunnel junctions were assembled by sequentially picking up flakes of BN, few-layer graphite, $CrCl_3$, few-layer graphite, and BN. The stacks were aligned such that the only vertical overlap between the two graphite electrodes is through the $CrCl_3$ tunnel barrier two to four layers in thickness. The use of top and bottom BN flakes provides protection from ambient conditions and an atomically flat substrate free of dangling bonds.

In each device, the final stack was transferred onto a silicon substrate wire-bonded to a chip carrier with a 285 nm oxide layer, also containing prepatterned Ti/Pd wires. The stack was aligned so that the two few-layer graphite electrodes contact the Ti/Pd wires.

Magnetotransport measurements were carried out in a helium-3 cryostat with an external magnetic field applied either parallel or perpendicular to the device. Differential conductance measurements were obtained using low-frequency lock-in methods (excitation frequency $<$20 Hz). Our DC measurements were performed by applying a DC bias to the sample and reading out the DC through a current preamplifier. All measurements were performed at fixed temperature (300 mK or 4.2 K), with the exception of the temperature-dependent data shown in Fig. 7-2c,d.

Polarized Raman experiments were performed in a backscattering geometry using a confocal microscope spectrometer (Horiba Evolution) with a 50× objective lens and 532 nm laser with a power of 2.0 mW. The spectrometer integration times were 5 minutes and 30 minutes for bulk and exfoliated crystals, respectively. Each scan was taken twice and then averaged before analysis.

The incident laser beam was linearly polarized in the vertical direction, and a half-wave plate was placed just before the objective. The analyzer was placed in front of the spectrometer entrance and kept vertical for parallel configuration (XX). For polarization dependence, the half-wave plate was rotated in steps of 2.5° from 0° to 180°.

7.8.2 Interlayer exchange model

In order to extract the interlayer exchange value from the magnetoresistance curves, we employ a simple model to describe the magnetization energy in the few-layer $CrCl_3$ tunnel barrier. We consider two different energy contributions: the exchange energy between layers and the Zeeman energy from the external field. Here we assume that the out-of-plane magnetization is zero and can thus ignore out-of-plane shape anisotropy.

The interlayer exchange energy per unit area for a barrier of n layers is:

$$U_{\mathrm{E}} = \frac{1}{2} d\mu_0 M_{\mathrm{s}} H_{\mathrm{E}} \sum_{j=1}^{n-1} \hat{m}_j \cdot \hat{m}_{j+1} \tag{7.2}$$

where d is the layer thickness, M_{s} is the effective saturation magnetization, H_{E} is the interlayer exchange field, and $\hat{m}_j$ is the unit magnetization vector of layer j. The Zeeman energy per unit area for an applied in-plane magnetic field $\vec{H}_{\mathrm{ext}}$ is given by:

$$U_{\mathrm{Z}} = -d\mu_0 M_{\mathrm{s}} \vec{H}_{\mathrm{ext}} \cdot \sum_{j=1}^{n} \hat{m}_j \tag{7.3}$$

By minimizing the total energy of the system $U = U_{\mathrm{E}} + U_{\mathrm{Z}}$, one can obtain a relationship between the external field and the exchange field as a function of magnetization directions in the layers. In the limit where the magnetizations all align with the external field, we obtain the value of the exchange field in terms of this saturation field required to fully polarize the layers.

We start with the bilayer $CrCl_3$ junction. We assume that the two layers' magnetization vectors $\hat{m}_1$ and $\hat{m}_2$ point equal and opposite from the applied magnetic field, illustrated in Fig. 7-5a. Thus, the energy can be written and minimized with respect to a single parameter ϕ:

$$\frac{U}{d\mu_0 M_{\mathrm{s}}} = \frac{1}{2} H_{\mathrm{E}} \hat{m}_1 \cdot \hat{m}_2 - \vec{H}_{\mathrm{ext}} \cdot (\hat{m}_1 + \hat{m}_2) \tag{7.4}$$

$$= -\frac{1}{2} H_{\mathrm{E}} \cos(2\phi) - 2H_{\mathrm{ext}} \sin\phi$$

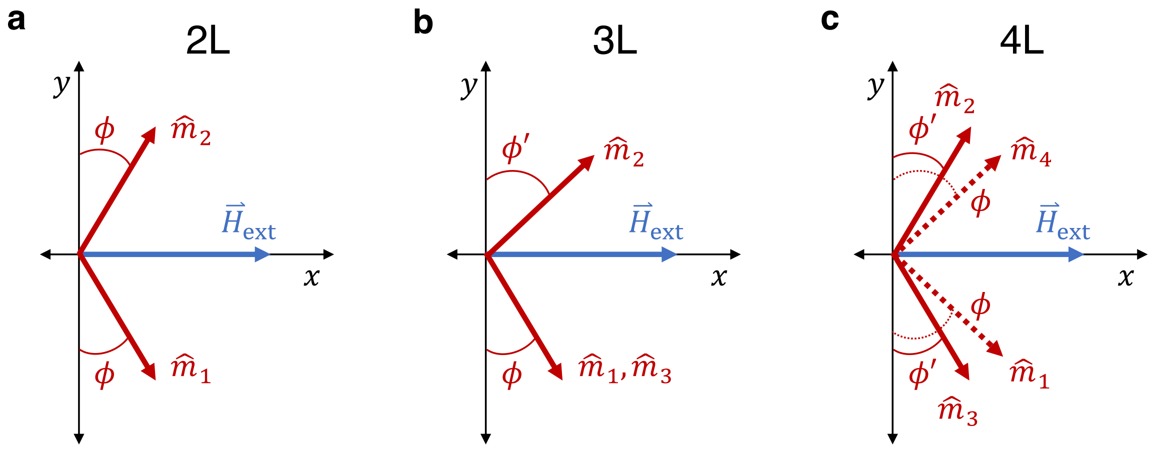

Figure 7-5: Schematic representation of unit magnetization vectors for few-layer CrCl$_3$. The vectors within the xy plane show the layer magnetization directions for (**a**) bilayer, (**b**) trilayer, and (**c**) tetralayer CrCl$_3$ crystals as the moments cant towards the applied field $\vec{H}_{\text{ext}}$ along the $+x$ axis.

$$\frac{\partial\left(\frac{U}{d\mu_0 M_{\text{s}}}\right)}{\partial\phi} = H_{\text{E}} \sin(2\phi) - 2H_{\text{ext}} \cos\phi = 0 \tag{7.5}$$

When $H_{\text{ext}} \leq H_{\text{sat}}$, the above equations have a solution:

$$H_{\text{ext}} = H_{\text{E}} \sin\phi \tag{7.6}$$

This determines ϕ as a function of H_{ext} in the antiferromagnetic state. The material is saturated when the two layers are fully aligned with the external field ($i.e.$ $\phi = 90°$) such that $H_{\text{ext}}(\phi = 90°) = H_{\text{sat}}$. Thus, we find $H_{\text{sat}} = H_{\text{E}}$ for 2L CrCl$_3$.

For trilayer CrCl$_3$, we assume that the top and bottom layers have equal magnetization directions (ϕ), but can have a different angle than the middle layer (ϕ'), as shown in Fig. 7-5b. Following the same procedure as for bilayer, we get:

$$\frac{U}{d\mu_0 M_{\text{s}}} = \frac{1}{2} H_{\text{E}}(\hat{m}_1 \cdot \hat{m}_2 + \hat{m}_2 \cdot \hat{m}_3) - \vec{H}_{\text{ext}} \cdot (\hat{m}_1 + \hat{m}_2 + \hat{m}_3) \tag{7.7}$$

$$= -H_{\text{E}} \cos(\phi + \phi') - H_{\text{ext}}(2\sin\phi + \sin\phi')$$

$$\frac{\partial\left(\frac{U}{d\mu_0 M_{\text{s}}}\right)}{\partial\phi} = H_{\text{E}} \sin(\phi + \phi') - 2H_{\text{ext}} \cos\phi = 0 \tag{7.8}$$

$$\frac{\partial\left(\frac{U}{d\mu_0 M_\mathrm{s}}\right)}{\partial\phi'} = H_\mathrm{E}\sin(\phi+\phi') - H_\mathrm{ext}\cos\phi' = 0 \tag{7.9}$$

Using the equations above, we can derive the following relation:

$$\frac{H_\mathrm{ext}}{H_\mathrm{E}} = \frac{1}{2}\sin\phi' + \sqrt{1-\frac{1}{4}(\cos\phi')^2} \tag{7.10}$$

We note that this relation only holds above a finite critical H_ext. This is because 3L $\mathrm{CrCl_3}$ has a net moment and, for low H_ext, this moment aligns with the applied field direction while keeping the sublattice moments antiparallel ($\phi = 90°$, $\phi' = -90°$). When we fix the angle $\phi' = 90°$ such that the 3L $\mathrm{CrCl_3}$ barrier is fully aligned with the external field, $H_\mathrm{sat} = 3H_\mathrm{E}/2$.

Finally, we consider four layers in which the outer two layers and inner two layers each have equal and opposite angles (ϕ and ϕ', see Fig. 7-5c). Following the same procedure as for 2L and 3L $\mathrm{CrCl_3}$, we can calculate:

$$\frac{U}{d\mu_0 M_\mathrm{s}} = \frac{1}{2}H_\mathrm{E}(\hat{m}_1\cdot\hat{m}_2 + \hat{m}_2\cdot\hat{m}_3 + \hat{m}_3\cdot\hat{m}_4) - \vec{H}_\mathrm{ext}\cdot(\hat{m}_1+\hat{m}_2+\hat{m}_3+\hat{m}_4) \tag{7.11}$$

$$= -H_\mathrm{E}\cos(\phi+\phi') - \frac{1}{2}H_\mathrm{E}\cos(2\phi') - H_\mathrm{ext}(2\sin\phi + 2\sin\phi')$$

$$\frac{\partial\left(\frac{U}{d\mu_0 M_\mathrm{s}}\right)}{\partial\phi} = H_\mathrm{E}\sin(\phi+\phi') - 2H_\mathrm{ext}\cos\phi = 0 \tag{7.12}$$

$$\frac{\partial\left(\frac{U}{d\mu_0 M_\mathrm{s}}\right)}{\partial\phi'} = H_\mathrm{E}\sin(\phi+\phi') + H\mathrm{E}\sin(2\phi') - 2H_\mathrm{ext}\cos\phi' = 0 \tag{7.13}$$

From the above equations, we obtain the following relation:

$$\frac{H_\mathrm{ext}}{H_\mathrm{E}} = \sin\phi' + \frac{1}{2}\sin\phi'\left(1-\frac{H_\mathrm{E}}{H_\mathrm{ext}}\sin\phi'\right) + \frac{1}{2}\sqrt{1-(\cos\phi')^2\left(1-\frac{H_\mathrm{E}}{H_\mathrm{ext}}\sin\phi'\right)^2} \tag{7.14}$$

Evaluating the above expression for $\phi' = 90°$ gives a quadratic equation with solution $H_\mathrm{sat} = (1+\sqrt{2}/2)H_\mathrm{E}$ for 4L $\mathrm{CrCl_3}$.

7.8.3 Raman symmetry analysis

$\mathrm{CrCl_3}$ has two bulk crystallographic phases resulting in different symmetry-allowed Raman modes. At low temperature, it adopts a rhombohedral structure with space group $R\bar{3}$ and point group $C_{3i} = S_6$. At high temperature, it has a monoclinic structure with space group $C2/m$ and point group C_{2h}.

The phonon modes all form irreducible representations of the point group, yielding information about their symmetries and their Raman activity. The optical representations for the C_{3i} and C_{2h} point groups, respectively, are $4A_g + 3A_u + 4E_g + 3E_u$ and $6A_g + 4A_u + 6B_g + 5B_u$. The A and B representations are singlets; the E representations are doublets.

The cross section (and thus intensity) for Raman scattering from mode Q_i is proportional to:

$$I_i \propto \frac{d\sigma_i}{d\Omega} \propto \left| \hat{e}_s \frac{\partial \tilde{\alpha}}{\partial Q_i} \hat{e}_i \right|^2 \tag{7.15}$$

where $\tilde{\alpha}$ is the polarizability tensor, $\frac{\partial \tilde{\alpha}}{\partial Q_i}$ is the Raman tensor for mode Q_i, and $\hat{e}_{i,s}$ are the polarization directions of the incident (i) and scattered (s) light.

Let us first consider the low temperature rhombohedral phase with point group C_{3i}. Raman active modes must be even under inversion, resulting in two Raman active irreps A_g and E_g. The Raman tensors are given by:

$$A_g = \begin{bmatrix} a & 0 & 0 \\ 0 & a & 0 \\ 0 & 0 & b \end{bmatrix}, \quad {}^1E_g = \begin{bmatrix} c & d & e \\ d & -c & f \\ e & f & 0 \end{bmatrix}, \quad {}^2E_g = \begin{bmatrix} d & -c & -f \\ -c & -d & e \\ -f & e & 0 \end{bmatrix} \tag{7.16}$$

We assume a backscattering geometry with incident light along the -z direction and reflected light along the $+z$ direction. For parallel polarization in the xy-plane making an angle θ with respect to the x-axis, we have $\hat{e}_i = \hat{e}_s = (\cos\theta, \sin\theta, 0)$. The Raman tensors are complex valued; we take the pairs a, b and c, d to have the same phase without loss of generality.

We analyze the polarization dependence of the 247 $\mathrm{cm^{-1}}$ Raman peak in Section 7.5 (Fig. 7-4). At low temperatures in bulk $\mathrm{CrCl_3}$, this corresponds to the doubly-degenerate E_g mode. By plugging in the tensors from Eq. 7.16 into Eq. 7.15, we obtain:

$$I({}^1E_g) \propto \left|\hat{e}_s{}^1E_g\hat{e}_i\right|^2 = |c\cos(2\theta) + d\sin(2\theta)|^2 \tag{7.17a}$$

$$= c^2(\cos(2\theta))^2 + 2cd\cos(2\theta)\sin(2\theta) + d^2(\sin(2\theta))^2$$

$$I({}^2E_g) \propto \left|\hat{e}_s{}^2E_g\hat{e}_i\right|^2 = |d\cos(2\theta) + c\sin(2\theta)|^2 \tag{7.17b}$$

$$= d^2(\cos(2\theta))^2 - 2cd\cos(2\theta)\sin(2\theta) + c^2(\sin(2\theta))^2$$

We can see that the two components of intensity vary oppositely with polarization angle. However, since the E_g mode is degenerate, these contribute to a peak at the same frequency. Summing the two intensities gives a constant $c^2 + d^2$. Thus, the 247 cm^{-1} peak in the rhombohedral structure should be polarization independent, consistent with our observations of the bulk peak energy at 80 K (Fig. 7-4d).

In contrast, let us consider the high temperature monoclinic phase with point group C_{2h}. Its two Raman active irreps are A_g and B_g with the following Raman tensors:

$$A_g = \begin{bmatrix} a & 0 & d \\ 0 & a & 0 \\ d & 0 & c \end{bmatrix}, \quad B_g = \begin{bmatrix} 0 & e & 0 \\ e & 0 & f \\ 0 & f & 0 \end{bmatrix} \tag{7.18}$$

The high temperature 247 cm^{-1} peak reflects the two nearly-overlapping A_g and B_g modes at slightly different frequencies. The polarization angle dependence of these two modes is again obtained by substituting Eq. 7.18 into Eq. 7.15:

$$I(A_g) \propto |\hat{e}_s A_g \hat{e}_i|^2 = |a(\cos\theta)^2 + b(\sin\theta)^2|^2 \tag{7.19a}$$

$$= \frac{1}{4}(a^2+b^2) + \frac{1}{8}(a+b)^2 + \frac{1}{8}(a-b)^2\cos(4\theta) + \frac{1}{2}(a^2-b^2)\cos(2\theta)$$

$$I(B_g) \propto |\hat{e}_s B_g \hat{e}_i|^2 = |e\cos\theta\sin\theta + e\cos\theta\sin\theta|^2 \tag{7.19b}$$

$$= e^2(\sin(2\theta))^2$$

Since the A_g and B_g modes in the $C2/m$ phase pair to form the degenerate E_g mode in the $R\bar{3}$ phase, the parameters in the Raman tensors for these sets of modes must have matching symmetry patterns. Therefore, the 247 cm^{-1} peak's A_g mode has $a \sim -b$, resulting in an intensity $I(A_g) \propto a^2(\cos{(2\theta)})^2$. The observed Raman signal will be the sum of intensities from the two modes at different frequencies, which have opposite 4-fold dependences on the polarization angle. Thus, the overall peak should oscillate in energy in a 4-fold pattern versus polarization angle. This modulation is observed in the bulk crystal Raman signal at 300 K (Fig. 7-4d), as well as the exfoliated thin crystal Raman signals at both 300 K and 80 K (Fig. 7-4e).

We note that while the Raman tensor components can be complex, the relative phases between the entries cancel out in the intensities of the B_g and E_g modes. For the A_g mode, a small relative phase between a and b would give a small constant contribution to the intensity independent of polarization angle. This correction does not affect the conclusions of the symmetry analysis.

7.8.4 Density functional theory calculations

We performed spin-polarized density functional theory (DFT) calculations of bilayer CrCl_3 with magnetic moments of the Cr atoms aligned within each layer. We calculate the total energy of the bilayer system assuming the magnetic moments of the two layers are either aligned (FM) or opposite each other (AFM). The energy difference, defined as $\Delta E = E(\text{FM}) - E(\text{AFM})$ below, can then be determined for different stacking arrangements of the layers. We use projector augmented-wave (PAW) pseudopotentials [209] as implemented in the Vienna Ab initio Simulation Package (VASP) [210, 211]. For the calculations to converge, the energy cutoff for plane wave basis is set at 350 eV with a 17×17×1 Brillouin zone sampling in k-space. Because calculations of magnetic energy differences are very sensitive to the DFT setup, we have repeated the calculations under various conditions. We employed a Cl pseudopotential with 7 valence electrons ($3s^2 3p^5$) and considered Cr pseudopotentials with either 6 or 12 valence electrons ($3d^5 4s^1$ or $3p^6 3d^5 4s^1$, respectively). Aside from the conventional local density approximation (LDA) [212] and Perdew-Burke-Ernzerhof (PBE) approximation [213] functionals, we also considered the optB86b-vdW exchange functional [214, 215] with the vdW correlation functional [216]. In addition, we considered the effect of the on-site Coulomb interaction for the Cr d states using the simplified, rotationally invariant LSDA + U method [217] with Hubbard parameter $U = 3$ eV for chromium atoms [81]. We have chosen nine representative combinations of pseudopotentials, exchange-correlation functionals, and U values to demonstrate the overall dependence of magnetism on stacking order.

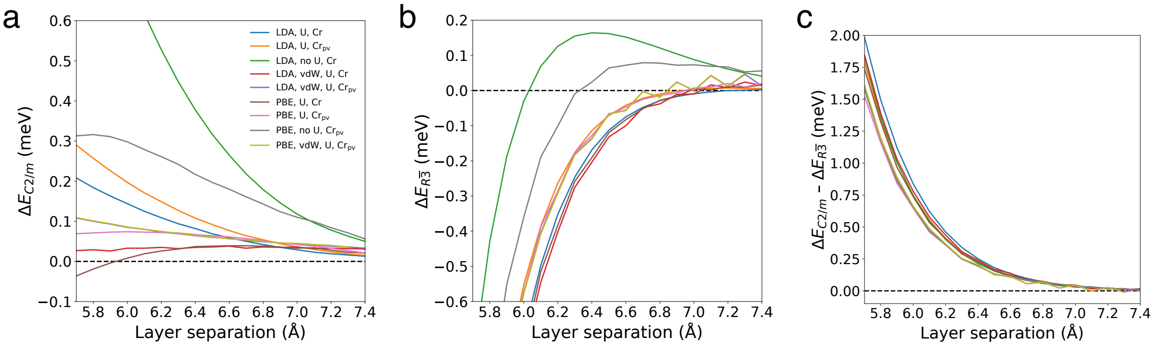

Figure 7-6: Calculated energy difference versus layer spacing. **a.** Calculated energy difference between FM and AFM states for bilayer $CrCl_3$ as a function of interlayer separation in the $C2/m$-type configuration using different DFT functionals. **b.** Same calculations as in **a** for the $R\bar{3}$-type configuration. **c.** Difference between the $C2/m$-type and $R\bar{3}$-type energy differences versus interlayer separation.

First, we consider the energy difference between the FM and AFM states versus layer spacing for interlayer alignments of bilayer $CrCl_3$ corresponding to the bulk $C2/m$ and $R\bar{3}$ phases (Fig. 7-6a and 7-6b). The $C2/m$-type plots (Fig. 7-6a) have a positive energy difference between the FM and AFM states, indicating a strong preference for AFM coupling in the ground state of bilayer $CrCl_3$. In contrast, the $R\bar{3}$-type curves (Fig. 7-6b) vary between positive and negative energy differences depending on the chosen DFT functional and layer separation, therefore indicating a weaker preference for AFM coupling. Nonetheless, the difference between the two phases (Fig. 7-6c) shows that the $C2/m$-type phase always has a much larger AFM coupling strength than the $R\bar{3}$-type phase regardless of choice of DFT functional.

Second, we generalize our analysis beyond the $C2/m$-type and $R\bar{3}$-type configurations to examine the overall dependence of interlayer coupling on relative stacking at fixed layer separation (Fig. 7-7). At a realistic interlayer spacing value of 6 Å, we find that $R\bar{3}$-type stacking sits at a local maximum favoring FM coupling, while

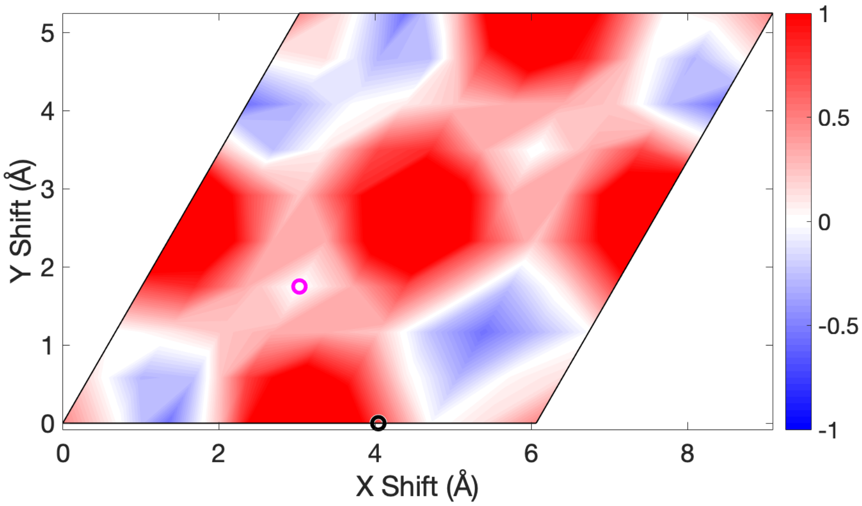

Figure 7-7: Calculated energy difference versus layer displacement. Calculated energy difference (in meV) between FM and AFM states for bilayer $CrCl_3$ as a function of interlayer displacements in the in-plane x and y directions. The layer separation is fixed at 6 Å and the DFT functional used is LDA using a Cr pseudopotential. The $C2/m$-type and $R\bar{3}$-type stacking phases are indicated by the black and magenta circles, respectively.

$C2/m$-type stacking lies near the local minimum favoring AFM coupling.

Together, these DFT calculations are in agreement with our observed results from tunneling magnetoresistance and Raman spectroscopy measurements. They support the conclusion that ultrathin $CrCl_3$ adopts a $C2/m$-type stacking order at low temperatures and therefore exhibits markedly stronger AFM interlayer coupling than bulk $CrCl_3$ in the $R\bar{3}$ configuration.

As a final quantitative check, we compare the energy difference in Fig. 7-6c with estimated energy differences for ultrathin and bulk $CrCl_3$ from experimental data. The work per unit volume required for an applied magnetic field to magnetize a material is given by $dW = \mu_0 H dM$. During the magnetization process of bilayer $CrCl_3$, the component of $\vec{M}$ along the applied field direction obeys $M(H) = M_s H/H_{sat}$ (see Section 7.8.2). Therefore, to fully saturate $CrCl_3$, the total work density is $W = \int_0^{M_S} dM \mu_0 H_{sat} M_s/2$. Since $M_s = 3\mu_B$ per Cr atom volume, the work done per Cr atom is $W = 3\mu_0\mu_B H_{sat}/2$. As the AFM to FM transition in $CrCl_3$ occurs via a coherent and reversible rotation of the moments (see Fig. S3 7-10), this is also the (free) energy difference between the AFM state and the fully polarized FM state

$\Delta E = E(\mathrm{FM}) - E(\mathrm{AFM})$. To estimate the value for a $C2/m$-type bilayer, we use the observed saturation field $\mu_0 H_{\mathrm{sat}}$ of 0.86 Tesla for bilayer $\mathrm{CrCl_3}$. We multiply our value by 4 to match the 4 Cr atoms used in the DFT calculation, yielding an estimate for the energy difference $\Delta E = 0.30$ meV. Next, we estimate the $R\bar{3}$-type bilayer energy difference. We assume that the saturation field in and $R\bar{3}$-type bilayer would be half of the bulk $R\bar{3}$ saturation field (0.25 Tesla) since each layer only couples to one adjacent layer rather than two. Therefore, we find that the energy difference is $\Delta E = 0.043$ meV. Finally, we subtract the two values for ΔE, yielding a difference in the interlayer exchange per unit cell between the two stacking types of approximately 0.26 meV. This value is on the same order as the energy difference in Fig. 7-6c for realistic values of layer separation from 0.55 nm to 0.65 nm.

7.8.5 Additional data from $\mathrm{CrCl_3}$ tunneling measurements

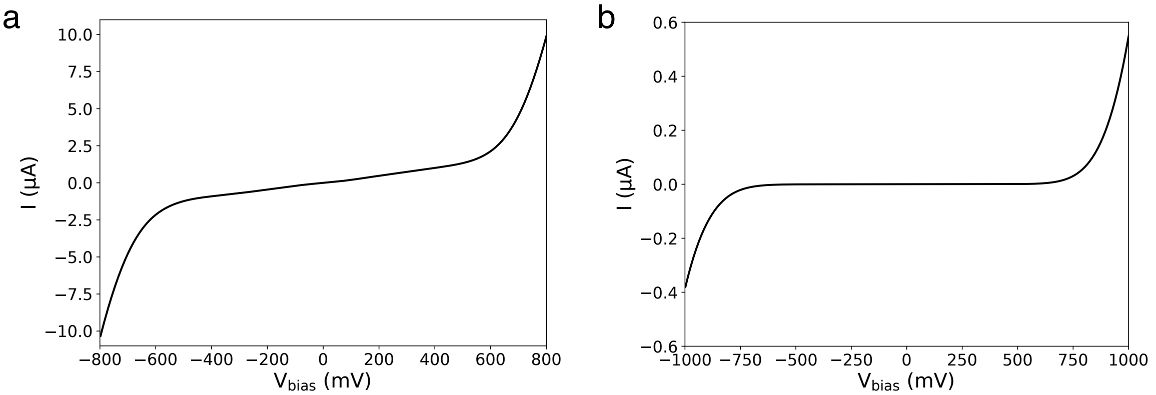

Figure 7-8: Current-voltage curves. Current versus bias voltage for (**a**) bilayer and (**b**) tetralayer $\mathrm{CrCl_3}$ devices at 4.2 K with an AC excitation of 50 mV. The DC current values were calculated by integrating the differential conductance and fixing the current to be zero at zero applied DC bias. The sharp increase of current at finite bias indicates tunneling in the Fowler-Nordheim regime.

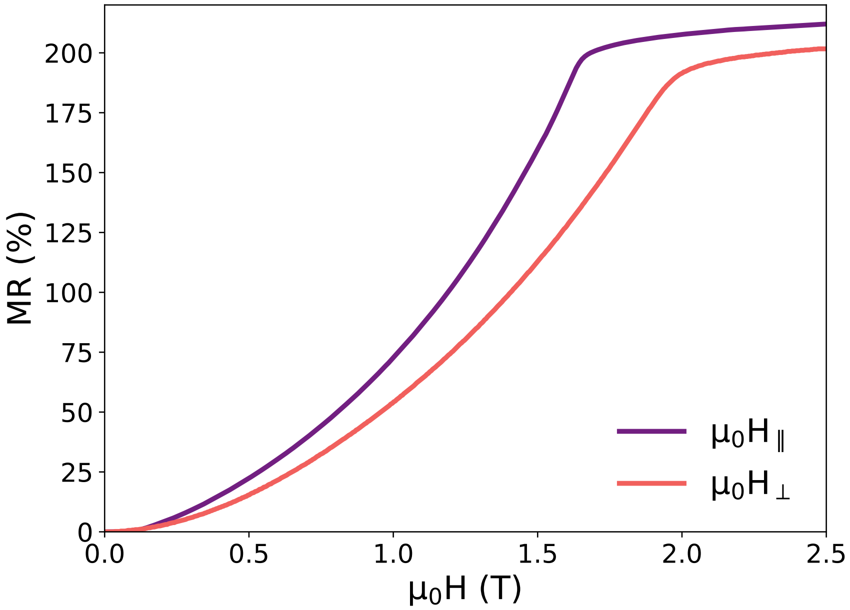

Figure 7-9: Directional dependence of magnetoresistance. Magnetoresistance versus applied magnetic fields in the in-plane (purple) and out-of-plane (pink) directions for a tetralayer $CrCl_3$ device. The out-of-plane magnetoresistance saturates at a field of 1.95 Tesla, 0.3 Tesla larger than the in-plane saturation field of 1.65 Tesla. This difference is consistent with the observed demagnetization field of 0.35 Tesla in bulk $CrCl_3$ [49].

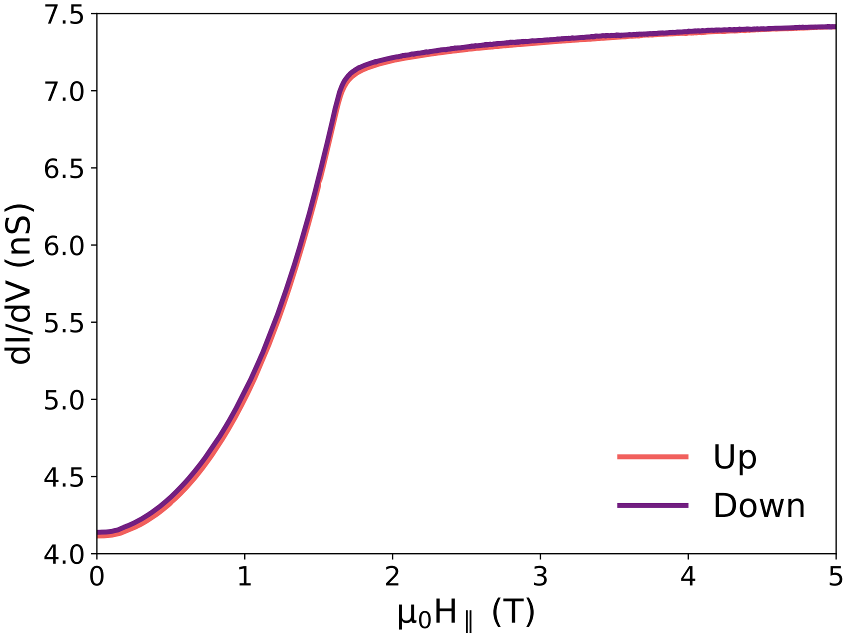

Figure 7-10: Reversibility of magnetoresistance. Differential conductance versus applied in-plane magnetic field swept up (pink) and down (purple) for a tetralayer $CrCl_3$ device at 4.2 K with an AC excitation of 500 mV. The traces demonstrate no hysteresis in the tunnel junction magnetoresistance.

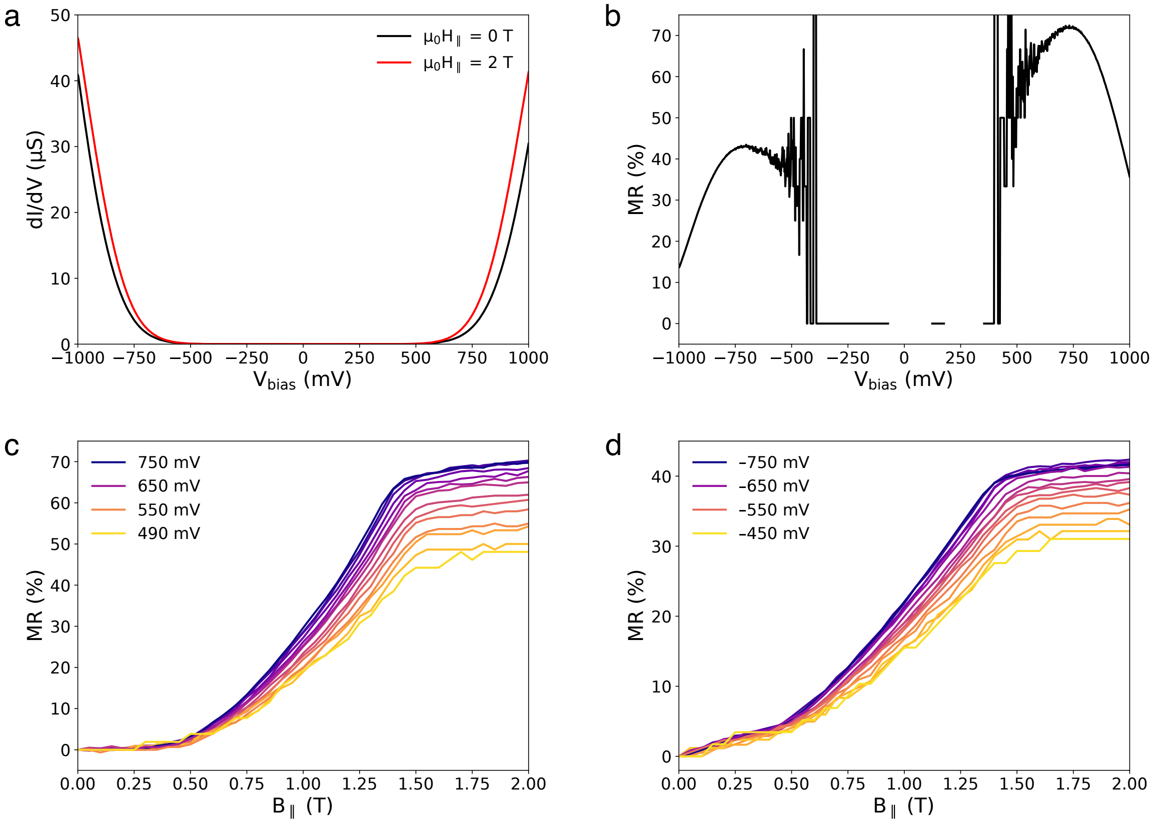

Figure 7-11: Bias dependence of a trilayer device. **a.** Differential conductance versus bias voltage for a trilayer tunnel junction with an AC excitation of 50 mV at 300 mK. The data are taken at zero applied field (black) and with an in-plane magnetic field of 2 Tesla (red). **b.** Magnetoresistance percent versus applied bias voltage with a high-field in-plane magnetic field of 2 Tesla, extracted from **a**. **c,d.** Magnetoresistance percent for the same device taken at different (**c**) positive and (**d**) negative bias voltages with an AC excitation of 50 mV at 4K. The saturation field where the MR plateaus remains effectively constant over a wide bias range.

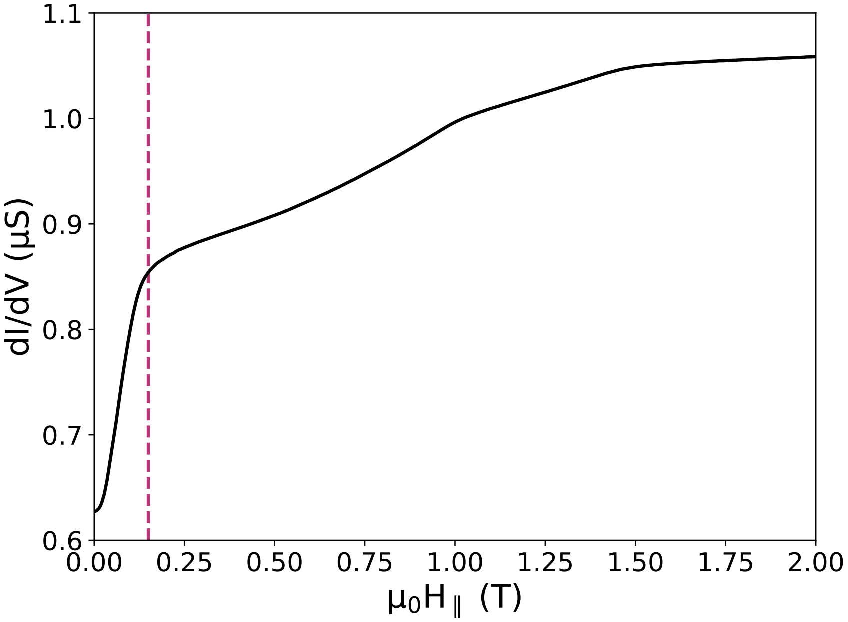

Figure 7-12: Additional trilayer device. Differential conductance versus applied in-plane magnetic field for a different trilayer $CrCl_3$ tunneling device taken at 4 K with a bias voltage of -625 mV and AC excitation of 50 mV. The dashed purple line denotes an applied field of 0.15 T. Using this value for the saturation field for 3L $CrCl_3$ gives an interlayer exchange field of approximately 0.1 T, similar to the reported bulk value of 0.084 T [197]. This observation suggests that the $CrCl_3$ barrier in this device may have domains of both rhombohedral and monoclinic stacking.

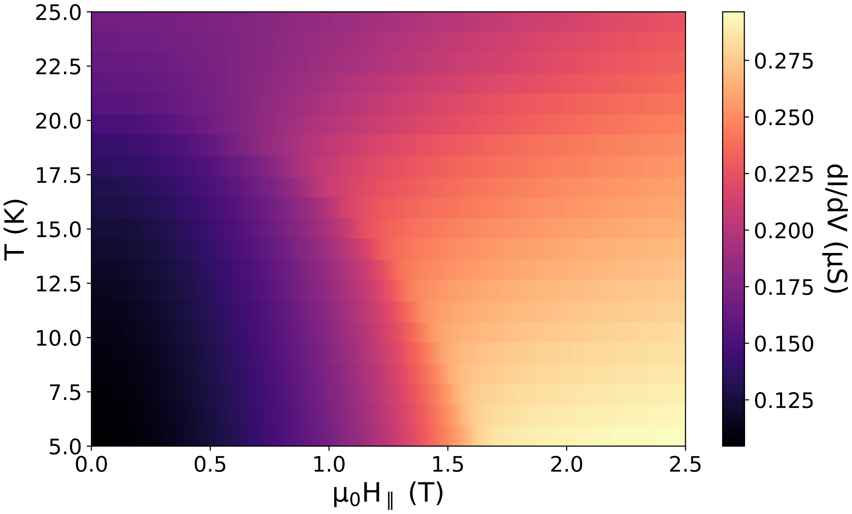

Figure 7-13: Temperature dependence of tetralayer device. Differential conductance versus applied in-plane magnetic field and temperature. The DC bias is 750 mV and the AC excitation is 50 mV.

7.8.6 Additional Raman spectroscopy data

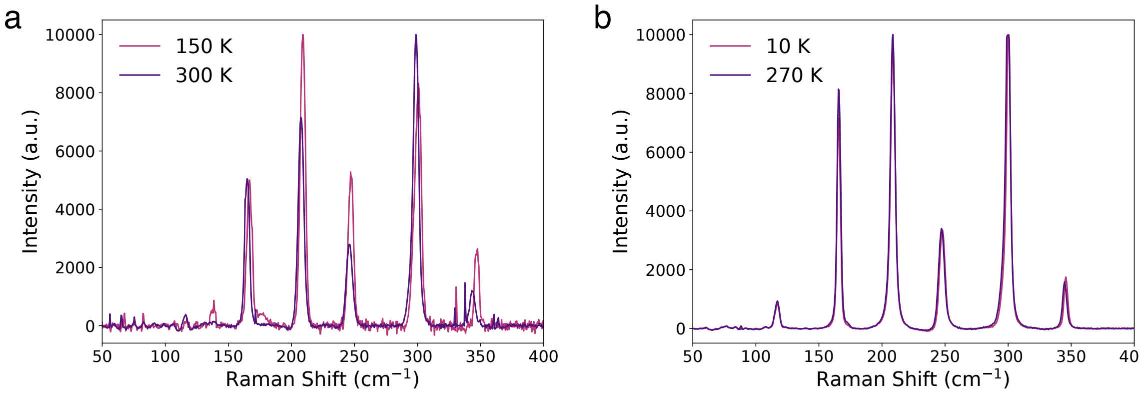

Figure 7-14: Raman spectra of bulk and exfoliated $CrCl_3$. Raman spectra at high and low temperatures of (**a**) a bulk crystal and (**b**) an exfoliated 35 nm thick flake. The spectra were taken using a 532 nm laser and parallel configuration (XX). The background has been subtracted from each trace.

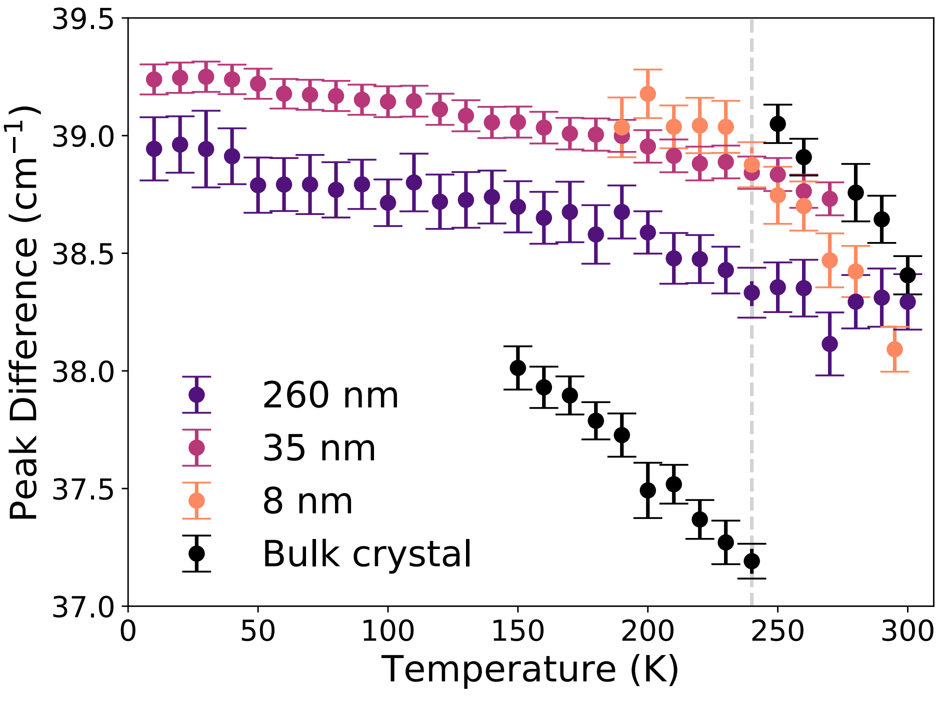

Figure 7-15: Temperature dependence of Raman peaks. Difference between Raman peak positions of the 247 cm^{-1} and 209 cm^{-1} modes versus temperature for a bulk crystal and exfoliated flakes of $CrCl_3$. A jump in the peak difference occurs around the crystallographic phase transition near 240 K for bulk $CrCl_3$ but not for the exfoliated flakes. The data for bulk, 35 nm, and 8 nm samples are shown in Fig. 7-4a-c, respectively.

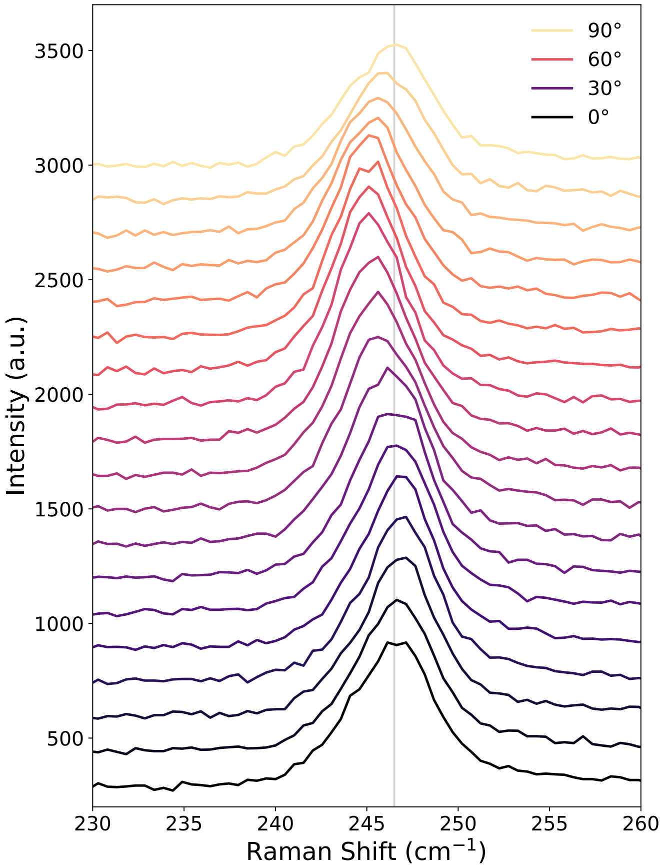

Figure 7-16: Polarization dependence of bulk crystal Raman peak. Raman spectra of the 247 cm^{-1} peak in a bulk crystal with polarizations ranging from 0° to 90° in 5° steps. The data were taken at 300 K and the polarization was changed using a half-wave plate rotated from 0° to 45° in 2.5° steps.

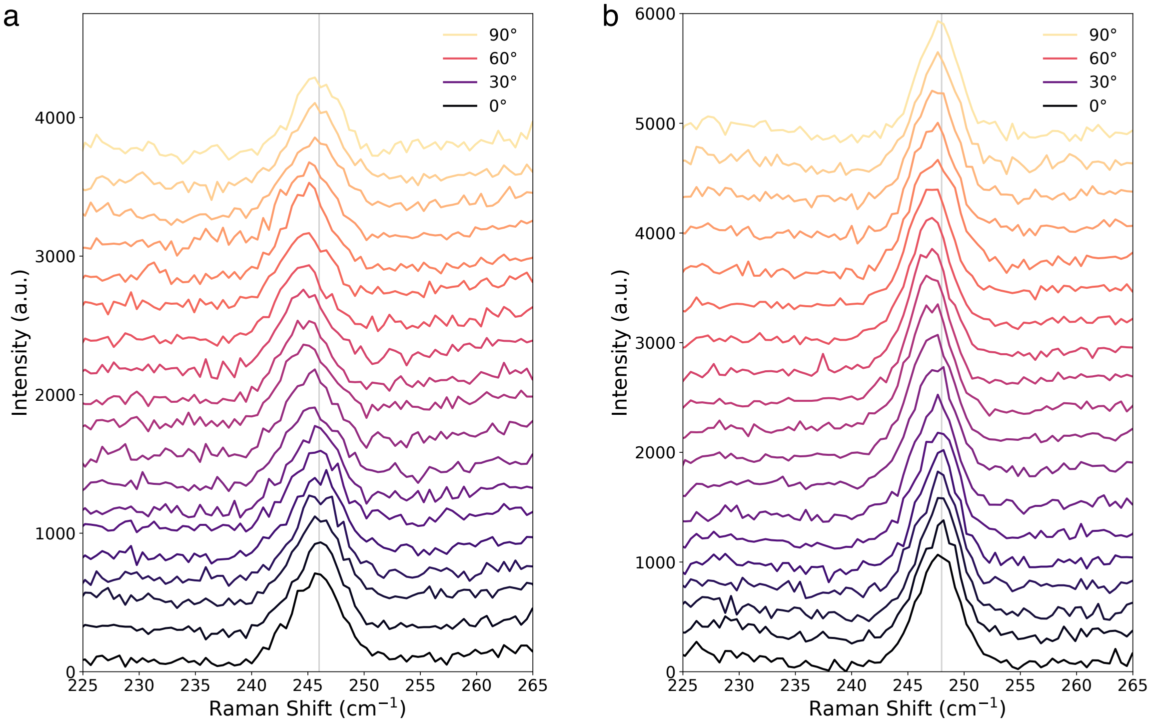

Figure 7-17: Polarization dependence of exfoliated crystal Raman peak. Raman spectra of the 247 cm^{-1} peak in an exfoliated 17 nm thick crystal with polarizations ranging from 0° to 90° in 5° steps. The data were taken at (**a**) 300 K and (**b**) 80 K. The polarization was changed using a half-wave plate rotated from 0° to 45° in 2.5° steps.

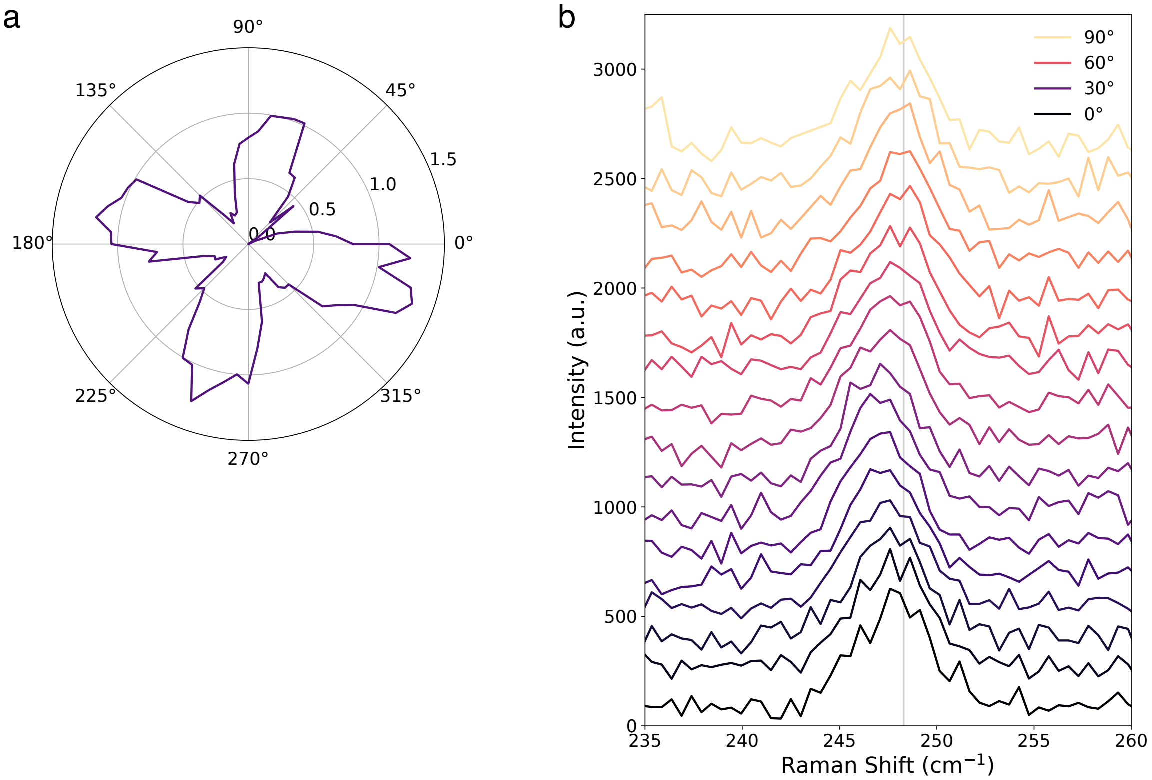

Figure 7-18: Polarized Raman of exfoliated $CrCl_3$ at 10 K. **a.** Peak position shift (in cm^{-1}) relative to minimum of 247 cm^{-1} mode versus polarization angle for an exfoliated 85 nm thick flake on a 90 nm SiO_2/Si substrate at 10 K. **b.** Raw Raman spectra of the data in **a** from 0° to 90°. The polarization was changed using a half-wave plate rotated from 0° to 45° in 2.5° steps.

Chapter 8

Outlook

The field of van der Waals magnetism is still in its infancy and many opportunities remain to discover new materials and capabilities within it. In this chapter, I describe some of these possible paths.

8.1 Expanding the family of 2D magnets

Over the past five years, dozens of 2D magnets have been experimentally investigated with a wide range of magnetic, electrical, and optical properties. Nevertheless, the number of yet unexplored van der Waals magnets far outnumbers these studies.

A key step for incorporating ultrathin magnetism into practical applications is to identify a room-temperature, air-stable magnet with small coercivity and robust anisotropy, ideally perpendicular to the layers. These features would enable scalable, low-power switching devices that do not require liquid helium or inert conditions to operate. One such material could be lurking in the list of predicted van der Waals magnets. Another route towards this goal, however, could be chemical modifications such as alloying, substitutional doping, or intercalation to enhance T_{C} and stabilize the magnetic anisotropy of a previously studied 2D magnet.

Moreover, van der Waals materials have yet to include multiferroicity. Multiferroic materials combine two or more ferroic orders such as ferromagnetism, ferroelectricity, and ferroelasticity. These materials are of great interest for new types of switchable magnetoelectronic devices. Several van der Waals materials display intrinsic ferroelectricity, including MnI_2 [179], $CuInP_2S_6$ [218], α-In_2Se_3 [219], and 1T'-WTe_2 [220]. There is ample room to explore both discovering an intrinsic van der Waals multiferroic as well as engineering a multiferroic interface of a van der Waals magnet/ferroelectric heterostructure [221].

Further, advancements in growth techniques could give rise to higher quality bulk crystals, and consequently exfoliated flakes with lower defect densities. Recent developments in TMD growth have demonstrated that flux-grown crystals have two orders of magnitude fewer point defects compared to their CVT-grown counterparts [222]. Extending these methods to van der Waals magnets could lead to improved magnetic stability.

The intrinsic van der Waals gap also gives us the opportunity to explore naturally heterostructured materials that have alternating layers of different van der Waals monolayers within a single crystal [65, 223]. One example, the MBT family of antiferromagnetic topological insulators (TIs), has already demonstrated exotic physics including QAH and axion insulator states [66, 67]. Further exploration into these materials could yield an intrinsic out-of-plane ferromagnetic TI with QAH states in the absence of an external magnetic field at even higher temperatures.

Additionally, weak van der Waals bonding let us restack 2D materials into moiré heterostructures with correlated insulating states, including ones that have surprisingly demonstrated spontaneous polarization without an applied magnetic field [26–29]. Conventional 2D magnets contain elements from the transition and rare earth blocks of the periodic table that have unpaired d or f electrons, such as Cr^{3+} or Fe^{2+}. In contrast, these moiré magnetic systems, like magic-angle twisted bilayer graphene aligned to BN, are built from atoms without intrinsic magnetic moments. Instead, the polarization is understood to arise from the orbital magnetization in bands with nonzero Chern number. In graphene systems, the K and K' valleys carry equal and opposite Chern number due to their opposite Berry curvature. If the bands are filled equally, there will be no net Chern number. However, in twisted bilayer graphene, the bands become extremely flat, enabling strong electron correlations that drive spontaneous polarization to fill bands with a nonzero net Chern number. This gives rise to the observation of the QAHE [224, 225].

There are still many open questions about competing ground states in these strongly correlated systems to be answered on both the experimental and theoretical fronts in this evolving field. For example, the introduction of an aligned BN layer to the monolayer graphene in twisted monolayer-bilayer graphene (tMBG) adds an additional staggered potential term that could modify the system's bandwidths and ground-state Chern numbers [226]. Moreover, these systems are predicted to have stable fractional Chern insulator states certain fillings of the moiré unit cell at zero applied field, which would make them the first platform to display the fractional quantum anomalous Hall effect (FQAHE) [227].

Another area for further exploration are the Kitaev quantum spin liquids, which are theoretically predicted to host Majorana fermions [35]. Aside from the interest from a fundamental physics perspective, there is a long-term goal of realizing and controlling these fractionalized excitations as a platform for topologically-protected qubits in quantum computing applications. The 2D zigzag antiferromagnet α-RuCl$_3$ is believed to realize this Kitaev QSL Hamiltonian to an excellent approximation, but further investigations in related materials could uncover additional candidates.

Finally, van der Waals magnets could have unconventional magnon excitations, including dissipationless edge modes in a topological magnon insulator [77]. Many of these materials, including CrX$_3$, CGT, and α-RuCl$_3$, have moments strongly localized on magnetic ions arranged on a honeycomb lattice. A ferromagnet with spins on a honeycomb lattice has a spin excitation spectrum that is a direct bosonic analog of the Dirac fermion dispersion in graphene [194], including two spin-wave branches that meet at topologically protected Dirac cones. These Dirac magnon systems behave differently than their electronic counterparts due to Bose-Einstein statistics and strong magnon-magnon interactions that renormalize the magnon band structure, which could experimentally manifest exotic spin excitations.

8.2 Controlling magnetism

The most natural method to control magnetic order is the application of an external magnetic field. However, the extreme sensitivity of ultrathin van der Waals magnets on their environment enables other methods to tune their magnetism.

Previous work on magnetic thin films has demonstrated that electric fields and currents can effectively switch their magnetic order, an important step for integration in applications [159]. The van der Waals community has already proven these approaches, showing electrically tunable magnetism in a growing number of materials including CrI_3 [155,176,177], $MnBi_2Te_4$ [228], and graphene moiré magnets [26,28,29]. Electrical doping using ionic liquid gating has also been an effective means to increase T_C of a trilayer FGT flake up to 320 K [9]. While the mechanism is not fully understood, and could be due to Li^+ ion intercalation in the crystal, it nonetheless achieved electrically-induced ferromagnetism above room temperature in a van der Waals material, a promising step towards room-temperature applications.

Another approach that has been explored is applying hydrostatic pressure to change the magnetic order of a magnet. Since CrI_3's stacking order is directly linked to its interlayer exchange, two experiments have shown that applying large hydrostatic pressure up to 2 GPa can induce a stacking phase transition from monoclinic to rhombohedral at low temperatures [205,206]. This consequently results in a change from antiferromagnetic to ferromagnetic interlayer coupling, which is confirmed using tunneling magnetoresistance, RMCD, and Raman spectroscopy before and after the pressure was applied. One caveat of this technique is that the phase transition is irreversible; the crystal remains in the rhombohedral phase even when the pressure is released, making it less attractive for use as a tuning knob in applications.

The interfacial exchange bias field between two magnetic layers is a common technique to stabilize the magnetization of a thin-film ferromagnet by pinning its moments at the interface. Due to their sharp interfaces, van der Waals heterostructures of two different magnets could be used to modify an existing 2D magnet. Recently, it was proposed that the exchange bias in a CrI_3/MBT heterostructure may pin the perpendicular magnetization at the interface of a few-layer MBT crystal, thereby leading to a more robust zero-field QAH state [229].

8.3 Applications in spintronics

A natural extension of van der Waals magnet research is looking for new ways to integrate into spintronics. One challenge in the field is generation of spin-polarized electrical currents. Van der Waals spin-filter magnetic tunnel junctions (MTJs) using CrI_3 have demonstrated extremely large TMR up to one million percent, corresponding to highly spin-polarized currents when the CrI_3 barrier is aligned with a magnetic field due to the double spin-filter effect. These types of devices could be used to generate spin-polarized currents, as well as detect incoming spin polarizations due to their high sensitivity to electron spin. Van der Waals MTJs have also been demonstrated in the more conventional geometry of two ferromagnetic electrodes sandwiched by a non-magnetic insulator using van der Waals heterostructures of FGT and BN [230]. Both flavors of MTJs could be developed for magnetic memory devices, with one study already showing both electrical switching and electrical readout of the magnetic state in a bilayer CrI_3 MTJ [119]. Nevertheless, further progress towards high-temperature operation and low-power switching would be necessary for most realistic applications.

These MTJs could be further developed into magnetic random access memory (MRAM) architectures based on spin-transfer torque (STT) or spin-orbit torque (SOT). In STT-MRAM, the spin-polarized current generated from a magnetic layer is used to switch the magnetization of another layer. In SOT-MRAM, however, a material with large SOC instead uses its spin angular momentum to switch an adjacent magnetic layer. This type of device typically has reduced Joule heating which could lead to a more efficient magnetic memory. Room-temperature SOT-induced switching of a thin magnetic film using the TMD WTe_2 has been previously reported [183], offering hope for development of a fully van der Waals SOT-MRAM device.

Another field within spintronics is the study of magnons. Some van der Waals magnets, like CrI_3, have magnons in the terahertz (THz) range. Others, like $CrCl_3$, have antiferromagnetic resonance that lie the gigahertz (GHz) range, which is easily accessible with microwave driving [85]. Future studies could utilize these materials to further study both their spin dynamics and controlling magnon propagation across a device.

Finally, half metals, which have only a single electron spin polarization at the Fermi level, are of interest as 100% spin-polarized current sources. No van der Waals magnets have been experimentally confirmed, though numerous transition metal halide candidates have been proposed, including MnX_3 [231], FeX_2 [232], and monolayer VCl_3 [233]. These materials could be used as the critical component of a new class of spin field-effect transistors that generate fully spin-polarized currents with spin polarization controlled by gate voltage [234].

8.4 Magnetic van der Waals heterostructures

Some van der Waals heterostructures using 2D magnets have already been addressed in this chapter, including combining with ferroelectrics for multiferroic interfaces, building van der Waals MTJs, and discovering new unconventional magnetic moiré superlattices. Beyond these, there are other heterostructures that take advantage of magnetic proximity effects across the narrow van der Waals gap.

Monolayer 2H-phase TMDs have spin-valley locking at the K and K' valleys of the Brillouin zone due to the effects of strong SOC on their band structure [235]. Placing a monolayer TMD onto a 2D magnet leads to large valley Zeeman splitting, which has already resulted in effective proximity magnetic fields exceeding 10 Tesla [19, 236]. First-principles calculations suggest that certain TMD/magnet combinations could have even larger valley Zeeman splittings of over 100 Tesla, far exceeding what one could achieve with an external magnetic field [237]. These heterostructures could also have band inversion arising from charge transfer at the interface and topologically nontrivial states, which would result in valley-polarized QAH systems.

Combining superconductors and magnets is another attractive possibility with van der Waals heterostructures. Superconducting and magnetic orders naturally compete with one another, making the interplay at such an interface a rich area for investigation of topological superconductivity. Very recently, these have begun to be experimentally explored via MBE growth of monolayer $CrBr_3$ on the superconductor $NbSe_2$ [238]. In addition, unconventional superconductors with triplet pairing would be robust to magnetic layers since the Cooper pairs are aligned with the same spin, unlike the conventional s-wave singlet pair. Heterostructures enabling triplet pairing may enable the realization of robust Majorana zero modes for braiding experiments proposed for topological quantum computing applications.

Furthermore, in addition to the intrinsic magnetic TIs such as MBT, van der Waals heterostructures combining ferromagnets and TIs could also give rise to QAH states from proximity magnetism. These systems would be advantageous over the magnetically doped TIs that suffer from unavoidable defect states due to doping.

On a final note, twisting of the existing 2D magnets could yield novel moiré-induced noncollinear spin textures that do not appear in a natural magnet [39]. Unlimited choice of the twist angle paves the way for exploring new spin states, as well as their renormalized magnon spectra.

Appendix A

Growth of bulk chromium trihalide crystals

A.1 Chemical Vapor Transport

Chemical vapor transport (CVT) is a method of bulk crystal growth that utilizes a gaseous transport agent to transport a solid from one region (the source) to another region (the sink) in the ampule where the final product forms and crystallizes [239]. This is achieved by varying the equilibrium of forward and back reactions in the ampule using a temperature gradient. This gradient is usually established in a two- or three-zone furnace, where each zone has a different temperature setpoint. The gradient thus establishes a heterogeneous equilibrium along the length of the ampule.

We can consider two simultaneous chemical reactions occurring primarily in different zones. First, we have the forward reaction at the source zone:

$$\mathrm{A}_{(g)} + \mathrm{B}_{(s)} \rightleftharpoons \mathrm{C}_{(g)} \tag{A.1}$$

Here, the gaseous transport agent A transfers the solid precursor B into the gas phase in the form of a new gaseous compound C. Second, we have the back reaction at the sink zone:

$$\mathrm{C}_{(g)} \rightleftharpoons \mathrm{D}_{(s)} + \mathrm{E}_{(g)} \tag{A.2}$$

Here, C decomposes into the target solid compound D along with a gaseous compound E. D nucleates and crystallizes into the final product that we wish to extract. Crystallization of D decreases its concentration in the equilibrium reaction, thereby driving the production of more C from A and B at the source zone in accordance with Le Châtelier's Principle. The rate-determining step in the entire process is the diffusive flow of C along the length of the ampule. These reactions are shown schematically in Fig. A-1.

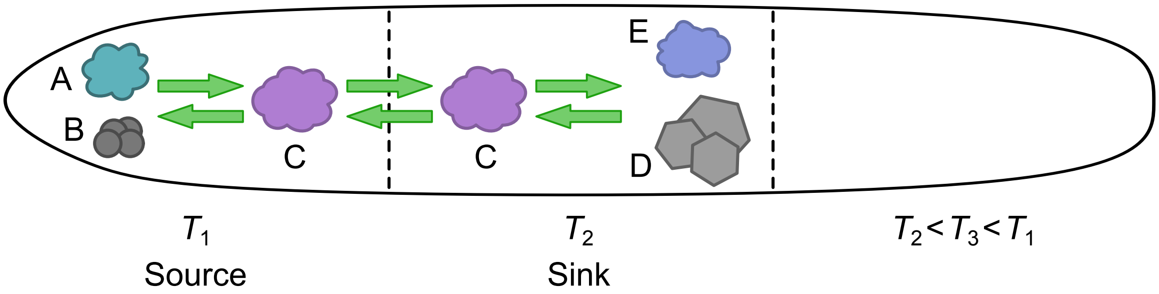

Figure A-1: Schematic drawing of a CVT reaction in a three-zone furnace. The target compound D crystallizes in the sink zone of the ampule.

There are several important factors to consider when optimizing a CVT reaction. First, one wants to choose a volatile transport agent that will combine with the precursor(s) to form gaseous compound(s) at high temperatures that will diffuse along the ampule. In some cases, it is one of the precursors itself — this is called direct vapor transport (DVT) or auto transport. If the transport agent is not a component of the target crystal, it should be inert and easily separable from the final product. Some common transport agents include halogens (I_2, Br_2, and Cl_2), oxide halides, and hydrogen halides.

Next, choosing a temperature gradient requires careful balance of equilibria [239]. If the reaction is too exergonic (*i.e.* free energy $\Delta_r G^\circ \ll 0$), then the back reaction is not thermodynamically favorable, and thus no crystallization will occur. On the other hand, if the reaction is too endergonic (*i.e.* $\Delta_r G^\circ \gg 0$), then the forward reaction is not thermodynamically favorable and very little solid will be transported out of the source zone. An ideal CVT reaction will therefore have a balanced equilibrium constant neither too large nor too small such that neither reaction direction is too dominant.

One also wants to optimize the growth conditions for a slow transport rate. This is ideal for undisturbed nucleation, which will result in larger single crystals instead of many small nucleation sites and minimize defects such as twinning. The disadvantage of a slow rate is that CVT can have long growth times, sometimes several weeks long. We can use Schäfer's equation for the diffusion (mass transport) rate in the reaction $i\mathrm{A}_{(s)} + k\mathrm{B}_{(g)} \rightleftharpoons j\mathrm{C}_{(g)}$ [240]:

$$\frac{dn_{\mathrm{A}}}{dt} \propto \frac{i}{j}\frac{\Delta p(\mathrm{C})}{\sum p}\frac{q}{s}\bar{T}^{0.75} \tag{A.3}$$

where $\Delta p(\mathrm{C})$ is the partial pressure difference of C between source and sink, $\bar{T}$ is the mean temperature, q is the cross-sectional area of the ampule, and s is the distance between source and sink. In designing the ampule, we want to minimize the ratio q/s by making the ampule long and with a small cross-sectional area. Our ampules have a total length of 55 cm and inner diameter of 16 mm. The length was chosen to be the maximum length to still allow transfer into the glovebox after growth in order to extract the crystals in an inert atmosphere.

The temperatures are typically chosen to introduce a small temperature gradient $(50 - 100°C)$. The source (T_1) is chosen to be hotter than the sink (T_2) if the net reaction $(A + B \rightarrow D + E)$ is exothermic. If employing a third zone in the furnace, as depicted in Fig. A-1, one usually sets it at an intermediate temperature in between the other two. This third zone can then act to keep the back reaction localized in the sink at the center of the ampule.

Finally, an initial period of an inverted gradient can improve CVT growth [241]. Using this method, the sink is set to be hotter than the source at the start of the growth process. This procedure helps clear out any precursors and impurities that may have remained in the sink zone during ampule loading, which would serve as nucleation sites and possibly facilitate the formation of defects in the final crystal products.

A.2 Growth of CrI_3

Our growth of CrI_3 was adapted from previously reported growth conditions in Ref. [41] using I_2 as the transport agent in a direct vapor transport growth. Our forward (a), back (b), and net (c) reactions are:

$$\mathrm{Cr}_{(s)} + \frac{x}{2}\mathrm{I}_{2(g)} \rightleftharpoons \mathrm{CrI}_{x(g)} \tag{A.4a}$$

$$\mathrm{CrI}_{x(g)} \rightleftharpoons \mathrm{CrI}_{3(s)} + \frac{x-3}{2}\mathrm{I}_{2(g)} \tag{A.4b}$$

$$\mathrm{Cr}_{(s)} + \frac{3}{2}\mathrm{I}_{2(g)} \rightleftharpoons \mathrm{CrI}_{3(s)} \tag{A.4c}$$

Our silica ampules have a total length of 67 cm, inner diameter of 16 mm, and outer diameter of 19 mm. The open end of the ampule has a length of 9 cm followed by a narrow neck with a length of 3 cm and inner diameter of 3 mm. This gives a length of approximately 55 cm after flame sealing the ampule shut at the narrow neck.

We use a home-built vacuum pump setup equipped with a 3-way valve connected to both vacuum and an argon cylinder. The vacuum pump line is connected to a diffusion pump backed by an oil roughing pump. The setup has vertical metal bellows with a 180° elbow section at the top and an NF25 compression fitting. The ampule is secured into place and suspended from the fitting.

We begin by loading chromium powder (99.5%, Sigma-Aldrich) and anhydrous iodine beads (99.999%, Sigma-Aldrich) in a 1:3 ratio (0.158 g chromium, 1.162 g iodine) into the ampule inside an argon glovebox. We use a pipe cleaner to clean the narrow neck of the ampule and cover the open end with parafilm. We then remove the ampule from the glovebox, quickly secure it in the compression fitting, and open the 3-way valve to the roughing pump. Once the pressure has reached low 10^{-3} Torr, we begin cycles of alternating flushing with argon and opening the valve to the roughing pump until the pressure stabilizes at a minimum value. After 5 cycles, we use a small, open dewar of liquid N_2 to submerge the bottom of the ampule containing the precursors in order to prevent sublimation of I_2. Then, we switch the vacuum pump to the diffusion pump. We allow the pressure to decrease to low 10^{-4} Torr, refilling the N_2 dewar as needed. After reaching this low pressure value, we seal the narrow neck of the ampule using a narrow flame from a H_2/O_2 torch. Finally, while keeping the glass glowing with the torch, we break off the ampule at the sealed neck from the top part connected to the compression fitting by slowly pulling it away.

We use a three-zone furnace and begin by ramping up to an inverted gradient over the course of 2 hours with left (source), center (sink), and right zone setpoints of 25°C, 600°C, and 600°C, respectively. We maintain the inverted gradient conditions for 2.5 hours. Then, over a period of 2 hours, we ramp to the growth conditions with the left zone at 650°C, center zone at 550°C, and right zone at 600°C. We allow the ampule to slowly cool to room temperature after a growth period of 7 days.

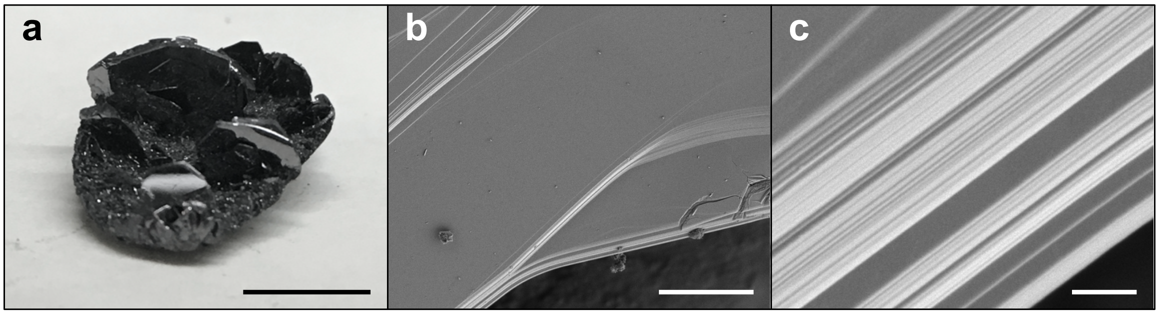

Figure A-2: Bulk CrI_3 crystals. **a.** Platelets of bulk CrI_3 grown in the source zone (scale bar 5 mm). **b.** and **c.** Scanning electron microscope images of a bulk crystal (scale bars 10 µm and 500 nm, respectively).

Crystals form both in the source (shiny hexagonal platelets of several mm in size embedded in solid iodine, Fig. A-2a) and the sink (mm-long ribbon-like flakes). We performed scanning electron microscopy (SEM) on a bulk crystal, shown in Fig. A-2b and c. We used a Zeiss Merlin SEM with an accelerating voltage of 2 kV and type-II secondary electron detection. As we increased magnification along the edge of the crystal (Fig. A-2c), we could easily see the van der Waals nature of the bulk crystal with layers peeling away from one another.

We performed elemental analysis using X-ray photoelectron spectroscopy (XPS) to confirm the stoichiometry of our crystals. We used a PHI VersaProbe II XPS system to extract the atomic concentrations of the Cr $2p$ and I $3d$ orbitals and found them to be in a ratio of approximately 1:3.0096. We also performed powder wide-angle X-ray diffraction and energy-dispersive X-ray microanalysis (see Section 4.7.1).

A.3 Growth of $CrCl_3$

Bulk $CrCl_3$ crystals can also be grown via chemical vapor transport. In our case, we use CVT to recrystallize small flakes of $CrCl_3$ (99.9%, Alfa Aesar). We load 1.0 grams into the ampule inside an argon glovebox and follow the same ampule sealing procedures as described above for CrI_3. We use a three-zone furnace and begin by slowly ramping up to an inverted gradient with left (source), center (sink), and right zone setpoints of 25°C, 700°C, and 700°C, respectively. We ramp up over 1 day and then hold the inverted gradient conditions for another 2 days. Then, we transition over a period of 1 day to the growth conditions with the left zone at 700°C, center zone at 550°C, and right zone at 625°C. After a growth period of 6 days, we slowly ramp down to room temperature over the course of 1 day. The source material fully transports to the middle growth zone, where it recrystallizes into flat platelet crystals (Fig. A-3).

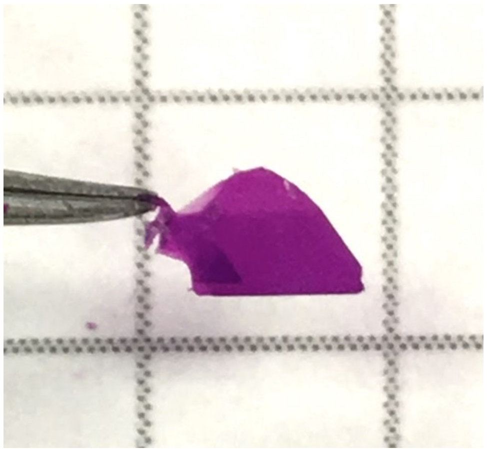

Figure A-3: Bulk $CrCl_3$ single crystal. The grid spacing is 5 mm.

Appendix B

Manipulation of air-sensitive 2D materials

B.1 Glovebox overview

In order to fabricate devices from air-sensitive van der Waals crystals, we use an inert-atmosphere glovebox system to protect the crystals from degradation. The levels of O_2 and H_2O are both maintained at < 0.1 ppm.

The system consists of two gloveboxes connected by a T-chamber to enable transport of materials without exposing them to the outside atmosphere. One box houses a Nikon Eclipse LV-CH 150NA optical microscope with a DS-Ri2 full-frame camera as well as a home-built transfer setup for van der Waals assembly. The other box is equipped with a solvent filter to handle anhydrous solvents and prepare bulk crystal growth reactions.

B.2 Device fabrication

Ampules containing bulk crystals of CrI_3 and $CrCl_3$ are brought into the box and cracked inside to avoid any contact with the air. We then use tweezers to select individual bulk crystals for exfoliation.

We use either Scotch tape or PDMS sheets (WF-30-X0 films from Gel-Pak) to mechanically exfoliate the crystal onto SiO_2/Si substrates. For optimal optical contrast in the few-layer limit of CrX_3, we use either 285 nm SiO_2 thickness and optical filtering (see Sec. 4.7.3) or 90 nm SiO_2 thickness. Once we have identified a desired flake using optical contrast analysis of images taken on the Nikon microscope, we use the dry transfer method to pick up flakes with the transfer setup inside the glovebox.

Since fabrication outside of the box would lead to degradation of our air-sensitive flakes, we carefully design our device geometries to require no post-transfer fabrication steps. For example, we use pre-defined bottom metallic electrodes fabricated using electron-beam lithography and either electron-beam or thermal evaporation for contacting the narrow graphite strips in our magnetic tunnel junctions of CrX_3. We also mount the chip in a 44-pin leadless chip carrier and wirebond prior to van der Waals assembly inside the box.

Once the stack has been assembled using the PC slide on the transfer setup, we remove the polycarbonate residue inside the other glovebox containing a solvent filter. We immerse the entire chip carrier in anhydrous chloroform for several rounds of 30 second soaks to remove as much residue as possible without degrading the sensitive flake.

B.3 Sealing samples

Completely sandwiching air-sensitive flakes in top and bottom BN is an effective approach to protect from degradation. However, sometimes the flake is not fully encapsulated due to geometric constraints, providing opportunities for water and oxygen to leak into the heterostructure and degrade the flake. Therefore, we use two different methods for sealing samples and devices to bring them out of the glovebox. First, we employ a bag sealing method for shipping samples to collaborators at other institutions. We use an impulse bag sealer (ULINE) to completely seal polyethylene bags containing our samples. We also include silica gel desiccant packets to absorb any moisture that may leak inside the argon-filled bags over time.

Second, we employ a coverslip sealing technique to protect our wirebonded devices from ambient conditions in the short time between removal from the glovebox and loading into a cryostat. After removing PC residue, we place the chip carrier on the sample stage of the transfer setup. We heat the stage to 120°C and carefully line the rim of the chip carrier with the adhesive Crystalbond 509 (Ted Pella). This material is solid at room temperature but begins to flow at approximately 120°C. We then allow the stage to cool to 40°C. Next, we position a 15x15 mm glass coverslip over the chip carrier to cover its entire top surface. Finally, we heat up the stage to 120°C for a second time to allow the Crystalbond to melt again, effectively hermetically sealing the device in an argon environment upon cooling. One caveat of this method is that vacuum pumping inside the cryostat usually breaks the seal and removes the cover slip. Therefore, venting the device after measurement may lead to air exposure and flake degradation in a subsequent cooldown.

Bibliography

[1] K. S. Novoselov, A. K. Geim, S. V. Morozov, D. Jiang, Y. Zhang, S. V. Dubonos, I. V. Grigorieva, and A. A. Firsov. Electric field effect in atomically thin carbon films. *Science*, 306(5696):666–669, 2004.

[2] Y. Zhang, Y.-W. Tan, H. L. Stormer, and P. Kim. Experimental observation of the quantum Hall effect and Berry's phase in graphene. *Nature*, 438:201–204, 2005.

[3] C. R. Dean, A. F. Young, I. Meric, C. Lee, L. Wang, S. Sorgenfrei, K. Watanabe, T. Taniguchi, P. Kim, K. L. Shepard, and J. Hone. Boron nitride substrates for high-quality graphene electronics. *Nat. Nanotechnol.*, 5:722–726, 2010.

[4] K. F. Mak, C. Lee, J. Hone, J. Shan, and T. F. Heinz. Atomically thin MoS_2: A new direct-gap semiconductor. *Phys. Rev. Lett.*, 105:136805, 2010.

[5] H. Steinberg, D. R. Gardner, Y. S. Lee, and P. Jarillo-Herrero. Surface state transport and ambipolar electric field effect in Bi_2Se_3 nanodevices. *Nano Lett.*, 10(12):5032–5036, 2010.

[6] X. Xi, Z. Wang, W. Zhao, J.-H. Park, K. T. Law, H. Berger, L. Forró, J. Shan, and K. F. Mak. Ising pairing in superconducting $NbSe_2$. *Nat. Phys.*, 12:139–143, 2016.

[7] B. Huang, G. Clark, E. Navarro-Moratalla, D. R. Klein, R. Cheng, K. L. Seyler, D. Zhong, E. Schmidgall, M. A. McGuire, D. H. Cobden, W. Yao, D. Xiao, P. Jarillo-Herrero, and X. Xu. Layer-dependent ferromagnetism in a van der Waals crystal down to the monolayer limit. *Nature*, 546(7657):270–273, 2017.

[8] C. Gong, L. Li, Z. Li, H. Ji, A. Stern, Y. Xia, T. Cao, W. Bao, C. Wang, Y. Wang, Z. Q. Qiu, R. J. Cava, S. G. Louie, J. Xia, and X. Zhang. Discovery of intrinsic ferromagnetism in two-dimensional van der Waals crystals. *Nature*, 546:265–269, 2017.

[9] Y. Deng, Y. Yu, Y. Song, J. Zhang, N. Z. Wang, Z. Sun, Y. Yi, Y. Z. Wu, S. Wu, J. Zhu, J. Wang, X. H. Chen, and Y. Zhang. Gate-tunable room-temperature ferromagnetism in two-dimensional Fe_3GeTe_2. *Nature*, 563:94–99, 2018.

[10] N. Mounet, M. Gibertini, P. Schwaller, D. Campil, A. Merkys, A. Marrazzo, T. Sohier, I. E. Castelli, A. Cepellotti, G. Pizzi, and N. Marzari. Two-dimensional materials from high-throughput computational exfoliation of experimentally known compounds. *Nat. Nanotechnol.*, 13:246–252, 2018.

[11] V. Fatemi, S. Wu, Y. Cao, L. Bretheau, Q. D. Gibson, K. Watanabe, T. Taniguchi, R. J. Cava, and P. Jarillo-Herrero. Electrically tunable low-density superconductivity in a monolayer topological insulator. *Science*, 362:926–929, 2018.

[12] S. Wu, V. Fatemi, Q. D. Gibson, K. Watanabe, T. Taniguchi, R. J. Cava, and P. Jarillo-Herrero. Observation of the quantum spin Hall effect up to 100 kelvin in a monolayer crystal. *Science*, 359(6371):76–79, 2018.

[13] D. R. Klein, D. MacNeill, Q. Song, D. T. Larson, S. Fang, M. Xu, R. A. Ribeiro, P. C. Canfield, E. Kaxiras, R. Comin, and P. Jarillo-Herrero. Enhancement of interlayer exchange in an ultrathin two-dimensional magnet. *Nat. Phys.*, 15:1255–1260, 2019.

[14] Y. Zhang, T.-T. Tang, C. Girit, Z. Hao, M. C. Martin, A. Zettl, M. F. Crommie, Y. R. Shen, and F. Wang. Direct observation of a widely tunable bandgap in bilayer graphene. *Nature*, 459:820–823, 2009.

[15] A. Avsar, J. Y. Tan, T. Taychatanapat, J. Balakrishnan, G. K. W. Koon, Y. Yeo, J. Lahiri, A. Carvalho, A. S. Rodin, E. C. T. O'Farrell, G. Eda, A. H. Castro Neto, and B. Özyilmaz. Spin-orbit proximity effect in graphene. *Nat. Commun.*, 5:4875, 2014.

[16] Z. Wang, D.-K. Ki, H. Chen, H. Berger, A. H. MacDonald, and A. F. Morpurgo. Strong interface-induced spin–orbit interaction in graphene on WS_2. *Nat. Commun.*, 6:8339, 2015.

[17] Z. Wang, C. Tang, R. Sachs, Y. Barlas, and J. Shi. Proximity-induced ferromagnetism in graphene revealed by the anomalous Hall effect. *Phys. Rev. Lett.*, 114:016603, 2015.

[18] P. Wei, S. Lee, F. Lemaitre, L. Pinel, D. Cutaia, W. Cha, F. Katmis, Y. Zhu, D. Heiman, J. Hone, J. S. Moodera, and C.-T. Chen. Strong interfacial exchange field in the graphene/EuS heterostructure. *Nat. Mater.*, 15:711–716, 2016.

[19] D. Zhong, K. L. Seyler, X. Linpeng, R. Cheng, N. Sivadas, B. Huang, E. Schmidgall, T. Taniguchi, K. Watanabe, M. A. McGuire, W. Yao, D. Xiao, K. C. Fu, and X. Xu. Van der Waals engineering of ferromagnetic semiconductor heterostructures for spin and valleytronics. *Sci. Adv.*, 3(5):e1603113, 2017.

[20] C. R. Dean, L. Wang, P. Maher, C. Forsythe, F. Ghahari, Y. Gao, J. Katoch, M. Ishigami, P. Moon, M. Koshino, T. Taniguchi, K. Watanabe, K. L. Shepard, J. Hone, and P. Kim. Hofstadter's butterfly and the fractal quantum Hall effect in moiré superlattices. *Nature*, 497:598–602, 2013.

[21] B. Hunt, J. D. Sanchez-Yamagishi, A. F. Young, M. Yankowitz, B. J. LeRoy, K. Watanabe, T. Taniguchi, P. Moon, M. Koshino, P. Jarillo-Herrero, and R. C. Ashoori. Massive Dirac fermions and Hofstadter butterfly in a van der Waals heterostructure. *Science*, 340(6139):1427–1430, 2013.

[22] Y. Cao, V. Fatemi, S. Fang, K. Watanabe, T. Taniguchi, E. Kaxiras, and P. Jarillo-Herrero. Unconventional superconductivity in magic-angle graphene superlattices. *Nature*, 556:43–50, 2018.

[23] Y. Cao, V. Fatemi, A. Demir, S. Fang, S. L. Tomarken, J. Y. Luo, J. D. Sanchez-Yamagishi, K. Watanabe, T. Taniguchi, E. Kaxiras, R. C. Ashoori, and P. Jarillo-Herrero. Correlated insulator behaviour at half-filling in magic-angle graphene superlattices. *Nature*, 556:80–84, 2018.

[24] G. Chen, L. Jiang, S. Wu, B. Lyu, H. Li, B. L. Chittari, K. Watanabe, T. Taniguchi, Z. Shi, J. Jung, Y. Zhang, and F. Wang. Evidence of a gate-tunable Mott insulator in a trilayer graphene moir$'e$ superlattice. *Nat. Phys.*, 15:237–241, 2019.

[25] G. Chen, A. L. Sharpe, P. Gallagher, I. T. Rosen, E. J. Fox, L. Jiang, B. Lyu, H. Li, K. Watanabe, T. Taniguchi, J. Jung, Z. Shi, D. Goldhaber-Gordon, Y. Zhang, and F. Wang. Signatures of tunable superconductivity in a trilayer graphene moir$'e$ superlattice. *Nature*, 572:215–219, 2019.

[26] A. L. Sharpe, E. J. Fox, A. W. Barnard, J. Finney, K. Watanabe, T. Taniguchi, M. A. Kastner, and D. Goldhaber-Gordon. Emergent ferromagnetism near three-quarters filling in twisted bilayer graphene. *Science*, 365(6453):605–608, 2019.

[27] G. Chen, A. L. Sharpe, E. J. Fox, Y.-H. Zhang, S. Wang, L. Jiang, B. Lyu, H. Li, K. Watanabe, T. Taniguchi, Z. Shi, T. Senthil, D. Goldhaber-Gordon, Y. Zhang, and F. Wang. Tunable correlated Chern insulator and ferromagnetism in a moir$'e$ superlattice. *Nature*, 579:56–61, 2020.

[28] M. Serlin, C. L. Tschirhart, H. Polshyn, Y. Zhang, J. Zhu, K. Watanabe, T. Taniguchi, L. Balents, and A. F. Young. Intrinsic quantized anomalous Hall effect in a moiré heterostructure. *Science*, 367:900–903, 2020.

[29] H. Polshyn, J. Zhu, M. A. Kumar, Y. Zhang, F. Yang, C. L. Tschirhart, M. Serlin, K. Watanabe, T. Taniguchi, A. H. MacDonald, and A. F. Young. Electrical switching of magnetic order in an orbital Chern insulator. *Nature*, 588:66–70, 2020.

[30] P. Blake, E. W. Hill, A. H. Castro Neto, K. S. Novoselov, D. Jiang, R. Yang, T. J. Booth, and A. K. Geim. Making graphene visible. *Appl. Phys. Lett.*, 91:063124, 2007.

[31] L. Wang, I. Meric, P. Y. Huang, Q. Gao, Y. Gao, H. Tran, T. Taniguchi, K. Watanabe, L. M. Campos, D. A. Muller, J. Guo, P. Kim, J. Hone, K. L. Shepard, and C. R. Dean. One-dimensional electrical contact to a two-dimensional material. *Science*, 342:614–617, 2013.

[32] A. H. Edwards. Interaction of H and H_2 with the silicon dangling orbital at the $< 1\ 1\ 1 >$ Si/SiO_2 interface. *Phys. Rev. B*, 44(4):1832–1838, 1991.

[33] R. Decker, Y. Wang, V. W. Brar, W. Regan, H.-Z. Tsai, Q. Wu, W. Gannett, A. Zettl, and M. F. Crommie. Local electronic properties of graphene on a BN substrate via scanning tunneling microscopy. *Nano Lett.*, 11(6):2291–2295, 2011.

[34] C.-X. Liu, S.-C. Zhang, and X.-L. Qi. The quantum anomalous Hall effect: Theory and experiment. *Annu. Rev. Condens. Matter Phys.*, 7:301–321, 2016.

[35] A. Kitaev. Anyons in an exactly solved model and beyond. *Ann. Phys.*, 321(1):2–111, 2006.

[36] S. Das Sarma, M. Freedman, and C. Nayak. Majorana zero modes and topological quantum computation. *npj Quantum Inf.*, 1:15001, 2015.

[37] A. H. MacDonald, P. Schiffer, and N. Samarth. Ferromagnetic semiconductors: moving beyond (Ga,Mn)As. *Nat. Mater.*, 4:195–202, 2005.

[38] C. Gong and X. Zhang. Two-dimensional magnetic crystals and emergent heterostructure devices. *Science*, 363(6428):eaav4450, 2019.

[39] K. Hejazi, Z.-X. Luo, and L. Balents. Noncollinear phases in moiré magnets. *Proc. Natl. Acad. Sci.*, 117:10721–10726, 2020.

[40] N. D. Mermin and H. Wagner. Absence of ferromagnetism or antiferromagnetism in one- or two-dimensional isotropic Heisenberg models. *Phys. Rev. Lett.*, 17:1133, 1966.

[41] M. A. McGuire, H. Dixit, V. R. Cooper, and B. C. Sales. Coupling of crystal structure and magnetism in the layered, ferromagnetic insulator CrI_3. *Chem. Mater.*, 27:612–620, 2015.

[42] J. F. Dillon and C. E. Olson. Magnetization, resonance, and optical properties of the ferromagnet CrI_3. *J. Appl. Phys*, 36(3):1259–1260, 1965.

[43] J.-U. Lee, S. Lee, J. H. Ryoo, S. Kang, T. Y. Kim, P. Kim, C.-H. Park, J.-G. Park, and H. Cheong. Ising-type magnetic ordering in atomically thin $FePS_3$. *Nano Lett.*, 16:7433–7438, 2016.

[44] M. A. McGuire. Crystal and magnetic structures in layered, transition metal dihalides and trihalides. *Crystals*, 7(5):121, 2017.

[45] K. S. Burch, D. Mandrus, and J.-G. Park. Magnetism in two-dimensional van der Waals materials. *Nature*, 563:47–52, 2018.

[46] K. F. Mak, J. Shan, and D. C. Ralph. Probing and controlling magnetic states in 2D layered magnetic materials. *Nat. Rev. Phys.*, 1:646–661, 2019.

[47] M. Gibertini, M. Koperski, A. F. Morpurgo, and K. S. Novoselov. Magnetic 2D materials and heterostructures. *Nat. Nanotechnol.*, 14:408–419, 2019.

[48] I. Tsubokawa. On the magnetic properties of a $CrBr_3$ single crystal. *J. Phys. Soc. Jpn.*, 15:1664–1668, 1960.

[49] M. A. McGuire, G. Clark, S. KC, W. M. Chance, Jr. G. E. Jellison, V. R. Cooper, X. Xu, and B. C. Sales. Magnetic behavior and spin-lattice coupling in cleavable van der Waals layered $CrCl_3$ crystals. *Phys. Rev. Mater.*, 1:014001, 2017.

[50] K. W. Plumb, J. P. Clancy, L. J. Sandilands, V. Vijay Shankar, Y. F. Hu, K. S. Burch, Hae-Young Kee, and Young-June Kim. α-$RuCl_3$: A spin-orbit assisted Mott insulator on a honeycomb lattice. *Phys. Rev. B*, 90:041112(R), 2014.

[51] L. Sandilands, Y. Tian, K. W. Plumb, Y.-J. Kim, and K. S. Burch. Scattering continuum and possible fractionalized excitations in α-$RuCl_3$. *Phys. Rev. Lett.*, 114:147201, 2015.

[52] A. Banerjee, C. A. Bridges, J.-Q. Yan, A. A. Aczel, L. Li, M. B. Stone, G. E. Granroth, M. D. Lumsen, Y. Yiu, J. Knolle, S. Bhattacharjee, D. L. Kovrizhin, R. Moessner, D. A. Tennant, D. G. Mandrus, and S. E. Nagler. Proximate Kitaev quantum spin liquid behaviour in a honeycomb magnet. *Nat. Mater.*, 15:733–740, 2016.

[53] J. Nasu, J. Knollle, D. L. Kovrizhin, Y. Motome, and R. Moessner. Fermionic response from fractionalization in an insulating two-dimensional magnet. *Nat. Phys.*, 12:912–915, 2016.

[54] A. Banerjee, J. Yan, J. Knoelle, C. A. Bridges, M. B. Stone, M. D. Lumsden, D. G. Mandrus, D. A. Tennant, R. Moessner, and S. E. Nagler. Neutron scattering in the proximate quantum spin liquid $\alpha-RuCl_3$. *Science*, 356:1055–1059, 2017.

[55] N. Janša, A. Zorko, M. Gomilšek, M. Pregelj, K. W. Krämer, D. Biner, A. Biffin, C. Rüegg, and M. Klanjšek. Observation of two types of fractional excitation in the Kitaev honeycomb magnet. *Nat. Phys.*, 14:786–790, 2018.

[56] Y. Kasahara, T. Ohnishi, Y. Mizukami, O. Tanaka, S. Ma, K. Sugii, N. Kurita, H. Tanaka, J. Nasu, Y. Motome, T. Shibauchi, and Y. Matsuda. Majorana quantization and half-integer thermal quantum Hall effect in a Kitaev spin liquid. *Nature*, 559:227–231, 2018.

[57] S. Son, M. J. Coak, N. Lee, J. Kim, T. Y. Kim, H. Hamidov, H. Cho, C. Liu, D. M. Jarvis, P. A. C. Brown, J. H. Kim, C.-H. Park, D. I. Khomskii, S. S. Saxena, and J.-G. Park. Bulk properties of the van der Waals hard ferromagnet VI_3. *Phys. Rev. B*, 99:041402(R), 2019.

[58] J. W. Cable, M. K. Wilkinson, and E. O. Wollan. Neutron diffraction investigation of antiferromagnetism in $CrCl_3$. *J. Phys. Chem. Solids*, 19:29–34, 1961.

[59] V. Carteaux, G. Ouvrard, J. C. Grenier, and Y. Laligant. Magnetic structure of the new layered ferromagnetic chromium hexatellurosilicate $Cr_2Si_2Te_6$. *J. Magn. Magn. Mater.*, 94:127–133, 1991.

[60] A. Wiedenmann, J. Rossat-Mignod, A. Louisy, R. Brec, and J. Rouxel. Neutron diffraction study of the layered compounds $MnPSe_3$ and $FePSe_3$. *Solid State Commun.*, 40:1067–1072, 1981.

[61] P. A. Joy and S. Vasudevan. Magnetism in the layered transition-metal thiophosphates MPS_3 (M=Mn, Fe, and Ni). *Phys. Rev. B*, 46:5425, 1992.

[62] K. Kim, S. Y. Lim, J.-U. Lee, S. Lee, T. Y. Kim, K. Park, G. S. Jeon, C.-H. Park, J.-G. Park, and H. Cheong. Suppression of magnetic ordering in XXZ-type antiferromagnetic monolayer $NiPS_3$. *Nat. Commun.*, 10:345, 2019.

[63] Z. Fei, T. Palomaki, S. Wu, W. Zhao, X. Cai, B. Sun, P. Nguyen, J. Finney, X. Xu, and D. H. Cobden. Edge conduction in monolayer WTe_2. *Nat. Phys.*, 13:677–682, 2017.

[64] S. Lei, J. Lin, Y. Jia, M. Gray, A. Topp, G. Farahi, S. Klemenz, T. Gao, F. Rodolakis, J. L. McChesney, C. R. Ast, A. Yazdani, K. S. Burch, S. Wu, N. P. Ong, and L. M. Schoop. High mobility in a van der Waals layered antiferromagnetic metal. *Sci. Adv.*, 6(6):eaay6407, 2020.

[65] J. Li, Y. Li, S. Du, Z. Wang, B.-L. Gu, S.-C. Zhang, K. He, W. Duan, and Y. Xu. Intrinsic magnetic topological insulators in van der Waals layered $MnBi_2Te_4$-family materials. *Sci. Adv.*, 5:eaaw5685, 2019.

[66] Y. Deng, Y. Yu, M. Z. Shi, Z. Guo, Z. Xu, J. Wang, X. H. Chen, and Y. Zhang. Quantum anomalous Hall effect in intrinsic magnetic topological insulator $MnBi_2Te_4$. *Science*, 367:895–900, 2020.

[67] C. Liu, Y. Wang, H. Li, Y. Wu, Y. Li, J. Li, K. He, Y. Xu, J. Zhang, and Y. Wang. Robust axion insulator and Chern insulator phases in a two-dimensional antiferromagnetic topological insulator. *Nat. Mater.*, 19:522–527, 2020.

[68] C. Hu, L. Ding, K. N. Gordon, B. Ghosh, H.-J. Tien, H. Li, A. G. Linn, S.-W. Lien, C.-Y. Huang, S. Mackey, J. Liu, P. V. S. Reddy, B. Singh, A. Agarwal, A. Bansil., M. Song, D. Li, S.-Y. Xu, H. Lin, H. Cao, T.-R. Chang,

D. Dessau, and N. Ni. Realization of an intrinsic ferromagnetic topological state in $\mathrm{MnBi_8Te_13}$. *Sci. Adv.*, 6:eaba4275, 2020.

[69] B. Morosin and A. Narath. X-ray diffraction and nuclear quadrupole resonance studies of chromium trichloride. *J. Phys. Chem.*, 40:1958, 1964.

[70] P. W. Anderson. Antiferromagnetism. theory of superexchange interaction. *Phys. Rev.*, 79(2):350–356, 1950.

[71] J. B. Goodenough. Theory of the role of covalence in the perovskite-type manganites $[\mathrm{La},M(\mathrm{II})]\mathrm{MnO_3}$. *Phys. Rev.*, 100(2):564–573, 1955.

[72] J. B. Goodenough. An interpretation of the magnetic properties of the perovskite-type mixed crystals $\mathrm{La}_{1-x}\mathrm{Sr}_x\mathrm{CoO}_{3-\gamma}$. *J. Phys. Chem. Solids*, 6:287–297, 1958.

[73] J. Kanamori. Superexchange interaction and symmetry properties of electron orbitals. *J. Phys. Chem. Solids*, 10:87–98, 1959.

[74] H. Wang, F. Fan, S. Zhu, and H. Wu. Doping enhanced ferromagnetism and induced half-metallicity in $\mathrm{CrI_3}$ monolayer. *Europhys. Lett.*, 114:47001, 2016.

[75] J. L. Lado and J. Fernández-Rossier. On the origin of magnetic anisotropy in two dimensional $\mathrm{CrI_3}$. *2D Mater.*, 4(3):035002, 2017.

[76] C. Xu, J. Feng, H. Xiang, and L. Bellaiche. Interplay between Kitaev interaction and single ion anisotropy in ferromagnetic $\mathrm{CrI_3}$ and $\mathrm{CrGeTe_3}$ monolayers. *NPJ Comput. Mater.*, 4:57, 2018.

[77] L. Chen, J.-H. Chung, B. Gao, T. Chen, M. B. Stone, A. I. Kolesnikov, Q. Huang, and P. Dai. Topological spin excitations in honeycomb ferromagnet $\mathrm{CrI_3}$. *Phys. Rev. X*, 8:041028, 2018.

[78] L. Chen, J.-H. Chung, T. Chen, C. Duan, A. Schneidewind, I. Radelytskyi, D. J. Voneshen, R. A. Ewings, M. B. Stone, A. I. Kolesnikov, B. Winn, S. Chi, R. A. Mole, D. H. Yu, G. Gao, and P. Dai. Magnetic anisotropy in ferromagnetic $\mathrm{CrI_3}$. *Phys. Rev. B*, 101:134418, 2020.

[79] Y. Liu and C. Petrovic. Three-dimensional magnetic critical behavior in $\mathrm{CrI_3}$. *Phys. Rev. B*, 97:014420, 2018.

[80] I. Lee, F. G. Utermohlen, D. Weber, K. Hwang, C. Zhang, J. van Tol, J. E. Goldberger, N. Trivedi, and P. C. Hammel. Fundamental spin interactions underlying the magnetic anisotropy in the Kitaev ferromagnet $\mathrm{CrI_3}$. *Phys. Rev. Lett.*, 124:017201, 2020.

[81] N. Sivadas, S. Okamoto, X. Xu, C. J. Fennie, and D. Xiao. Stacking-dependent magnetism in bilayer $\mathrm{CrI_3}$. *Nano Lett.*, 18(12):7658–7664, 2018.

[82] D. Soriano, C. Cardoso, and J. Fernández-Rossier. Interplay between interlayer exchange and stacking in CrI_3 bilayers. *Solid State Commun.*, 299:113662, 2019.

[83] P. Jiang, C. Wang, D. Chen, Z. Zhong, Z. Yuan, Z.-Y. Lu, and W. Ji. Stacking tunable interlayer magnetism in bilayer CrI_3. *Phys. Rev. B*, 99:144401, 2019.

[84] S. W. Jang, M. Y. Jeong, H. Yoon, S. Ryee, and M. J. Han. Microscopic understanding of magnetic interactions in bilayer CrI_3. *Phys. Rev. Mater.*, 3:031001(R), 2019.

[85] D. MacNeill, J. T. Hou, D. R. Klein, P. Zhang, P. Jarillo-Herrero, and L. Liu. Gigahertz frequency antiferromagnetic resonance and strong magnon-magnon coupling in the layered crystal $CrCl_3$. *Phys. Rev. Lett.*, 123:047204, 2019.

[86] W.-B. Zhang, Q. Qu, P. Zhu, and C.-H. Lam. Robust intrinsic ferromagnetism and half semiconductivity in stable two-dimensional single-layer chromium trihalides. *J. Mater. Chem. C*, 3(48):12457–12468, 2015.

[87] S. Foner. Versatile and sensitive vibrating-sample magnetometer. *Rev. Sci. Instrum.*, 30(7):548–557, 1959.

[88] R. L. Fagaly. Superconducting quantum interference device instruments and applications. *Rev. Sci. Instrum.*, 77:101101, 2006.

[89] M. K. Wilkinson, E. O. Wollan, and W. C. Koehler. Neutron diffraction. *Annu. Rev. Nucl. Sci.*, 11:303–348, 1961.

[90] H. Ebert. Magneto-optical effects in transition metal systems. *Rep. Prog. Phys.*, 59(12):1665–1735, 1996.

[91] K. Sato. Measurement of magneto-optical Kerr effect using piezo-birefringent modulator. *Jpn. J. Appl. Phys.*, 20(12):2403, 1981.

[92] K. L. Seyler, D. Zhong, D. R. Klein, S. Gao, X. Zhang, B. Huang, E. Navarro-Moratalla, L. Yang, D. H. Cobden, M. A. McGuire, W. Yao, D. Xiao, P. Jarillo-Herrero, and X. Xu. Ligand-field helical luminescence in a 2D ferromagnetic insulator. *Nat. Phys.*, 14(3):277–281, 2018.

[93] Z. Zhang, J. Shang, C. Jiang, A. Rasmita, W. Gao, and T. Yu. Direct photoluminescence probing of ferromagnetism in monolayer two-dimensional $CrBr_3$. *Nano Lett.*, 19:3138–3142, 2019.

[94] A. McCreary, J. R. Simpson, T. T. Mai, R. D. McMichael, J. E. Douglas, N. Butch, C. Dennis, R. Valdés Aguilar, and A. R. Hight Walker. Quasi-two-dimensional magnon identification in antiferromagnetic $FePS_3$ via magneto-Raman spectroscopy. *Phys. Rev. B*, 101:064416, 2020.

[95] B. Huang, J. Cenker, X. Zhang, E. L. Ray, T. Song, T. Taniguchi, K. Watanabe, M. A. McGuire, D. Xiao, and X. Xu. Tuning inelastic light scattering via symmetry control in the two-dimensional magnet CrI_3. *Nat. Nanotechnol.*, 15:212–216, 2020.

[96] R. H. Fowler and L. Nordheim. Electron emission in intense electric fields. *Proc. R. Soc. Lond. A*, 119(781):173–181, 1928.

[97] J. G. Simmons. Generalized formula for the electric tunnel effect between similar electrodes separated by a thin insulating film. *J. Appl. Phys.*, 34:1793, 1963.

[98] M. Müller and. Exchange splitting and bias-dependent transport in EuO spin filter tunnel barriers. *Europhys. Lett.*, 88:47006, 2009.

[99] E. Y. Tsymbal and I. Žutić. *Handbook of Spin Transport and Magnetism.* CRC Press, 2012.

[100] J. S. Moodera, X. Hao, G. A. Gibson, and R. Meservey. Electron-spin polarization in tunnel junctions in zero applied field with ferromagnetic EuS barriers. *Phys. Rev. Lett.*, 61:637, 1988.

[101] J. S. Moodera, R. Meservey, and X. Hao. Variation of the electron-spin polarization in EuSe tunnel junctions from zero to near 100% in a magnetic field. *Phys. Rev. Lett.*, 70:853, 1993.

[102] D. C. Worledge and T. H. Geballe. Magnetoresistive double spin filter tunnel junction. *J. Appl. Phys.*, 88:5277–5279, 2000.

[103] Z.-W. Xie and B.-Z. Li. Bias dependence of the tunneling magnetoresistance in double spin-filter junctions. *J. Appl. Phys.*, 93:9111, 2003.

[104] G.-X. Miao, M. Müller, and J. S. Moodera. Magnetoresistance in double spin filter tunnel junctions with nonmagnetic electrodes and its unconventional bias dependence. *Phys. Rev. Lett.*, 102:076601, 2009.

[105] R. C. Jaklevic and J. Lambe. Molecular vibration spectra by electron tunneling. *Phys. Rev. Lett.*, 17:1139, 1966.

[106] D. C. Tsui, R. E. Dietz, and L. R. Walker. Multiple magnon excitation in NiO by electron tunneling. *Phys. Rev. Lett.*, 27:1729, 1971.

[107] S. Jung, M. Park, J. Park, T.-Y. Jeong, H.-J. Kim, K. Watanabe, T. Taniguchi, D. H. Ha, C. Hwang, and Y.-S. Kim. Vibrational properties of *h*-BN and *h*-BN-graphene heterostructures probed by inelastic electron tunneling spectroscopy. *Sci. Rep.*, 5:16642, 2015.

[108] M. A. Reed. Inelastic electron tunneling spectroscopy. *Mater. Today*, 11(11):46–50, 2008.

[109] J. Klein, A. Léger, M. Belin, D. Défourneau, and M. J. L. Sangster. Inelastic-electron-tunneling spectroscopy of metal-insulator-metal junctions. *Phys. Rev. B*, 7:2336, 1973.

[110] D. R. Klein, D. MacNeill, J. L. Lado, D. Soriano, E. Navarro-Moratalla, K. Watanabe, T. Taniguchi, S. Manni, P. Canfield, J. Fernández-Rossier, and P. Jarillo-Herrero. Probing magnetism in 2D van der Waals crystalline insulators via electron tunneling. *Science*, 360(6394):1218–1222, 2018.

[111] T. Song, X. Cai, M. W.-Y. Tu, X. Zhang, B. Huang, N. P. Wilson, K. L. Seyler, L. Zhu, T. Taniguchi, K. Watanabe, M. A. McGuire, D. H. Cobden, D. Xiao, W. Yao, and X. Xu. Giant tunneling magnetoresistance in spin-filter van der Waals heterostructures. *Science*, 360(6394):1214–1218, 2018.

[112] H. H. Kim, B. Yang, T. Patel, F. Sfigakis, C. Li, S. Tian, H. Lei, and A. W. Tsen. One million percent tunnel magnetoresistance in a magnetic van der Waals heterostructure. *Nano Lett.*, 18(8):4885–4890, 2018.

[113] Z. Wang, I. Gutiérrez-Lezama, N. Ubrig, M. Kroner, M. Gibertini, T. Taniguchi, K. Watanabe, A. Imamoğlu, E. Giannini, and A. F. Morpurgo. Very large tunneling magnetoresistance in layered magnetic semiconductor CrI_3. *Nat. Commun.*, 9:2516, 2018.

[114] H. H. Kim, B. Yang, S. Tian, C. Li, G.-X. Miao, H. Li, and A. W. Tsen. Tailored tunnel magnetoresistance response in three ultrathin chromium trihalides. *Nano Lett.*, 19:5739–5745, 2019.

[115] H. H. Kim, B. Yang, S. Li, S. Jiang, C. Jin, Z. Tao, G. Nichols, F. Sfigakis, S. Zhong, C. Li, S. Tian, D. G. Cory, G.-X. Miao, J. Shan, K. F. Mak, H. Lei, K. Sun, L. Zhao, and A. W. Tsen. Evolution of interlayer and intralayer magnetism in three atomically thin chromium trihalides. *Proc. Natl. Acad. Sci.*, 116:11131–11136, 2019.

[116] D. Ghazaryan, M. T. Greenaway, Z. Wang, V. H. Guarochico-Moreira, I. J. Vera-Marun, J. Yin, Y. Liao, S. V. Morozov, O. Kristanovski, A. I. Lichtenstein, M. I. Katsnelson, F. Withers, A. Mishchenko, L. Eaves, A. K. Geim, K. S. Novoselov, and A. Misra. Magnon-assisted tunnelling in van der Waals heterostructures based on $CrBr_3$. *Nat. Electron.*, 1:344–349, 2018.

[117] X. Cai, T. Song, N. P. Wilson, G. Clark, M. He, X. Zhang, T. Taniguchi, K. Watanabe, W. Yao, D. Xiao, M. A. McGuire, D. H. Cobden, and X. Xu. Atomically thin $CrCl_3$: An in-plane layered antiferromagnetic insulator. *Nano Lett.*, 19:3993–3998, 2019.

[118] Z. Wang, M. Gibertini, D. Dumcenco, T. Taniguchi, K. Watanabe, E. Giannini, and A. F. Morpurgo. Determining the phase diagram of atomically thin layered antiferromagnet $crcl_3$. *Nat. Nanotechnol.*, 14:1116–1122, 2019.

[119] S. Jiang, L. Li, Z. Wang, J. Shan, and K. F. Mak. Spin tunnel field-effect transistors based on two-dimensional van der Waals heterostructures. *Nat. Electron.*, 2:159–163, 2019.

[120] F. Casola, T. van der Sar, and A. Yacoby. Probing condensed matter physics with magnetometry based on nitrogen-vacancy centres in diamond. *Nat. Rev. Mater.*, 13:17088, 2018.

[121] I. Lovchinsky, J. D. Sanchez-Yamagishi, E. K. Urbach, S. Choi, S. Fang, T. I. Andersen, K. Watanabe, T. Taniguchi, A. Bylinskii, E. Kaxiras, P. Kim, H. Park, and M. D. Lukin. Magnetic resonance spectroscopy of an atomically thin material using a single-spin qubit. *Science*, 355(6324):503–507, 2017.

[122] C. Du, T. van der Sar, T. X. Zhou, P. Upadhyaya, F. Casola, H. Zhang, M. C. Onbasli, C. A. Ross, R. L. Walsworth, Y. Tserkovnyak, and A. Yacoby. Control and local measurement of the spin chemical potential in a magnetic insulator. *Science*, 357(6347):195–198, 2017.

[123] L. Thiel, Z. Wang, M. A. Tschudin, D. Rohner, I. Gutiérrez-Lezama, N. Ubrig, M. Gibertini, E. Giannini, A. F. Morpurgo, and P. Maletinsky. Probing magnetism in 2D materials at the nanoscale with single-spin microscopy. *Science*, 364(6444):973–976, 2019.

[124] M. Kim, P. Kumaravadivel, J. Birkbeck, W. Kuang, S. G. Xu, D. G. Hopkinson, J. Knolle, P. A. McClarty, A. I. Berdyugin, M. Ben Shalom, R. V. Gorbachev, S. J. Haigh, S. Liu, J. H. Edgar, K. S. Novoselov, I. V. Grigorieva, and A. K. Geim. Micromagnetometry of two-dimensional ferromagnets. *Nat. Electron.*, 2:457–463, 2019.

[125] R. Wiesendanger. Spin mapping at the nanoscale and atomic scale. *Rev. Mod. Phys.*, 81:1495, 2009.

[126] U. Hartmann. Magnetic force microscopy. *Annu. Rev. Mater. Sci.*, 29:53–87, 1999.

[127] D. A. Bozhko, A. A. Serga, P. Clausen, V. I. Vasyuchka, F. Heussner, G. A. Melkov, A. Pomyalov, V. S. L'vov, and B. Hillebrands. Supercurrent in a room-temperature Bose–Einstein magnon condensate. *Nat. Phys.*, 12:1057–1062, 2016.

[128] K. An, K. S. Olsson, A. Weathers, S. Sullivan, X. Chen, X. Li, L. G. Marshall, X. Ma, N. Klimovich, J. Zhou, L. Shi, and X. Li. Magnons and phonons optically driven out of local equilibrium in a magnetic insulator. *Phys. Rev. Lett.*, 117:107202, 2016.

[129] X. Xu, W. Yao, D. Xiao, and T. F. Heinz. Spin and pseudospins in layered transition metal dichalcogenides. *Nat. Phys.*, 10:343–350, 2015.

[130] Y. Saito, Y. Nakamura, M. S. Bahramy, Y. Kohama, J. Ye, Y. Kasahara, Y. Nakagawa, M. Onga, M. Tokunaga, T. Nojima, Y. Yanase, and Y. Iwasa. Superconductivity protected by spin–valley locking in ion-gated MoS_2. *Nat. Phys.*, 12:144–149, 2016.

[131] J. M. Lu, O. Zheliuk, I. Leermakers, N. F. Q. Yuan, U. Zeitler, K. T. Law, and J. T. Ye. Evidence for two-dimensional Ising superconductivity in gated MoS_2. *Science*, 350(6266):1353–1357, 2015.

[132] A. W. Tsen, B. Hunt, Y. D. Kim, Z. J. Yuan, S. Jia, R. J. Cava, J. Hone, P. Kim, C. R. Dean, and A. N. Pasupathy. Nature of the quantum metal in a two-dimensional crystalline superconductor. *Nat. Phys.*, 12:208–212, 2016.

[133] Y. Yu, F. Yang, X. F. Lu, Y. J. Yan, Y.-H. Cho, L. Ma, X. Niu, S. Kim, Y.-W. Son, D. Feng, S. Li, S.-W. Cheong, X. H. Chen, and Y. Zhang. Gate-tunable phase transitions in thin flakes of 1T-TaS_2. *Nat. Nanotechnol.*, 10:270–276, 2015.

[134] X. Qiana nd J. Kiu, L. Fu, and J. Li. Quantum spin Hall effect in two-dimensional transition metal dichalcogenides. *Science*, 346(6215):1344–1347, 2014.

[135] X. Li and J. Yang. $CrXTe_3$ (X = Si, Ge) nanosheets: two dimensional intrinsic ferromagnetic semiconductors. *J. Mater. Chem. C*, 2:7071–7076, 2014.

[136] M.-W. Lin, H. L. Zhuang, J. Yan, T. Z. Ward, A. A. Puretsky, C. M. Rouleau, Z. Gai, L. Liang, V. Meunier, B. G. Sumpter, P. Ganesh, P. R. C. Kent, D. B. Geohegan, D. G. Mandrus, and K. Xiao. Ultrathin nanosheets of $CrSiTe_3$: a semiconducting two-dimensional ferromagnetic material. *J. Mater. Chem. C*, 4:315–322, 2016.

[137] N. Sivadas, M. W. Daniels, R. H. Swendsen, S. Okamoto, and D. Xiao. Magnetic ground state of semiconducting transition-metal trichalcogenide monolayers. *Phys. Rev. B*, 91:235425, 2015.

[138] A. Soumyanarayanan, N. Reyren, A. Fert, and C. Panagopoulos. Emergent phenomena induced by spin–orbit coupling at surfaces and interfaces. *Nature*, 539:509–517, 2016.

[139] K. S. Novoselov, E. McCann, S. V. Morozov, V. I. Fal'ko, M. I. Katsnelson, U. Zeitler, D. Jiang, F. Schedin, and A. K. Geim. Unconventional quantum Hall effect and Berry's phase of 2π in bilayer graphene. *Nat. Phys.*, 2:177–180, 2006.

[140] A. Splendiani, L. Sun, Y. Zhang, T. Li, J. Kim, C.-Y. Chim, G. Galli, and F. Wang. Emerging photoluminescence in monolayer MoS_2. *Nano Lett.*, 10(4):1271–1275, 2010.

[141] E. Stryjewski and N. Giordano. Metamagnetism. *Adv. Phys.*, 26(5):487–650, 1977.

[142] F. Huang, M. T. Kief, G. J. Mankey, and R. F. Willis. Magnetism in the few-monolayers limit: A surface magneto-optic Kerr-effect study of the magnetic behavior of ultrathin films of Co, Ni, and Co-Ni alloys on Cu(100) and Cu(111). *Phys. Rev. B*, 49:3962, 1994.

[143] C. H. Back, Ch. Würsch, A. Vaterlaus, U. Ramsperger, U. Maier, and D. Pescia. Experimental confirmation of universality for a phase transition in two dimensions. *Nature*, 378:597–600, 1995.

[144] H.-J. Elmers, J. Hauschild, and U. Gradmann. Critical behavior of the uniaxial ferromagnetic monolayer Fe(110) on W(110). *Phys. Rev. B*, 54:15224, 1996.

[145] L. J. De Jongh and A. R. Miedema. Experiments on simple magnetic model systems. *Adv. Phys.*, 50(8):947–1170, 2001.

[146] V. Carteaux, F. Moussa, and M. Spiesser. 2d Ising-like ferromagnetic behaviour for the lamellar Cr_2.

[147] B. Sachs, T. O. Wehling, K. S. Novoselov, A. I. Lichtenstein, and M. I. Katsnelson. Ferromagnetic two-dimensional crystals: Single layers of K_2CuF_4. *Phys. Rev. B*, 88:201402(R), 2013.

[148] X. Wang, K. Du, Y. Y. F. Liu, P. Hu, J. Zhang, Q. Zhang, M. H. S. Owen, X. Lu, C. K. Gan, P. Sengupta, C. Kloc, and Q. Xiong. Raman spectroscopy of atomically thin two-dimensional magnetic iron phosphorus trisulfide (feps3) crystals. *2D Mater.*, 3(3):031009, 2016.

[149] Y. Tian, M. J. Gray, H. Ji, R. J. Cava, and K. S. Burch. Magneto-elastic coupling in a potential ferromagnetic 2D atomic crystal. *2D Mater.*, 3(2):025035, 2016.

[150] D. Sander. The magnetic anisotropy and spin reorientation of nanostructures and nanoscale films. *J. Phys. Condens. Matter*, 16(20):R603, 2004.

[151] A. R. Beal, H. P. Hughes, and W. Y. Liang. The reflectivity spectra of some group VA transition metal dichalcogenides. *J. Phys. C*, 8(24):4236, 1975.

[152] A. Castellanos-Gomez, E. Navarro-Moratalla, G. Mokry, J. Quereda, E. Pinilla-Cienfuegos, N. Agraït, H. S. J. van der Zant, E. Coronado, G. A. Steele, and G. Rubio-Bollinger. Fast and reliable identification of atomically thin layers of $TaSe_2$ crystals. *Nano Res.*, 6(3):191–199, 2013.

[153] P. M. Grant and G. B. Street. Optical properties of chromium trihalides in the region 1-11 eV. *Bull. Am. Phys. Soc. II*, 13:3, 1968.

[154] C. M. Herzinger, B. Johs, W. A. McGahan, J. A. Woollam, and W. Paulson. Ellipsometric determination of optical constants for silicon and thermally grown silicon dioxide via a multi-sample, multi-wavelength, multi-angle investigation. *J. Appl. Phys.*, 83:3323, 1998.

[155] B. Huang, G. Clark, D. R. Klein, D. MacNeill, E. Navarro-Moratalla, K. L. Seyler, N. Wilson, M. A. McGuire, D. H. Cobden, D. Xiao, W. Yao, P. Jarillo-Herrero, and X. Xu. Electrical control of 2D magnetism in bilayer $\mathrm{CrI_3}$. *Nat. Nanotechnol.*, 13(7):544–548, 2018.

[156] D. Chiba, S. Fukami, K. Shimamura, N. Ishiwata, K. Kobayashi, and T. Ono. Electrical control of the ferromagnetic phase transition in cobalt at room temperature. *Nat. Mater.*, 10:853–856, 2011.

[157] D. Chiba, M. Sawicki, Y. Nishitani, Y. Kanatani, F. Matsukura, and H. Ohno. Magnetization vector manipulation by electric fields. *Nature*, 455:515–518, 2008.

[158] W. Eerenstein, N. D. Mathur, and J. F. Scott. Multiferroic and magnetoelectric materials. *Nature*, 442:759–765, 2006.

[159] F. Matsukura, Y. Tokura, and H. Ohno. Control of magnetism by electric fields. *Nat. Nanotechnol.*, 10:209–220, 2015.

[160] G. A. Prinz. Magnetoelectronics. *Science*, 282(5394):1660–1663, 1998.

[161] Y.-H. Chu, L. W. Martin, M. B. Holcomb, M. Gajek, S.-J. Han, Q. He, N. Balke, C.-H. Yang, D. Lee, W. Hu, Q. Zhan, P.-L. Yang, A. Fraile-Rodríguez, A. Scholl, S. X. Wang, and R. Ramesh. Electric-field control of local ferromagnetism using a magnetoelectric multiferroic. *Nat. Mater.*, 7:478–482, 2008.

[162] H. Ohno, D. Chiba, F. Matsukura, T. Omiya, E. Abe, T. Dietl, Y. Ohno, and K. Ohtani. Electric-field control of magnetism. *Nature*, 408:944–946, 2000.

[163] T. Dietl, H. Ohno, F. Matsukura, J. Cibert, and D. Ferrand. Zener model description of ferromagnetism in zinc-blende magnetic semiconductors. *Science*, 287(5455):1019–1022, 2000.

[164] B. Zhou, Y. Wang, G. B. Osterhoudt, P. Lampen-Kelley, D. Mandrus, R. He, K. S. Burch, and E. A. Henriksen. Possible structural transformation and enhanced magnetic fluctuations in exfoliated $\alpha-\mathrm{RuCl_3}$. *J. Phys. Chem. Solids*, 128:291–295, 2019.

[165] D. J. O'Hara, T. Zhu, A. H. Trout, A. S. Ahmed, Y. K. Luo, C. H. Lee, M. R. Brenner, S. Rajan, J. A. Gupta, D. W. McComb, and R. K. Kawakami. Room temperature intrinsic ferromagnetism in epitaxial manganese selenide films in the monolayer limit. *Nano Lett.*, 18(5):3125–3131, 2018.

[166] W. Xing, Y. Chen, P. M. Odenthal, X. Zhang, W. Yuan, T. Su, Q. Song, T. Wang, J. Zhong, S. Jia, X. C. Xie, Y. Li, and W. Han. Electric field effect in multilayer $Cr_2Ge_2Te_6$: a ferromagnetic 2D material. *2D Mater.*, 4(2):024009, 2017.

[167] T. Taychatanapat, K. Watanabe, T. Taniguchi, and P. Jarillo-Herrero. Quantum Hall effect and Landau-level crossing of Dirac fermions in trilayer graphene. *Nat. Phys.*, 7:621–625, 2011.

[168] M. Weisheit, S. Fähler, A. Marty, Y. Souche, C. Poinsignon, and D. Givord. Electric field-induced modification of magnetism in thin-film ferromagnets. *Science*, 315(5810):349–351, 2007.

[169] C.-G. Duan, J. P. Velev, R. F. Sabirianov, Z. Zhu, J. Chu, S. S. Jaswal, and E. Y. Tsymbal. Surface magnetoelectric effect in ferromagnetic metal films. *Phys. Rev. Lett.*, 101:137201, 2008.

[170] K. Nakamura, R. Shimabukuro, Y. Fujiwara, T. Akiyama, T. Ito, and A. J. Freeman. Giant modification of the magnetocrystalline anisotropy in transition-metal monolayers by an external electric field. *Phys. Rev. Lett.*, 102:187201, 2009.

[171] A. Schmehl, V. Vaithyanathan, A. Herrnberger, S. Thiel, C. Richter, M. Liberati, T. Heeg, M. Röckerath, L. F. Kourkoutis, S. Mühlbauer, P. Böni, D. A. Muller, Y. Barash, J. Schubert, Y. Idzerda, J. Mannhart, and D. G. Schlom. Epitaxial integration of the highly spin-polarized ferromagnetic semiconductor EuO with silicon and GaN. *Nat. Mater.*, 6:882–887, 2007.

[172] T. Mairoser, A. Schmehl, A. Melville, T. Heeg, L. Canella, P. Böni, W. Zander, J. Schubert, D. E. Shai, E. J. Monkman, K. M. Shen, D. G. Schlom, and J. Mannhart. Is there an intrinsic limit to the charge-carrier-induced increase of the Curie temperature of EuO? *Phys. Rev. Lett.*, 105:257206, 2010.

[173] N. Sivadas, S. Okamoto, and D. Xiao. Gate-controllable magneto-optic Kerr effect in layered collinear antiferromagnets. *Phys. Rev. Lett.*, 117:267203, 2016.

[174] Z. Gong, G.-B. Liu, H. Yu, D. Xiao, X. Cui, X. Xu, and W. Yao. Magnetoelectric effects and valley-controlled spin quantum gates in transition metal dichalcogenide bilayers. *Nat. Commun.*, 4:2053, 2013.

[175] A. M. Jones, H. Yu, J. S. Ross, P. Klement, N. J. Ghimire, J. Yan, D. G. Mandrus, W. Yao, and X. Xu. Spin–layer locking effects in optical orientation of exciton spin in bilayer WSe_2. *Nat. Phys.*, 10:130–134, 2014.

[176] S. Jiang, L. Li, Z. Wang, K. F. Mak, and J. Shan. Controlling magnetism in 2D CrI_3 by electrostatic doping. *Nat. Nanotechnol.*, 13:549–553, 2018.

[177] S. Jiang, J. Shan, and K. F. Mak. Electric-field switching of two-dimensional van der Waals magnets. *Nat. Mater.*, 17:406–410, 2018.

[178] W.-K. Tse, Z. Qiao, Y. Yao, A. H. MacDonald, and Q. Niu. Quantum anomalous Hall effect in single-layer and bilayer graphene. *Phys. Rev. B*, 83:155447, 2011.

[179] T. Kurumaji, S. Seki, S. Ishiwata, H. Murakawa, Y. Tokunaga, Y. Kaneko, and Y. Tokura. Magnetic-field induced competition of two multiferroic orders in a triangular-lattice helimagnet MnI_2. *Phys. Rev. Lett.*, 106:167206, 2011.

[180] A. R. Mellnik, J. S. Lee, A. Richardella, J. L. Grab, P. J. Mintun, M. H. Fischer, A. Vaezi, A. Manchon, E.-A. Kim, N. Samarth, and D. C. Ralph. Spin-transfer torque generated by a topological insulator. *Nature*, 511:449–451, 2014.

[181] T. Wakamura, H. Akaike, Y. Omori, Y. Niimi, S. Takahashi, A. Fujimaki, S. Maekawa, and Y. Otani. Quasiparticle-mediated spin Hall effect in a superconductor. *Nat. Mater.*, 14:675–678, 2015.

[182] P. Wadley, B. Howells, J. Železný, C. Andrews, V. Hills, R. P. Campion, V. Novák, K. Olejník, F. Maccherozzi, S. S. Dhesi, S. Y. Martin, T. Wagner, J. Wunderlich, F. Freimuth, Y. Mokrousov, J. Kuneš, J. S. Chauhan, M. J. Grzybowski, A. W. Rushforth, K. W. Edmonds, B L. Gallagher, and T. Jungwirth. Electrical switching of an antiferromagnet. *Science*, 351:587–590, 2016.

[183] D. MacNeill, G. M. Stiehl, M. H. D. Guimaraes, R. A. Buhrman, J. Park, and D. C. Ralph. Control of spin-orbit torques through crystal symmetry in WTe_2/ferromagnet bilayers. *Nat. Phys.*, 13:300–305, 2017.

[184] D. MacNeill, G. M. Stiehl, M. H. D. Guimar aes, N. D. Reynolds, R. A. Buhrman, and D. C. Ralph. Thickness dependence of spin-orbit torques generated by WTe_2. *Phys. Rev. B*, 96:054450, 2017.

[185] Q. Shao, G. Yu, Y.-W. Lan, Y. Shi, M.-Y. Li, C. Zheng, X. Zhu, L.-J. Li, P. K. Amiri, and K. L. Wang. Strong Rashba-Edelstein effect-induced spin–orbit torques in monolayer transition metal dichalcogenide/ferromagnet bilayers. *Nano Lett.*, 16(12):7514–7520, 2016.

[186] T. D. Skinner, K. Olejník, L. K. Cunningham, H. Kurebayashi, R. P. Campion, B. L. Gallagher, T. Jungwirth, and A. J. Ferguson. Complementary spin-Hall and inverse spin-galvanic effect torques in a ferromagnet/semiconductor bilayer. *Nat. Commun.*, 6:6730, 2015.

[187] L. Esaki, P. J. Stiles, and S. von Molnar. Magnetointernal field emission in junctions of magnetic insulators. *Phys. Rev. Lett.*, 19:852, 1967.

[188] L. Vitali, M. A. Schneider, K. Kern, L. Wirtz, and A. Rubio. Phonon and plasmon excitation in inelastic electron tunneling spectroscopy of graphite. *Phys. Rev. B*, 69:121414(R), 2004.

[189] C. F. Hirjibehedin, C. P. Lutz, and A. J. Heinrich. Spin coupling in engineered atomic structures. *Science*, 312:1021–1024, 2006.

[190] A. Spinelli, B. Bryant, F. Delago, J. Fernández-Rossier, and A. F. Otte. Imaging of spin waves in atomically designed nanomagnets. *Nat. Mater.*, 13:782–785, 2014.

[191] K. Yamaguchi. Inelastic electron tunneling due to magnons and phonons of antiferromagnetic layered $MnPSe_3$ semiconductors. *phys. status solidi (b)*, 236(3):634–639, 2003.

[192] A. Narath. Zero-field ^{53}Cr nuclear magnetic resonance in ferromagnetic CrI_3: Renormalized spin-wave and Green's-function analysis. *Phys. Rev.*, 140:A854, 1965.

[193] S. A. Owerre. Dirac magnon nodal loops in quasi-2D quantum magnets. *Sci. Rep.*, 7:6931, 2017.

[194] S. S. Pershoguba, S. Banerjee, J. C. Lashley, J. Park, H. Ågren, G. Aeppli, and A. V. Balatsky. Dirac magnons in honeycomb ferromagnets. *Phys. Rev. X*, 8:011010, 2018.

[195] P. Giannozzi, S. Baroni, N. Bonini, M. Calandra, R. Car, C. Cavazzoni, D. Ceresoli, G. L. Chiarotti, M. Cococcioni, I. Daboll, A. D. Corsol, S. de Gironcoli, S. Fabris, G. Fratesi, R. Gebauer, U. Gerstmann, C. Gougoussis, A. Kokalj, M. Lazzeri, L. Martin-Samos, N. Marzari, F. Mauri, R. Mazzarello, S. Paolini, A. Pasquarello, L. Paulatto, C. Sbraccia, S. Scandolo, G. Sclauzero, A. P. Seitsonen, A. Smogunov, P. Umari, and R. M. Wentzcovitch. QUANTUM ESPRESSO: a modular and open-source software project for quantum simulations of materials. *J. Phys. Condens. Matter*, 21:395502, 2009.

[196] C.-T. Kuo, M. Neumann, K. Balamurugan, H. J. Park, S. Kang, H. W. Shiu, J. H. Kang, B. H. Hong, M. Han, T. W. Noh, and J.-G. Park. Exfoliation and Raman spectroscopic fingerprint of few-layer $NiPS_3$ van der Waals crystals. *Sci. Rep.*, 6:20904, 2016.

[197] A. Narath and H. L. Davis. Spin-wave analysis of the sublattice magnetization behavior of antiferromagnetic and ferromagnetic $CrCl_3$. *Phys. Rev.*, 137:A163, 1965.

[198] B. Kuhlow. Magnetic ordering in $CrCl_3$ at the phase transition. *phys. status solidi (a)*, 72:161, 1982.

[199] X. Hao, J. S. Moodera, and R. Meservey. Spin-filter effect of ferromagnetic europium sulfide tunnel barriers. *Phys. Rev. B*, 42:8235, 1990.

[200] A. Glamazda, P. Lemmens, S.-H. Do, Y. S. Kwon, and K.-Y. Choi. Relation between Kitaev magnetism and structure in $\alpha-RuCl_3$. *Phys. Rev. B*, 95:174429, 2017.

[201] H. B. Cao, A. Banerjee, J.-Q. Yan, C. A. Bridges, M. D. Lumsden, D. G. Mandrus, D. A. Tennant, B. C. Chakoumakos, and S. E. Nagler. Low-temperature crystal and magnetic structure of $\alpha-\mathrm{RuCl}_3$. *Phys. Rev. B*, 93:134423, 2016.

[202] V. M. Bermudez. Unit-cell vibrational spectra of chromium trichoride and chromium tribromide. *Solid State Commun.*, 19(8):693–697, 1976.

[203] D. T. Larson and E. Kaxiras. Raman spectrum of CrI_3: An *ab initio* study. *Phys. Rev. B*, 98:085406, 2018.

[204] Z. Sun, Y. Yi, T. Songa nd G. Clark, B. Huang, Y. Shan, S. Wu, D. Huang, C. Gao, Z. Chen, M. McGuire, T. Cao, D. Xiao, W.-T. Liu, W. Yao, X. Xu, and S. Wu. Giant nonreciprocal second-harmonic generation from antiferromagnetic bilayer CrI_3. *Nature*, 572:497–501, 2019.

[205] T. Song, Z. Fei, M. Yankowitz, Z. Lin, Q. Jiang, K. Hwangbo, Q. Zhang, B. Sun, T. Taniguchi, K. Watanabe, M. A. McGuire, D. Graf, T. Cao, J.-H. Chu, D. H. Cobden, C. R. Dean, D. Xiao, and X. Xu. Switching 2D magnetic states via pressure tuning of layer stacking. *Nat. Mater.*, 18:1298–1302, 2019.

[206] T. Li, S. Jiang, N. Sivadas, Z. Wang, Y. Xu, D. Weber, J. E. Goldberger, K. Watanabe, T. Taniguchi, C. J. Fennie, K. F. Mak, and J. Shan. Pressure-controlled interlayer magnetism in atomically thin CrI_3. *Nat. Mater.*, 18:1303–1308, 2019.

[207] B. Niu, T. Su, B. A. Francisco, S. Ghosh, F. Kargar, X. Huang, M. Lohmann, J. Li, Y. Xu, T. Taniguchi, K. Watanabe, D. Wu, A. Balandin, J. Shi, and Y.-T. Cui. Coexistence of magnetic orders in two-dimensional magnet CrI_3. *Nano Lett.*, 20:553–558, 2020.

[208] W. Chen, Z. Sun, Z. Wang, L. Gu, X. Xu, and S. Wu. Direct observation of van der Waals stacking–dependent interlayer magnetism. *Science*, 366:983–987, 2019.

[209] P. E. Blöchl. Projector augmented-wave method. *Phys. Rev. B*, 50:17953, 1994.

[210] G. Kresse and J. Furthmüller. Efficient iterative schemes for *ab initio* total-energy calculations using a plane-wave basis set. *Phys. Rev. B*, 54:11169, 1996.

[211] G. Kresse and J. Furthmüller. Efficiency of ab-initio total energy calculations for metals and semiconductors using a plane-wave basis set. *Comput. Mater. Sci.*, 6(1):15–50, 1996.

[212] J. P. Perdew and A. Zunger. Self-interaction correction to density-functional approximations for many-electron systems. *Phys. Rev. B*, 23:5048, 1981.

[213] J. P. Perdew, K. Burke, and M. Ernzerhof. Generalized gradient approximation made simple. *Phys. Rev. Lett.*, 77:3865, 1996.

[214] J. Klimeš, D. R. Bowler, and A. Michaelides. Chemical accuracy for the van der Waals density functional. *J. Phys. Condens. Matter*, 22:022201, 2009.

[215] J. Klimeš, D. R. Bowler, and A. Michaelides. Van der Waals density functionals applied to solids. *Phys. Rev. B*, 83:195131, 2011.

[216] M. Dion, H. Rydberg, E. Schröder, D. C. Langreth, and B. I. Lundqvist. Van der Waals density functional for general geometries. *Phys. Rev. Lett.*, 92:246401, 2004.

[217] S. L. Dudarev, G. A. Botton, S. Y. Savrasov, C. J. Humphreys, and A. P. Sutton. Electron-energy-loss spectra and the structural stability of nickel oxide: An LSDA+U study. *Phys. Rev. B*, 57:1505, 1998.

[218] F. Liu, L. You, K. L. Seyler, X. Li, P. Yu, J. Lin, X. Wang, J. Zhou, H. Wang, H. He, S. T. Pantelides, W. Zhou, P. Sharma, X. Xu, P. M. Ajayan, J. Wang, and Z. Liu. Room-temperature ferroelectricity in $CuInP_2S_6$ ultrathin flakes. *Nat. Commun.*, 7:12357, 2016.

[219] Y. Zhou, D. Wu, Y. Zhu, Y. Cho, Q. He, X. Yang, K. Herrera, Z. Chu, Y. Han, M. C. Downer, H. Peng, and K. Lai. Out-of-plane piezoelectricity and ferroelectricity in layered α-In_2Se_3 nanoflakes. *Nano Lett.*, 17:5508–5513, 2017.

[220] Z. Fei, W. Zhao, T. A. Palomaki, B. Sun, M. K. Miller, Z. Zhao, J. Yan, X. Xu, and D. H. Cobden. Ferroelectric switching of a two-dimensional metal. *Nature*, 560:336–339, 2018.

[221] C. Gong, E. M. Kim, Y. Wang, G. Lee, and X. Zhang. Multiferroicity in atomic van der Waals heterostructures. *Nat. Commun.*, 10:2657, 2019.

[222] D. Edelberg, D. Rhodes, A. Kerelsky, B. Kim, J. Wang, A. Zangiabadi, C. Kim, A. Abhinandan, J. Ardelean, M. Scully, D. Scullion, L. Embon, R. Zu, E. J. G. Santos, L. Balicas, C. Marianetti, K. Barmak, X. Zhu, J. Hone, and A. N. Pasupathy. Approaching the intrinsic limit in transition metal diselenides via point defect control. *Nano Lett.*, 19:4371–4379, 2019.

[223] A. Devarakonda, H. Inoue, S. Fang, C. Ozsoy-Keskinbora, T. Suzuki, M. Kriener, L. Fu, E. Kaxiras, D. C. Bell, and J. G. Checkelsky. Clean 2D superconductivity bulk van der Waals superlattice. *Science*, 370:231–236, 2020.

[224] N. Bultinck, S. Chatterjee, and M. P. Zaletel. Mechanism for anomalous Hall ferromagnetism in twisted bilayer graphene. *Phys. Rev. Lett.*, 124:166601, 2020.

[225] C. Repellin, Z. Dong, Y.-H. Zhang, and T. Senthil. Ferromagnetism in narrow bands of moiré superlattices. *Phys. Rev. Lett.*, 124:187601, 2020.

[226] Y. Park., B. L. Chittari, and J. Jung. Gate-tunable topological flat bands in twisted monolayer-bilayer graphene. *Phys. Rev. B*, 102:035411, 2020.

[227] C. Repellin and T. Senthil. Chern bands of twisted bilayer graphene: Fractional Chern insulators and spin phase transition. *Phys. Rev. Research*, 2:023238, 2020.

[228] S. Zhang, R. Wang, X. Wang, B. Wei, B. Chen, H. Wang, G. Shi, F. Wang, B. Jia, Y. Ouyang, F. Xie, F. Fei, M. Zhang, X. Wang, D. Wu, X. Wan, F. Song, H. Zhang, and B. Wang. Experimental observation of the gate-controlled reversal of the anomalous Hall effect in the intrinsic magnetic topological insulator $\mathrm{MnBi_2Te_4}$ device. *Nano Lett.*, 20:709–714, 2020.

[229] H. Fu, C.-X. Liu, and B. Yan. Exchange bias and quantum anomalous Hall effect in the $\mathrm{MnBi_2Te_4/CrI_3}$ heterostructure. *Sci. Adv.*, 6:eaaz0948, 2020.

[230] Z. Wang, D. Sapkota, T. Taniguchi, K. Watanabe, D. Mandrus, and A. F. Morpurgo. Tunneling spin valves based on $\mathrm{Fe_3GeTe_2/hBN/Fe_3GeTe_2}$ van der Waals heterostructures. *Nano Lett.*, 18:4303–4308, 2018.

[231] Q. Sun and N. Kioussis. Prediction of manganese trihalides as two-dimensional Dirac half-metals. *Phys. Rev. B*, 97:094408, 2018.

[232] M. Ashton, D. Gluhovic, S. B. Sinnott, J. Guo, D. A. Stewart, and R. G. Hennig. Two-dimensional intrinsic half-metals with large spin gaps. *Nano Lett.*, 17:5251–5257, 2017.

[233] J. He, S. Ma, P. Lyu, and P. Nachtigall. Unusual Dirac half-metallicity with intrinsic ferromagnetism in vanadium trihalide monolayers. *J. Mater. Chem. C*, 4:2518–2526, 2016.

[234] S.-J. Gong, C. Gong, Y.-Y. Sun, W.-Y. Tong, C.-G. Duan, J.-H. Chu, and X. Zhang. Electrically induced 2D half-metallic antiferromagnets and spin field effect transistors. *Proc. Natl. Acad. Sci.*, 115:8511–8516, 2018.

[235] D. Xiao, G.-B. Liu, W. Feng, X. Xu, and W. Yao. Coupled spin and valley physics in monolayers of $\mathrm{MoS_2}$ and other group-VI dichalcogenides. *Phys. Rev. Lett.*, 108:196802, 2012.

[236] L. Ciorciaro, M. Kroner, K. Watanabe, T. Taniguchi, and A. Imamoglu. Observation of magnetic proximity effect using resonant optical spectroscopy of an electrically tunable $\mathrm{MoSe_2/CrBr_3}$ heterostructure. *Phys. Rev. Lett.*, 124:197401, 2020.

[237] H. Zhang, W. Yang, Y. Ning, and X. Xu. Abundant valley-polarized states in two-dimensional ferromagnetic van der Waals heterostructures. *Phys. Rev. B*, 101:205404, 2020.

[238] S. Kezilebieke, M. N. Huda, V. Vaňol, M. Aapro, S. C. Ganguli, O. J. Silveira, S. Głlodzik, A. S. Forster, T. Ojanen, and P. Liljeroth. Topological superconductivity in a van der Waals heterostructure. *Nature*, 588:424–428, 2020.

[239] M. Binnewies, R. Glaum, M. Schmidt, and P. Schmidt. *Chemical Vapor Transport Reactions*. De Grutyer, 2012.

[240] M. Binnewies, R. Glaum, M. Schmidt, and P. Schmidt. Chemical vapor transport reactions - a historical review. *Z. Anorg. Allg. Chem.*, 639:219–229, 2013.

[241] A. Ubaldini and E. Giannini. Improved chemical vapor transport growth of transition metal dichalcogenides. *J. Cryst. Growth*, 401:878–882, 2014.